

International Journal of Antennas and Propagation

# Advances in Antennas for Wireless Identification and Sensing Systems

Guest Editors: Leena Ukkonen, Harish Rajagopalan,  
and Fan Yang





---

# **Advances in Antennas for Wireless Identification and Sensing Systems**

International Journal of Antennas and Propagation

---

**Advances in Antennas for Wireless  
Identification and Sensing Systems**

Guest Editors: Leena Ukkonen, Harish Rajagopalan,  
and Fan Yang



---

Copyright © 2013 Hindawi Publishing Corporation. All rights reserved.

This is a special issue published in “International Journal of Antennas and Propagation.” All articles are open access articles distributed under the Creative Commons Attribution License, which permits unrestricted use, distribution, and reproduction in any medium, provided the original work is properly cited.

## Editorial Board

M. Ali, USA  
Charles Bunting, USA  
Felipe Catedra, Spain  
Dau-Chyrh Chang, Taiwan  
Deb Chatterjee, USA  
Z. N. Chen, Singapore  
Michael Yan Wah Chia, Singapore  
Christos Christodoulou, USA  
Shyh-Jong Chung, Taiwan  
Lorenzo Crocco, Italy  
Tayeb A. Denidni, Canada  
Antonije R. Djordjevic, Serbia  
Karu P. Esselle, Australia  
Francisco Falcone, Spain  
Miguel Ferrando, Spain  
Vincenzo Galdi, Italy  
Wei Hong, China  
Hon Tat Hui, Singapore  
Tamer S. Ibrahim, USA  
Nemai Karmakar, Australia

Se-Yun Kim, Republic of Korea  
Ahmed A. Kishk, Canada  
Tribikram Kundu, USA  
Byungje Lee, Republic of Korea  
Ju-Hong Lee, Taiwan  
L. Li, Singapore  
Yilong Lu, Singapore  
Atsushi Mase, Japan  
Andrea Massa, Italy  
Giuseppe Mazzeola, Italy  
Derek McNamara, Canada  
C. F. Mecklenbräuker, Austria  
Michele Midrio, Italy  
Mark Mirotznik, USA  
Ananda S. Mohan, Australia  
P. Mohanan, India  
Pavel Nikitin, USA  
A. D. Panagopoulos, Greece  
Matteo Pastorino, Italy  
Massimiliano Pieraccini, Italy

Sadasiva M. Rao, USA  
Sembiam R. Rengarajan, USA  
Ahmad Safaai-Jazi, USA  
Safieddin Safavi-Naeini, Canada  
Magdalena Salazar-Palma, Spain  
Stefano Selleri, Italy  
Krishnasamy T. Selvan, India  
Zhongxiang Q. Shen, Singapore  
John J. Shynk, USA  
Mandeep S. Jit Singh, Malaysia  
Seong-Youp Suh, USA  
Parveen Wahid, USA  
Yuanxun Ethan Wang, USA  
Daniel S. Weile, USA  
Quan Xue, Hong Kong  
Tat Soon Yeo, Singapore  
Young Joong Yoon, Korea  
Wenhua Yu, USA  
Jong Won Yu, Republic of Korea  
Anping Zhao, China

# Contents

---

**Advances in Antennas for Wireless Identification and Sensing Systems**, Leena Ukkonen, Harish Rajagopalan, and Fan Yang  
Volume 2013, Article ID 816910, 2 pages

**Compact, Slotted, Printed Antennas for Dual-Band Communication in Future Wireless Sensor Networks**, Constantine G. Kakoyiannis and Philip Constantinou  
Volume 2013, Article ID 873234, 17 pages

**Dual-Band Antenna/AMC Combination for RFID**, M. E. de Cos and F. Las-Heras  
Volume 2012, Article ID 804536, 7 pages

**A Novel Electrically Small Meandered Line Antenna with a Trident-Shaped Feeding Strip for Wireless Applications**, Xueyao Ren, Xing Chen, and Kama Huang  
Volume 2012, Article ID 757429, 7 pages

**Resonant Frequency Calculation and Optimal Design of Peano Fractal Antenna for Partial Discharge Detection**, Jian Li, Changkui Cheng, Lianwei Bao, and Tianyan Jiang  
Volume 2012, Article ID 361517, 9 pages

**A Selective Ink Deposition Method for the Cost-Performance Optimization of Inkjet-Printed UHF RFID Tag Antennas**, J. Virtanen, J. Virkki, A. Z. Elsherbeni, L. Sydänheimo, and L. Ukkonen  
Volume 2012, Article ID 801014, 9 pages

## Editorial

# Advances in Antennas for Wireless Identification and Sensing Systems

**Leena Ukkonen,<sup>1</sup> Harish Rajagopalan,<sup>2</sup> and Fan Yang<sup>3</sup>**

<sup>1</sup> *Department of Electronics and Communications Engineering, Tampere University of Technology, 33720 Tampere, Finland*

<sup>2</sup> *Department of Electrical Engineering, University of California, Los Angeles, Los Angeles (UCLA), CA 90095, USA*

<sup>3</sup> *Electronic Engineering Department, Tsinghua University, Beijing 100084, China*

Correspondence should be addressed to Leena Ukkonen; [leena.ukkonen@tut.fi](mailto:leena.ukkonen@tut.fi)

Received 20 January 2013; Accepted 20 January 2013

Copyright © 2013 Leena Ukkonen et al. This is an open access article distributed under the Creative Commons Attribution License, which permits unrestricted use, distribution, and reproduction in any medium, provided the original work is properly cited.

Wireless identification and sensing systems are emerging in everyday use and the demand for ubiquitous automatic cognition and wireless sensing is growing rapidly [1, 2]. For example, passive sensors are critical and highly desirable in remote sensing platforms, where long term environment controlling and monitoring take place. Important features for the design of these sensors are that the sensor is wireless, battery-free, compact, and easy to integrate with other wireless passive sensors [3]. In addition, the growth of biosensors and health-related monitoring devices has accentuated the need for miniaturized, high-efficiency conformal sensing devices that can operate over a wide range of frequencies and are integrable in wearable and lightweight configurations [4]. For example, recently published “electronic tattoo” [5] presents an emerging wave of ideas of integrating sensors and other flexible electronic devices directly on human body. Electronic tattoo is a thin, extremely flexible device which has the same mechanical properties of skin to facilitate seamless attachment to the surface of skin.

Moreover, identification and monitoring of objects are needed in various supply chains and everyday logistics [6, 7]. Requirements in life cycle management (LCM) of different products have increased rapidly. For example, in construction business the condition and moisture of building structures are an important monitoring area. Also in the field of consumer electronics it is important to be able to monitor and manage the life cycle of products all the way from manufacturing to recycling.

Efficient wireless identification and sensing platforms have a huge potential to enhance the quality of life, for

example, in the fields of healthcare, security, and efficient use of available natural resources [8–11]. Antennas are one of the key components in achieving the desired efficient intelligent wireless platforms. In these future platforms, antennas should be small in size, efficient, and manufacturable with additive methods on environmentally friendly low cost substrates, such as paper. They should also be platform tolerant to enable attachment on various platform materials [2, 12, 13]. In addition, carbon nanotubes (CNTs) and graphene are attractive nanoscale materials which have been gaining a great interest in the research world recently [13, 14]. Their unique mechanical, electrical, and thermal properties make them promising building blocks for a large variety of applications in microelectronics and nanotechnologies [15]. In particular, CNTs are expected to address effectively numerous common electronic system challenges, such as tunability and miniaturization.

Recently, sensing methods based on the changes, for example, in the electrical properties of materials integrated with radio frequency identification (RFID) tag antennas, have gained a lot of interest within research groups globally [2, 8, 16]. Operation principle of passive RFID tag-integrated sensors can be based on the effects of change in the electrical properties of the sensing material on the performance of the RFID tag. No discrete or microchip-integrated sensor component is used in this kind of sensor tags. For example, permittivity of distilled water changes as a function on ambient temperature [16]. A sealed water pocket on top of the tag antenna’s matching circuit affects the impedance matching between the tag’s antenna and the microchip by

changing the input impedance of the tag antenna. Change in the impedance matching in turn affects the optimum operating frequency of the sensor tag, which serves as an indicator of temperature change or of a specific temperature value.

This special issue presents articles containing newest developments of antennas in wireless identification and sensing systems. In the paper entitled “*Dual-Band Antenna/AMC Combination for RFID*” M. E. de Cos and F. Las-Heras present a novel antenna—artificial magnetic conductor (AMC) combination usable in dual-band radio frequency identification (RFID) tags over metallic objects.

To address the miniaturization requirements, X. Ren et al. propose a novel electrically small antenna (ESA) based on the meandered line structure in their paper entitled “*A Novel Electrically Small Meandered Line Antenna with a Trident-Shaped Feeding Strip for Wireless Applications*.”

Ultrahigh-frequency (UHF) approaches have caught increasing attention recently and have been considered as a promising technology for online monitoring of partial discharge (PD) signals. The paper entitled “*Resonant Frequency Calculation and Optimal Design of Peano Fractal Antenna for Partial Discharge Detection*” by J. Li et al. presents a Peano fractal antenna for UHF PD online monitoring of transformer with small size and multiband features.

To improve the cost-efficiency of novel ink jet printed RFID tag antennas, J. Virtanen et al. present a paper entitled “*A Selective Ink Deposition Method for the Cost-Performance Optimization of Inkjet-Printed UHF RFID Tag Antennas*”. The deposition method is based on identifying areas with high surface current densities on a given tag antenna and applying additional silver nanoparticle ink onto such areas to increase tag read range.

The paper written by C. Kakoyiannis and P. Constantinou, entitled “*Compact, Slotted, Printed Antennas for Dual-Band Communication in Future Wireless Sensor Networks*,” describes how printed antennas, especially inverted-F antennas (IFAs) can be efficiently designed as simple, compact, device-integrated, dual-band antennas.

All papers appearing in this special issue have been subject to a strict peer reviewing process. They are of high quality and address the area of antennas for wireless identification and sensing systems from different perspectives. It is our expectation that through this special issue, some valuable ideas and conclusions on this challenging topic are provided. In addition, we hope that the published papers provoke new ideas and research in this area.

Leena Ukkonen  
Harish Rajagopalan  
Fan Yang

## References

- [1] T. T. Thai, L. Yang, G. R. Dejean, and M. M. Tentzeris, “Nanotechnology enables wireless gas sensing,” *IEEE Microwave Magazine*, vol. 12, no. 4, pp. 84–95, 2011.
- [2] R. Vyas, V. Lakafosis, A. Rida et al., “Paper-based RFID-enabled wireless platforms for sensing applications,” *IEEE Transactions on Microwave Theory and Techniques*, vol. 57, no. 5, pp. 1370–1382, 2009.
- [3] T. T. Thai, J. M. Mehdi, H. Aubert et al., “A novel passive wireless ultrasensitive RF temperature transducer for remote sensing,” in *Proceedings of the IEEE International Microwave Symposium (IMS '10)*, pp. 473–476, May 2010.
- [4] A. Traille, L. Yang, A. Rida, and M. M. Tentzeris, “A novel liquid antenna for wearable bio-monitoring applications,” in *Proceedings of the IEEE International Microwave Symposium Digest (MTT '08)*, pp. 923–926, June 2008.
- [5] J. Cartwright, “Electronic skin grafts gadgets to body,” *ScienceNOW*, August 2011, <http://news.sciencemag.org/science-now/2011/08/electronic-skin-grafts-gadgets-t.html>.
- [6] A. Lehto, J. Nummela, L. Ukkonen, L. Sydänheimo, and M. Kivikoski, “Passive UHF RFID in paper industry: challenges, benefits and the application environment,” *IEEE Transactions on Automation Science and Engineering*, vol. 6, no. 1, pp. 66–79, 2009.
- [7] J. Nummela, K. Määttä, L. Ukkonen, and L. Sydänheimo, “Utilizing UHF RFID in supply chains: examples from similarities in paper and cell phone industries,” *International Journal of Latest Trends in Computing (IJLTC)*, vol. 2, no. 3, 2011.
- [8] C. Occhiuzzi and G. Marrocco, “The RFID Technology for Neurosciences: feasibility of limbs’ monitoring in sleep diseases,” *IEEE Transactions on Information Technology in Biomedicine*, vol. 14, no. 1, pp. 37–43, 2010.
- [9] H. Rajagopalan and Y. Rahmat-Samii, “Ingestible RFID biocapsule tag design for medical monitoring,” in *Proceedings of the IEEE International Symposium on Antennas and Propagation*, July 2010.
- [10] L. Yang, R. Vyas, A. Rida, J. Pan, and M. Tentzeris, “Wearable RFID-enabled sensor nodes for biomedical applications,” in *Proceedings of the IEEE Electronic Components and Circuits Conference*, pp. 2156–2159, 2008.
- [11] J. Virtanen, L. Ukkonen, T. Björninen, and L. Sydänheimo, “Printed Humidity Sensor for UHF RFID Systems,” in *Proceedings of the Sensors Applications Symposium (SAS '10)*, pp. 269–272, IEEE, February 2010.
- [12] J. Virtanen, T. Björninen, L. Ukkonen, and L. Sydänheimo, “Passive UHF inkjet-printed narrow-line RFID tags,” *IEEE Antennas and Wireless Propagation Letters*, vol. 9, pp. 440–443, 2010.
- [13] M. M. Tentzeris, “Inkjet-printed paper-based RFID and nanotechnology-based ultrasensitive sensors: The “Green” ultimate solution for an ever improving life quality and safety?” in *Proceedings of the IEEE Radio and Wireless Symposium (RWS '10)*, pp. 120–123, January 2010.
- [14] B. H. Kim, T. H. Park, S. J. Baek et al., “N-type carbon nanotube by alkaline-earth metal Sr doping,” *Journal of Applied Physics*, vol. 103, no. 9, Article ID 096103, 2008.
- [15] R. De Paolis, S. Pacchini, F. Coccetti et al., “Circuit model of carbon-nanotube inks for microelectronic and microwave tunable devices,” in *Proceedings of the IEEE International Microwave Symposium (IMS '11)*, June 2011.
- [16] J. Virtanen, L. Ukkonen, T. Björninen, A. Z. Elsherbeni, and L. Sydänheimo, “Temperature sensor tag for passive UHF RFID systems,” in *Proceedings of the IEEE Sensor Applications Symposium*, pp. 312–317, San Antonio, Tex, USA, February 2011.

## Research Article

# Compact, Slotted, Printed Antennas for Dual-Band Communication in Future Wireless Sensor Networks

Constantine G. Kakoyiannis and Philip Constantinou

Mobile Radio Communications Laboratory, National Technical University of Athens, Zographos Polytechnic Campus,  
9 Iroon Polytechniou Street, 15773 Athens, Greece

Correspondence should be addressed to Constantine G. Kakoyiannis; [kkak@mobile.ntua.gr](mailto:kkak@mobile.ntua.gr)

Received 13 August 2012; Revised 25 October 2012; Accepted 20 December 2012

Academic Editor: Fan Yang

Copyright © 2013 C. G. Kakoyiannis and P. Constantinou. This is an open access article distributed under the Creative Commons Attribution License, which permits unrestricted use, distribution, and reproduction in any medium, provided the original work is properly cited.

Inverted-F antennas (IFAs) are a primary choice to implement the radiating system of portable devices. A tried and tested idea can remain topical if proven useful in modern applications. This paper shows that printed IFAs (PIFAs) are capable of forming robust, compact, dual-band radiating systems for wireless microsensors with an adjustable spacing between bands. Reactive tuning was applied by inductively loading the structures with prefractal slots; inductive slot loading degenerates higher-order resonances and increases the fractional bandwidth (FBW). The current distributions revealed that most of the element area is used for radiation at both resonances. In radiation terms, the antennas provide satisfactory gains and high efficiencies ( $\geq 82\%$ ). A simple figure of merit is used to compare the performance of the three PIFAs head to head. Operation at 2.5 GHz and 5.5 GHz indicated that changes in slot geometry almost double the FBW. The proposed antennas serve both the 5.15–5.35 GHz U-NII and the 5.8 GHz ISM bands; at the lower band, their size is less or equal to the half-wavelength dipole. This study of dual-band antennas also showed that the aggregate FBW of a PIFA is bounded; by degenerating higher-order modes, the designer redistributes whatever bandwidth is available by the antenna itself to the desired bands.

## 1. Introduction

*1.1. Background and Motivation.* For the past fifteen years inverted-F antennas have been a major design vehicle for the implementation of radiating systems for portable devices [1–8]. IFAs use image theory as their basic miniaturization technique through a shorting wall or pin that ties them to the ground plane (GNDP). The planar version of IFAs inherits the cavity features of microstrip patch antennas, thus its bandwidth is inherently limited. Extensive antenna and/or GNDP alteration has been applied through slots and slits to excite more radiating modes. The printed version of IFAs is not shaped like a cavity, thus it is significantly more broadband.

Dual-band printed and planar IFAs have drawn significant attention in the existing literature [9–21]. Starting from legacy applications like PCMCIA cards [9], the use of dual-band PIFAs was extended to (i) wireless LAN communication for laptop computers in the 2.4- and 5.2/5.8-GHz bands

[11–13, 15, 16, 20], (ii) mobile phone antennas operating at 900/1900 MHz [14], (iii) dual-band communication at 2.6 and 5.5 GHz [17], (iv) mobile phones equipped with WLAN capability operating at DCS/ISM frequencies [18], and (v) dual-band antennas printed on USB dongles serving as multiband antennas [19]. In the case of portable computers (laptops), printed antennas are usually installed under the lid on the back side of the screen [20]. Furthermore, printed dual-band antennas can be readily applied to WLAN routers. Finally, in a recent study, Li et al. [21] proposed a reconfigurable structure that can be transformed from a double planar IFA into a meandered loop antenna by means of a PIN diode switch. The two modes of operation enable the antenna to achieve complementary operating bands in the 0.79–2.56 GHz range.

This paper addresses the design of dual-band PIFAs for wireless sensor nodes. It aims to show that by properly applying inductive loading in the form of prefractal slots, printed IFAs are capable of producing robust, compact, dual-band radiating systems for wireless microsensors with an

adjustable spacing between bands. One could argue that dual-band antennas find no use in wireless sensor networks (WSNs), because dual-band WSNs do not exist: the second integrated transceiver that is required along with its peripheral passive components bring extra complexity, cost, and energy consumption for a wireless microsensor. So, it is best to wait until very large scale integration (VLSI) technology matures to the point of single-chip, dual-band, integrated transceivers. However, the above arguments do not hold for two reasons. On one hand, dual-band communication is inherent in real-world WSN deployments: the microsensors implement various algorithms, for example, routing, localization, virtual array formation, and improved connectivity and coverage. These algorithms depend on GPS signal reception; hence, a second communication band comes into play. On the other hand, dual-band, single-chip, integrated transceivers are already here: Cho et al. [22] designed an energy-efficient, dual-band, fully integrated transceiver for body sensor network applications in the 30–70 MHz and MICS (402–405 MHz) bands. Thus, it is anticipated that dual-band communication will become vital in future wireless sensor networks.

To the best of the authors' knowledge, the only existing study on dual-band antennas that target wireless sensors is the work of Mendes et al. [10]. We comment on this work in Section 4, along with the rest of the relevant literature.

*1.2. Theoretical Considerations.* Boyle [5, 23] and Boyle and Lighthart [24] used superposition and divided the operation of the antenna into the balanced (nonradiating) and the radiating mode. One of their key findings was that the PCB length has a strong effect on antenna quality factor,  $Q$ : the  $Q$  is minimized when the length is close to the  $\lambda/2$ - or  $\lambda$ -antiresonance. Hence, the bandwidth (BW), which is related to the quality factor  $Q$ , is strongly affected by the length of the GNDP. Furthermore, in the case of dual-band PIFAs, the width of the two bands is not independent; to improve BW at the lower resonance, the higher resonance BW must be degraded.

Referring to the internal workings of dual-band slotted planar IFAs [1, 25], Boyle suggested that slots in the antenna top plate between the feed and short pins allow independent variation of the impedance transformation and shunt reactance [5, 23, 24]. Furthermore, slots in the top plate can tune a planar inverted-L antenna (ILA) that is naturally resonant between the lower and upper resonance. If the slot is too long, the lower BW is degraded; if the slot is too short, the upper BW is degraded.

The technique of degenerating higher-order radiating modes by inductive loading of the antenna with slots applies equally well in the case of nonadjacent frequency bands. This has been shown for planar IFAs by Liu et al. [25] and Boyle and Lighthart [23, 24]. Angelopoulos et al. [9] showed that this response is also feasible with printed IFAs: the authors of [9] presented an application of the slot-loading concept, which involved a dual-band PIFA comprised of two  $\lambda/4$  monopoles coupled and separated by an L-slot. It was suggested that each monopole radiates in its own resonance

frequency (2.45/5.25 GHz) when fed by a single feeding port connected to the smaller monopole. It was also theorized that the function of the L-slot was to form a gap for higher frequency currents, which at the same time is not wide enough to disturb the lower resonance. The work described herein will demonstrate that, in general, this is not the case.

*1.3. Scope and Structure of the Paper.* Based on our experience with multimode, single-band printed IFAs [26], we have attempted to design microsensor-oriented PIFAs which should satisfy the following specifications.

- (1) Display a bandwidth at least equal to 100 MHz in the vicinity of 2.5 GHz, thus a fractional bandwidth  $\text{FBW}_{Ve} \geq 4\%$ .
- (2) Display a bandwidth at least equal to 200 MHz at the lower end of the 5–6 GHz range. A good application example is the U-NII 5.15–5.35 GHz band, which features a fractional bandwidth  $\text{FBW}_{Vu} = 3.8\%$ .
- (3) Achieve the previous two specifications without exceeding the electrical size,  $ka$ , of the half-wavelength dipole,  $(ka)_{\lambda/2} = \pi/2$  rad, at the lower band.
- (4) Achieve a mean total radiation efficiency over both bands at least equal to 80%, that is,  $\overline{\eta}_{\text{total}} \geq -1$  dB.

The paper describes the design of printed inverted-F antennas that have been inductively loaded by four different pre-fractal slots. The first three slot topologies were discussed in detail in [26]: they are the simple, generalized, and dual generalized, Koch curves of the second iteration. The fourth slot resembles the quadratic type 2 Koch curve; its properties are described in Section 3.4. The effect of the size of the ground plane on both frequency bands was also investigated. The reactive loading imposed by the pre-fractal slots not only surpassed the specifications, but also outperformed the results of several prior studies. Section 2 discusses design and modelling issues. Section 3 displays an array of numerical results produced by accurate computational models of the four slotted antenna configurations. Section 4 discusses the results. Section 5 presents measurement results harvested from a prototype antenna. Finally, Section 6 concludes the paper.

## 2. Antenna Design and Electromagnetic Modelling

Out of the four antennas that were designed, the first three were inductively loaded by slots shaped after the following pre-fractal curves:

- (1) the Koch curve of the second iteration (abbreviated herein as “K2”) [26],
- (2) the generalized Koch curve of the second iteration (abbreviated herein as “GK2”) [26], and
- (3) the dual generalized Koch curve of the second iteration (abbreviated herein as “D-GK2”) [26].

Apart from [26], the properties of Koch curve variants are also described in [27–30], thus the details are omitted here for

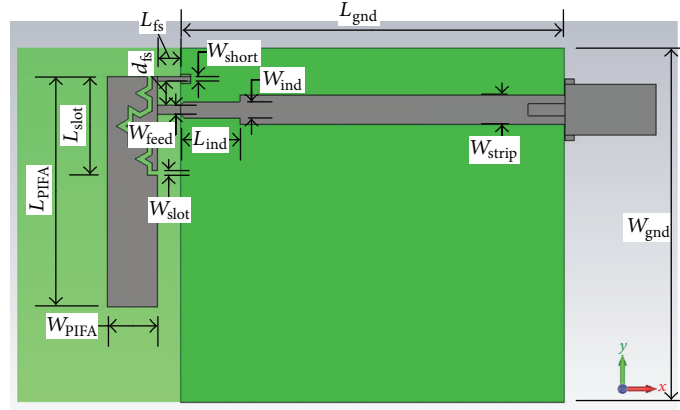


FIGURE 1: Parametric breakdown of the printed IFA loaded with an embedded Koch-shaped slot. The substrate is transparent, showing the ground plane on the bottom layer. The nomenclature of parameters is a simplified version of the one used in [26].

brevity. The fourth antenna was loaded by a quadratic type 2 Koch curve of the second iteration (abbreviated herein as “MK2”), which is described in Section 3.4.

The antennas were designed to operate about the centre frequencies  $f_{0\ell} = 2.5$  GHz and  $f_{0u} = 5.25$  GHz, where the corresponding wavelengths are  $\lambda_{0\ell} = 120$  mm and  $\lambda_{0u} \approx 57.1$  mm. The 2-layer PCBs are made of Taconic TRF-45 material ( $\epsilon_r = 4.38$  and  $\tan \delta_e = 0.0028$  at 2.5 GHz). The substrate is  $H_{\text{sub}} = 1.63$  mm thick, and it is loaded with 1 oz copper on each side [31]. Higher frequencies at the upper band demand the use of a good quality substrate that features low-loss and well-controlled relative permittivity. TRF-45 combines low-loss with an FR4-compatible printing process. In this system model, the size of the PCB represents the whole size of the sensor node. On the top layer, we etched the printed antenna and the 3.1 mm-wide microstrip line that excites it. On the bottom layer, there is a continuous copper cladding that serves as the ground plane (GNDP) of both antenna and microstrip line. The GNDP was removed below the antenna. Assuming that the PCB in Figure 1 is an autonomous node, then all radiofrequency (RF) and baseband integrated circuits and discrete components would be soldered on the bottom layer in an actual implementation. This structure can be easily transformed to uniplanar (single-sided PCB) by changing the feed to coplanar waveguide (CPW). The use of ground-backed CPW would double the available space for RF and baseband electronics.

The antennas were designed and simulated by means of a transient solver, which is part of a full-wave E/M simulator that uses the finite integration technique (FIT) to reformulate Maxwell’s integral equations into the so-called “Maxwell Grid Equations.” In the time domain, by applying Yee’s spatial discretization and time-stepping scheme, FIT results in the same set of equations as FDTD [32, 33]. The structures were excited by a wideband Gaussian pulse (DC–7 GHz). A spatially adaptive hexahedral mesh discretized the objects. Finer meshing was applied inside the substrate to capture the large gradients of the E-field; the same applies across the microstrip feed, on the main arm, and inside

the dielectric of the SMA connector. The simulator stopped when the initial system energy decayed by 40 dB. This trade-off between simulation speed and FFT truncation error was slightly in favour of speed. The maximum cell size at 7 GHz (smallest wavelength) was set at  $\lambda_{7\text{GHz}}/20$ . The solvable space was terminated at four Berenger PML layers, with a distance-to-boundary equal to  $\lambda_{3\text{GHz}}/8$ . The antennas did not exhibit topological symmetry, thus did not satisfy the required boundary conditions of electric and magnetic flux for the placement of “magnetic walls”, which would lower the computational burden. The complexity of the models varied in the range  $370\text{--}495 \times 10^3$  Yee cells. Complexity depends on the size of the PCB and the level of detail exhibited by the antenna element. Narrow copper traces and narrow object spacing contribute greatly to complexity. The MK2 model exhibited 28–33% greater complexity compared to the other three model due to its inherently finer structure. Simulation setup settings are summarized in Table 1.

### 3. Proposed Radiating Structures and Numerical Results

The design of the four slotted antennas is based on the manual optimization procedure and design guidelines that were reported in [26]. The controlling parameters of the antennas converged to the values listed in Table 2. The nomenclature of parameters shown in Figure 1 is a representative of all four structures.

Table 2 lists at the bottom parameters  $L_{\text{ind}}$  and  $W_{\text{ind}}$ . In order to achieve a well-balanced input impedance in both operating bands, there is a need to compensate the capacitive part of the impedance. The imaginary part,  $X_{\text{in}}(j\omega)$ , assumed large negative values, because the common length of the feeding and shorting stubs,  $L_{\text{fs}}$ , is short due to high-frequency upper band, thus the main arm of the PIFA approaches the ground plane far more than it did in the case of the multi-mode, single-band counterparts [26]. To mend this problem, the last segment of the microstrip feed line, whose length equals  $L_{\text{ind}}$ , was narrowed from  $W_{\text{strip}}$  down to  $W_{\text{ind}}$ . The

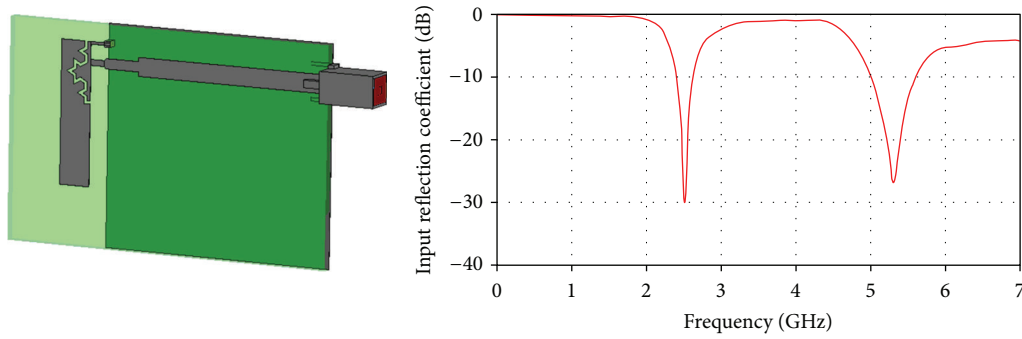


FIGURE 2: The computational model of the dual-band K2 PIFA in perspective and the magnitude of its input reflection coefficient in the range DC-7 GHz.

TABLE 1: Settings applied to the FIT-TS solver [32, 33] during the simulations of the slotted PIFAs.

Slotted PIFA simulation setup	
Excitation signal	Gaussian pulse, DC-7 GHz
Spatial discretization	Hexahedral, nonuniform
Convergence condition	40 dB energy decay
Maximum cell size at $f_{\max}$	$\lambda_{\min}/20$
Absorbing boundary conditions	4-layer PML
Minimum distance to PML boundary	$\lambda_{3\text{GHz}}/8$
Computational complexity, (D)-(G)K2	$(370-385) \times 10^3$ Yee cells
Computational complexity, MK2	$495 \times 10^3$ Yee cells

narrowed segment inserts extra inductance in series with  $Z_{\text{in}}(j\omega)$  and makes up the simplest matching circuit.

It is also noted that the design procedure verified the manual optimization algorithm given in [26], but with one important difference: excluding parameters  $L_{\text{PIFA}}$  and  $L_{\text{slot}}$ , the other six parameters affect the response of the antenna in the two frequency bands in opposite ways. For example, a change in  $d_{\text{fs}}$  that improves matching and resonance in the lower band, worsens the performance in the upper band, and vice versa. Inevitably, parameter values were chosen in a compensatory manner.

During simulations for the virtual prototyping, an automated calculation of the electrical size of antennas was required. Thus, the automated estimation of the radius of the circumscribing sphere was based on the simplified expression

$$a = \frac{1}{2} \sqrt{W_{\text{strip}}^2 + (W_{\text{PIFA}} + L_{\text{fs}} + L_{\text{gnd}})^2}, \quad (1)$$

which produces slightly larger electrical sizes than the actual ones.

This section demonstrates through accurate computational models (virtual prototypes) the electrical performance of the four slotted PIFAs.

**3.1. Dual-Band PIFA Loaded by the Koch Slot.** The first antenna that was designed is inductively loaded by a Koch-shaped slot of the second iteration, which has been described in [26] and also in [27–30]. The computational model and the broadband magnitude of the input reflection coefficient are depicted in Figure 2. Antenna dimensions, starting with  $L_{\text{slot}}$ , were adjusted so as to obtain resonances at the desired bands. The high-frequency upper band leads to a significantly smaller slot compared to the one in [26]: the side length ratio of the outline of the K2 slot remains constant as dimensions vary, thus the slot is much shorter, allowing for the design of a PIFA with a significantly narrower main arm. The feeding line is offset with respect to the longitudinal symmetry axis of the PCB. Application of the offset feed further facilitates matching and resonance in both bands. The key numerical results of the K2 PIFA are listed in Table 4. The antenna meets all four specifications, but the figure of merit assumes negative values in decibels. In the lower band the low FoM values are due to the reduced bandwidth, whereas in the upper band they result from the increased electrical size: in the 5-6 GHz range the K2 PIFA is electrically large ( $ka > 2$  rad).

The Smith charts in Figure 3 were derived after placing the reference plane of the scattering parameters at the beginning of the SMA end launch connector. The charts indicate that the compensatory dimensions that were chosen for the K2 antenna produce a frequency response that is well-balanced between inductive and capacitive reactance. Furthermore, in the lower band the input resistance is equally distributed below and above  $50 \Omega$ , whereas in the upper band we mostly get  $R_{\text{in}} < 50 \Omega$ .

The surface current distributions (SCDs) in Figure 4 show concurrent maxima of current density at every point on the PCB. Concurrent maxima are physically unrealisable due to the phase shift along the structure, but they are useful for identifying “hot” and “cold” regions. The SCDs indicate that (i) in the lower frequency band practically the whole extent of the main arm radiates and (ii) in the upper band the main arm radiates mainly along the K2 slot, whereas a discontinuous image forms on the ground plane with a greater overall length. In both bands, return currents are strong along all four sides of the GNPD.

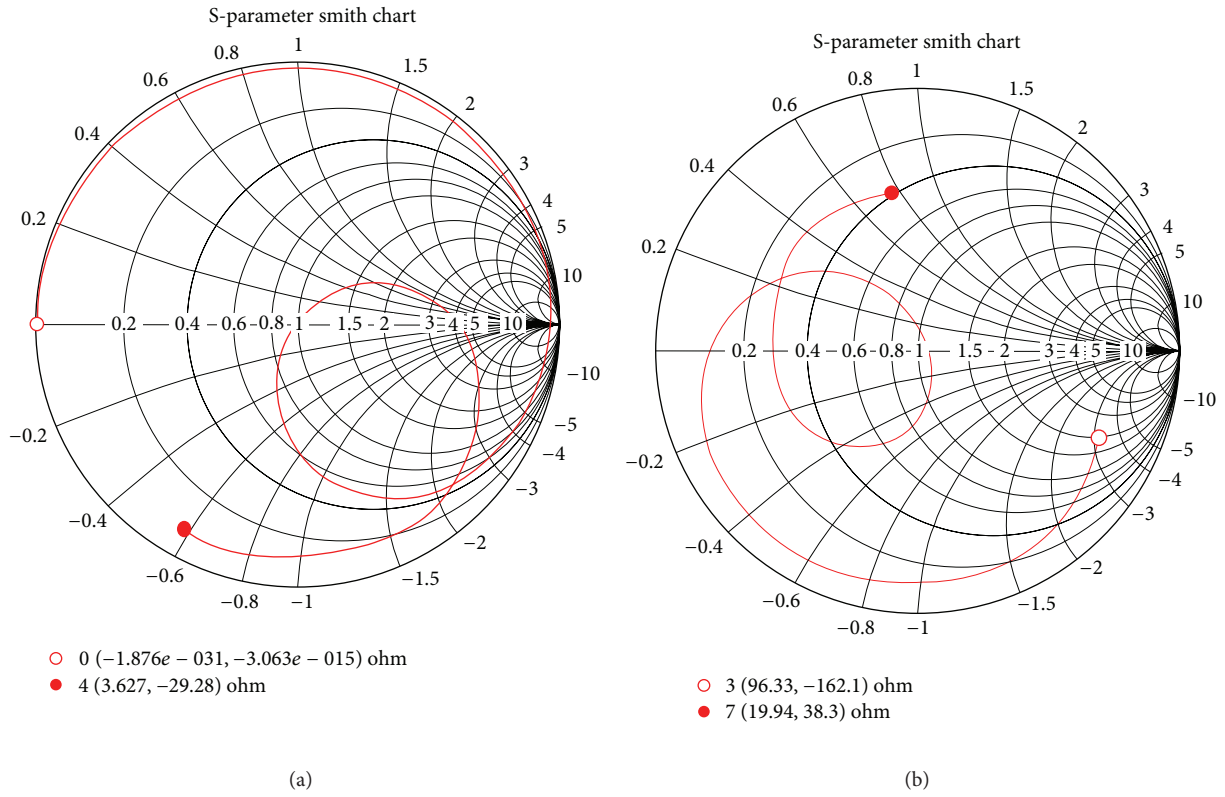


FIGURE 3: Smith chart of the complex reflection coefficient of the dual-band K2 PIFA in the overlapping frequency ranges DC-4 GHz and 3-7 GHz.

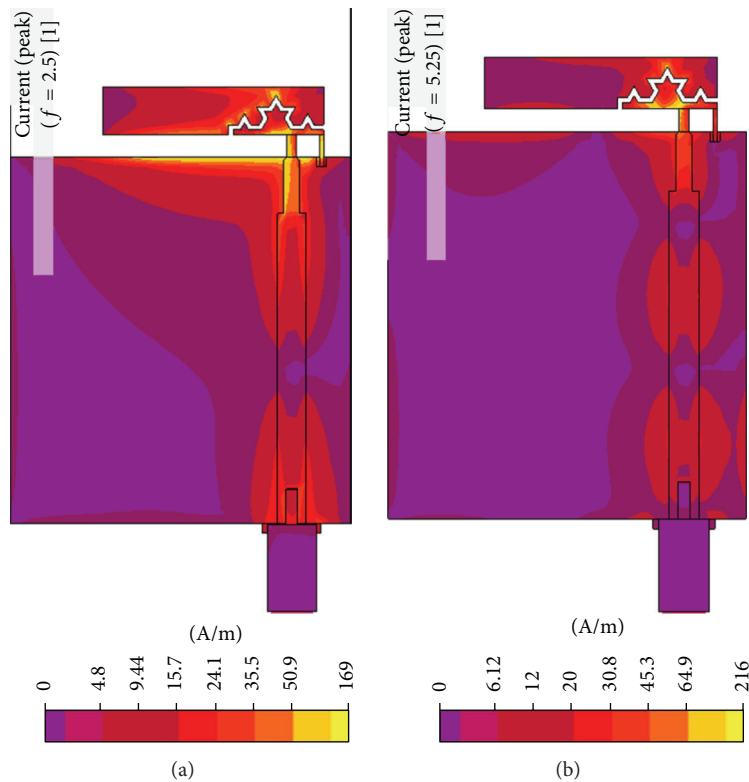


FIGURE 4: Surface current distributions of the dual-band K2 PIFA at 2.5 GHz and 5.25 GHz.

TABLE 2: Values of parameters that determine the design of the four proposed dual-band PIFAs. All dimensions are in millimetres.

Dimension	K2	GK2	D-GK2	MK2
$L_{\text{sub}} \times W_{\text{gnd}}$	$57 \times 37$	$54 \times 35.8$	$54 \times 36.2$	$60 \times 33.6$
$L_{\text{gnd}} \times W_{\text{gnd}}$	$40 \times 37$	$40 \times 35.8$	$40 \times 36.2$	$40 \times 33.6$
$L_{\text{PIFA}} \times (W_{\text{PIFA}} + L_{\text{fs}})$	$24.0 \times 7.7$	$23.3 \times 7.8$	$23.2 \times 7.6$	$21.2 \times 8.1$
$W_{\text{strip}}$	3.1	3.1	3.1	3.1
$d_{\text{fs}}$	2.5	2.1	2.2	1.5
$L_{\text{slot}}$	10.3	8.9	8.9	6.7
$L_{\text{PIFA}}$	24.0	23.3	23.2	21.6
$L_{\text{fs}}$	2.4	1.4	1.5	1.5
$W_{\text{slot}}$	0.5	0.5	0.6	0.3
$W_{\text{PIFA}}$	5.3	6.4	6.1	6.6
$W_{\text{short}}$	0.5	0.4	0.4	0.4
$W_{\text{feed}}$	1.0	1.1	0.6	0.9
$L_{\text{ind}}$	6.2	6.1	6.4	6.2
$W_{\text{ind}}$	1.7	1.9	2.3	1.9

The first row denotes the extent of the PCB, the second row denotes the size of the ground plane, and the third one denotes the extent of the antenna element.

### 3.2. Dual-Band PIFA Loaded by the Generalized Koch Slot.

The second antenna that was designed is inductively loaded by a generalized Koch-shaped slot of the second iteration, which has been described in [26]. The computational model and the broadband magnitude of the input reflection coefficient are depicted in Figure 5. The antenna resonates at 2.5 GHz, 5.14 GHz, and 5.71 GHz. This means that by a simple change in slot geometry the reactive loading produces a second  $S_{11}$  minimum in the 5-6 GHz range. As a result, the 5-6 GHz range meets the VSWR criterion practically in its full extent. The key numerical results of the K2 PIFA are listed in Table 4.

The Smith charts in Figure 6 indicate that the compensatory dimensions that were chosen for the GK2 antenna produce a frequency response that is well-balanced between inductive and capacitive reactance. Furthermore, in the lower band the input resistance is equally distributed below and above  $50 \Omega$ , whereas in the upper band we mostly get  $R_{\text{in}} < 50 \Omega$ . Finally, the  $S_{11}$  minimum at 5.71 GHz is not a resonance in the strict sense, but appears as a result of the small loop that the curve traces.

The surface current distributions in Figure 7 show concurrent maxima of current density at every point on the PCB. In the lower frequency band, the same comments as in the K2 case apply. At 5.14 GHz, the main arm radiates mostly along the GK2 slot, whereas a discontinuous image forms on the ground plane with greater overall length. At 5.71 GHz, the main arm radiates uniformly (not focused around the slot), whereas a strong image forms on the ground plane away from the slot.

**3.3. Dual-Band PIFA Loaded by the Dual Generalized Koch Slot.** The third antenna was inductively loaded by the dual generalized Koch-shaped slot of the second iteration, which has been described in [26]. This particular version of the

Koch pre-fractal shape exhibits lower variations in height and thus produced an antenna with slightly narrower main arm. The computational model and the broadband magnitude of the input reflection coefficient are depicted in Figure 8. The antenna resonates at 2.5 GHz, 5.11 GHz, and 5.77 GHz, that is, the dual of the generalized Koch slot preserves the second  $S_{11}$  minimum in the 5-6 GHz range. The key numerical results of the K2 PIFA are listed in Table 4.

The Smith charts in Figure 9 indicate that the compensatory dimensions that were chosen for the D-GK2 antenna produce a frequency response that is well-balanced between inductive and capacitive reactance. Furthermore, in the lower band the input resistance is equally distributed below and above  $50 \Omega$ , whereas in the upper band we mostly get  $R_{\text{in}} < 50 \Omega$ . Finally, the  $S_{11}$  minimum at 5.77 GHz appears as a result of the small loop traced by the curve, which produces an extra resonance.

The surface current distributions in Figure 10 show concurrent maxima of current density at every point on the PCB. At 2.5 GHz and 5.11 GHz the same comments as in the K2 and GK2 cases apply. At 5.77 GHz, the main arm radiates in an exceptionally uniform manner almost ignoring the presence of the slot, whereas a strong image forms on the ground plane away from the slot.

### 3.4. Dual-Band PIFA Loaded by the Quadratic Koch Slot.

The fourth antenna was inductively loaded by the quadratic Koch-shaped slot of the second kind and second iteration. This particular version of the Koch pre-fractal shape is also known in the literature as the Minkowski sausage. The curve is produced by an iterative function system (IFS) [26–30] as illustrated in Figure 11: an initial straight segment is divided into  $n$  equally long, consecutive segments. Then, each one of the  $n - 2$  middle segments is replaced by a  $\Pi$ -shaped broken line. The straight segments of the broken line are equal in length to the initial subdivisions. In order for the curve to preserve its self-avoidance, a sequence of proper and inverted Pi shapes is created. In this way, during the first iteration of the pre-fractal curve, the initial straight segment takes on the shape of a meander line. Thus, we are working with a hybrid meander-Koch curve, and this is where the abbreviation “MK2” for the  $i = 2$  iteration came from. It is easily proven that, with every new iteration, the updated curve comprises  $3n - 4$  straight segments, where  $n$  is the number of segments comprising the previous iteration. Therefore, the Hausdorff dimension for  $i = +\infty$  is equal to

$$D_{\text{MK}} = \frac{\ln(3n - 4)}{\ln(n)} \quad (2)$$

and is maximized when the initial straight segment is divided into  $n_{\text{opt}} = \arg \max\{D_{\text{MK}}\} = 4$  subdivisions:  $D_{\text{MK,max}} = 1.5$ . The increased complexity of the MK2 curve leads to two geometrical differences with regard to the previous three antennas: (i) the current covers a longer path as it traverses the initial part of the main arm, thus length  $L_{\text{PIFA}}$  turns out to be 8.6–11.7% shorter when compared to the corresponding lengths of the previous three antennas; (ii) the width of the MK2 slot had to be reduced by a factor of two to facilitate

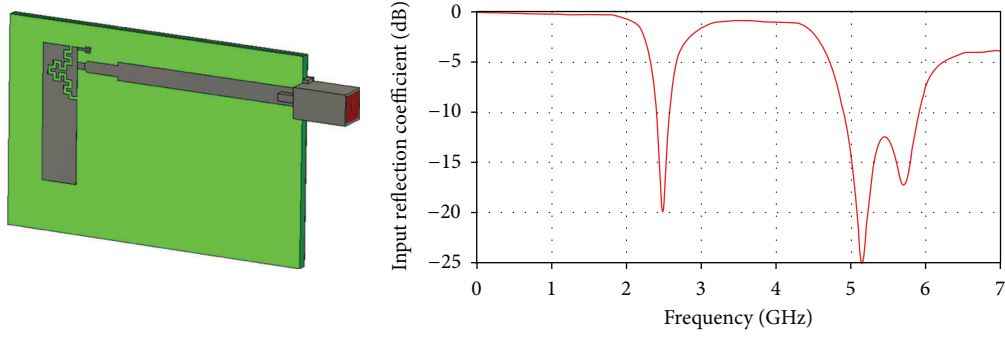


FIGURE 5: The computational model of the dual-band GK2 PIFA in perspective and the magnitude of its input reflection coefficient in the range DC-7 GHz.

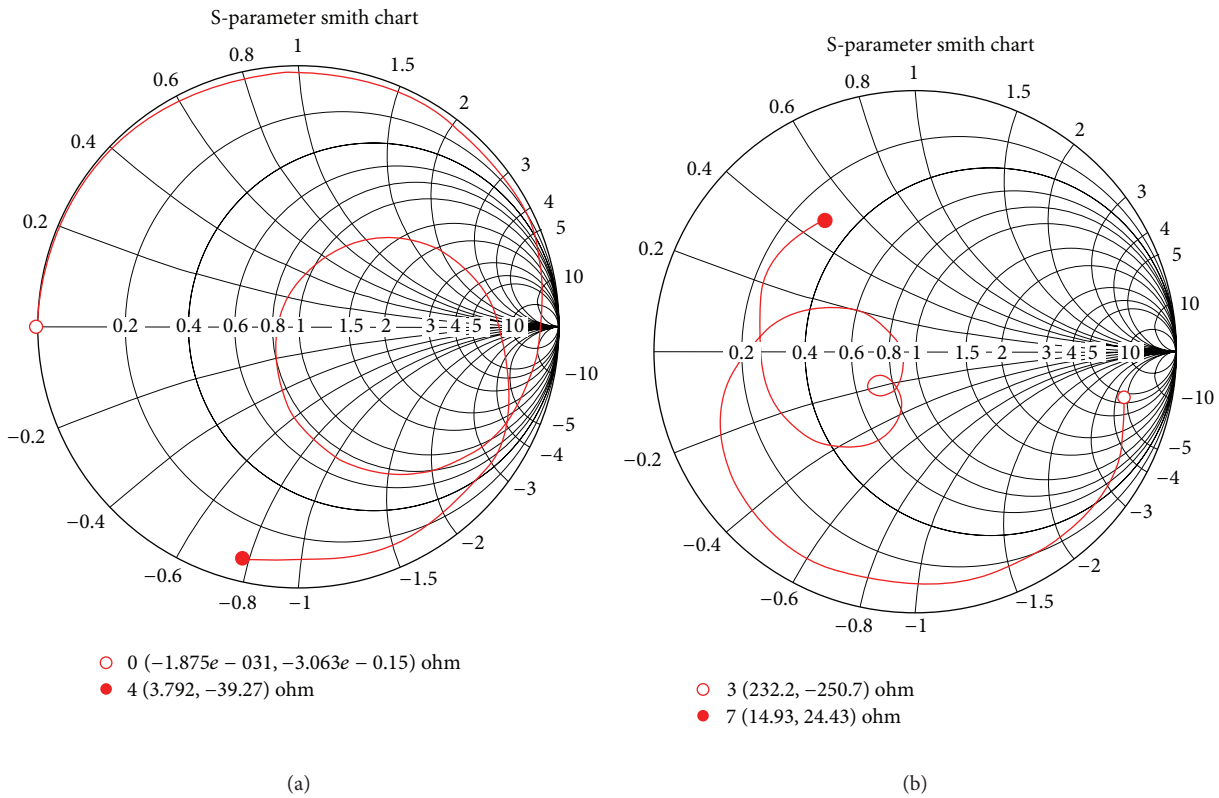


FIGURE 6: Smith chart of the complex reflection coefficient of the dual-band GK2 PIFA in the overlapping frequency ranges DC-4 GHz and 3-7 GHz.

fabrication. The computational model and the broadband magnitude of the input reflection coefficient are depicted in Figure 12. The antenna resonates at 2.45 GHz, 5.24 GHz, and 5.88 GHz. The meander-Koch slot preserves the second  $S_{11}$  minimum; however, the matching meets the VSWR criterion only approximately in the 5-6 GHz range. The key numerical results of the K2 PIFA are listed in Table 4.

The Smith charts in Figure 13 indicate that the compensatory dimensions that were chosen for the MK2 antenna produce a frequency response that is well-balanced between inductive and capacitive reactance. Furthermore, in the lower band we get an input resistance  $R_{in} > 50 \Omega$ , whereas in the upper band we obtain  $R_{in} < 50 \Omega$ . Finally, in this case, it is the

$S_{11}$  minimum at 5.24 GHz that appears as a result of a small loop traced by the curve.

The surface current distributions in Figure 14 show concurrent maxima of current density at every point on the PCB. At 2.5 GHz the same comments as in the previous three cases apply. At 5.24 GHz and 5.88 GHz, the main arm radiates mostly in the vicinity of the slot, whereas a strong image forms on the ground plane along the full extent of the main arm.

**3.5. Study of Ground Plane Effect.** The effect of the size of the ground plane was studied in the same manner as in [26, 34]. The most important findings are briefly summarized here.

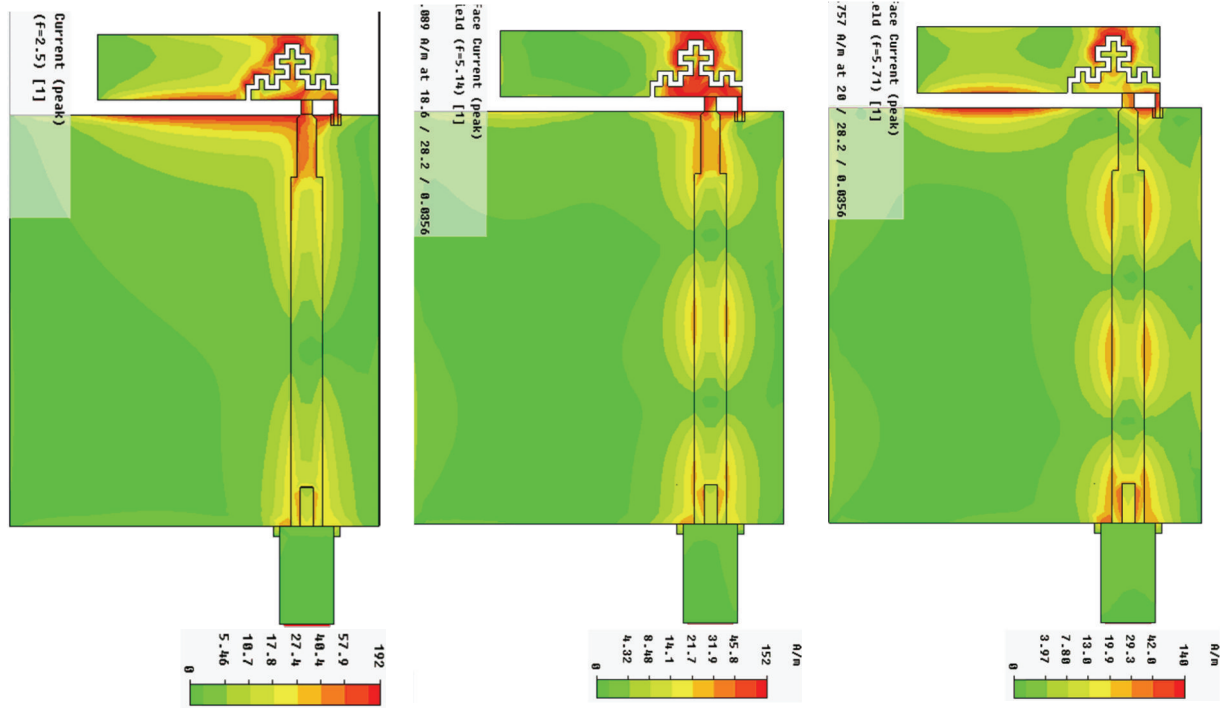


FIGURE 7: Surface current distributions of the dual-band GK2 PIFA at 2.5 GHz, 5.14 GHz and 5.71 GHz.

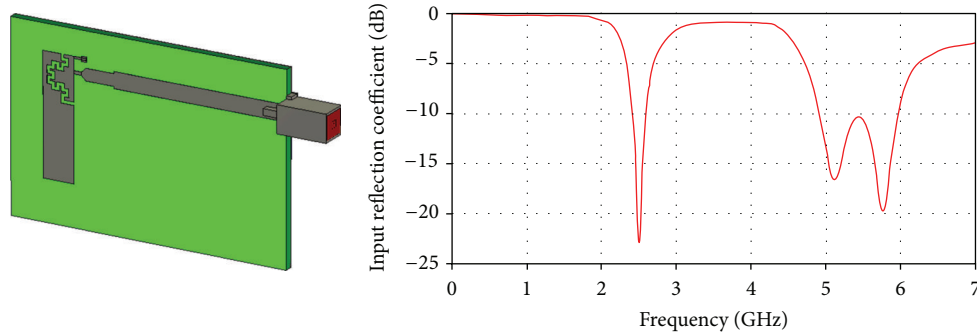


FIGURE 8: The computational model of the dual-band D-GK2 PIFA in perspective and the magnitude of its input reflection coefficient in the range DC-7 GHz.

The width of the ground plane should be at least large enough to accommodate the main arm of the PIFA. Furthermore, small extensions are also required: towards the open-circuited end of the PIFA, the substrate and ground plane should be extended by  $8 \leq w_1 \leq 10$  mm. Towards the short-circuited end of the PIFA, the substrate and ground plane should be extended by  $3 \leq w_2 \leq 5$  mm. Changes in  $w_1$  affect both resonances significantly, so this parameter must be chosen carefully. Changes in  $w_2$  only affect the upper resonance; the lower one is practically insensitive. Note that the values suggested above are frequency-dependent.

The results presented in Sections 3.1–3.4 correspond to the common ground plane length  $L_{\text{gnd}} = 40$  mm. This common length is equal to  $\lambda/3$  at 2.5 GHz and  $3\lambda/4$  at 5.5 GHz. Table 3 lists the ranges of ground length that produce maximum absolute bandwidth and total efficiency

for each antenna and frequency band. It seems that optimally compensatory ground length equals  $L'_{\text{gnd}} = 32$  mm. This length is equal to  $0.27\lambda$  at 2.5 GHz and  $0.59\lambda$  at 5.5 GHz. The 40 mm-long ground plane was chosen because it maximizes the obtainable bandwidth at the lower band.

## 4. Discussion

**4.1. Performance of the Four Slotted PIFAs.** The results given in Section 3 lead to conclusions and comparisons with prior studies. First, it is important to note that, in the general case, the whole structure is used at both resonances for radiation. Unlike what was suggested in prior studies [9], the current distributions indicate that the slot does not divide the antenna element in two separate radiators, that is, it does not facilitate the creation of two resonant current paths.

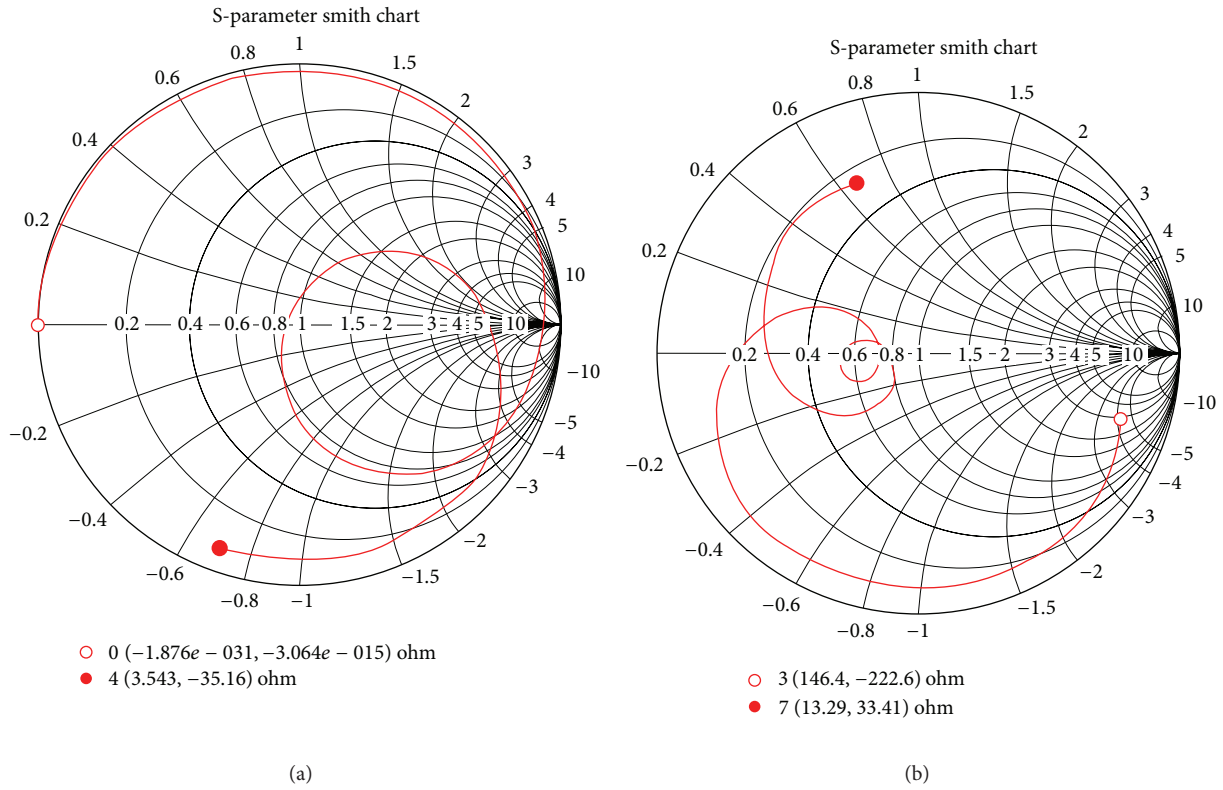


FIGURE 9: Smith chart of the complex reflection coefficient of the dual-band D-GK2 PIFA in the overlapping frequency ranges DC-4 GHz and 3-7 GHz.

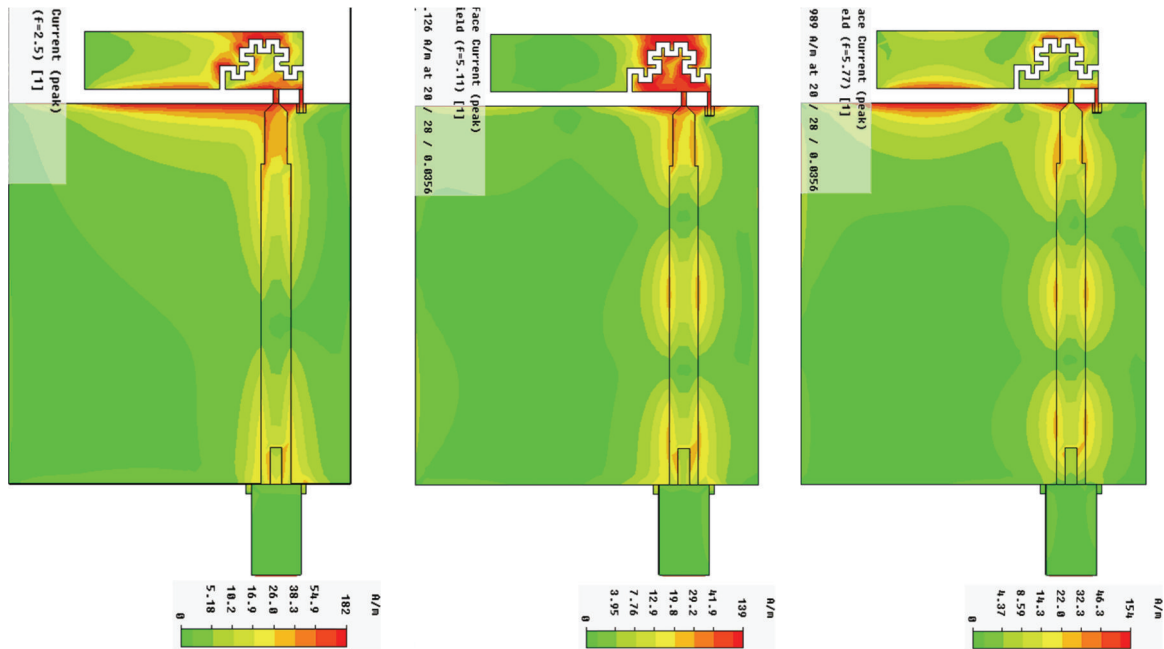


FIGURE 10: Surface current distributions of the dual-band D-GK2 PIFA at 2.5 GHz, 5.11 GHz, and 5.77 GHz.

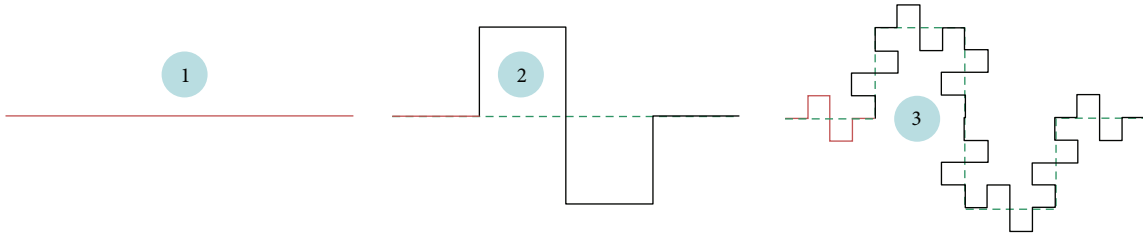


FIGURE 11: The first two iterations,  $i = 0 \rightarrow 2$ , of the hybrid meander-Koch curve for the optimum case of  $n = 4$  subdivisions.

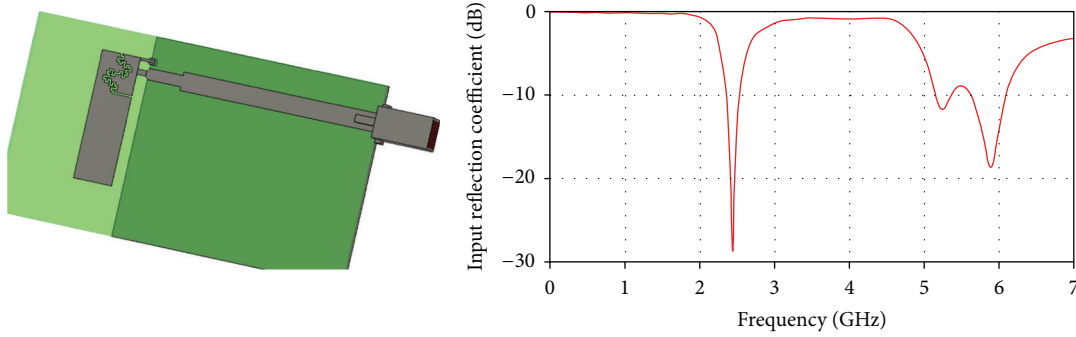


FIGURE 12: The computational model of the dual-band MK2 PIFA in perspective and the magnitude of its input reflection coefficient in the range DC-7 GHz.

TABLE 3: Comparison of well-performing GNDP lengths between the four dual-band printed IFAs in terms of bandwidth and efficiency.

Band (GHz)	K2		GK2		D-GK2		MK2	
	2-3	5-6	2-3	5-6	2-3	5-6	2-3	5-6
Maximum BW (GHz) at $L_{\text{gnd}}$ (mm)	0.23 36-40	0.96 28	0.18 36-44	1.40 28	0.19 32-44	1.20 32-40	0.18 32-44	1.00 28
Maximum $\overline{n_{\text{total}}}$ (%) at $L_{\text{gnd}}$ (mm)	88 32-36	87-88 28-32	83 32-44	91 28-32	84 28-44	88-90 20-36	84 28-48	87-88 28

TABLE 4: Comparison of electrical performance between the four dual-band printed IFAs in each frequency band.

Band (GHz)	K2		GK2		D-GK2		MK2	
	2-3	5-6	2-3	5-6	2-3	5-6	2-3	5-6
$f_c$ (GHz)	2.530	5.310	2.500	5.410	2.500	5.410	2.450	5.450
$BW_V$ (GHz)	0.231	0.598	0.182	1.000	0.191	1.050	0.182	0.950
FBW <sub>V</sub>	0.091	0.113	0.073	0.185	0.076	0.193	0.074	0.174
Q	7.3	5.9	9.1	3.6	8.7	3.4	9.0	3.8
$ka$ (rad)	1.60	3.35	1.56	3.38	1.57	3.41	1.50	3.20
$\overline{G_{\text{max}}}$ (dBi)	2.0	4.2	2.0	4.3	2.0	4.4	2.1	4.6
$\overline{n_{\text{rad}}}$	0.94	0.97	0.94	0.97	0.94	0.97	0.94	0.97
$\overline{n_{\text{total}}}$	0.87	0.82	0.83	0.86	0.84	0.87	0.83	0.84
FOM (dB)	-3.1	-5.6	-4.1	-3.3	-3.9	-3.1	-3.9	-3.4
$Q_r$ (dB)	+8.9	+7.8	+9.9	+5.7	+9.7	+5.4	+9.8	+5.9
$Q_i$ (dB)	+9.2	+8.6	+10.4	+6.2	+10.2	+5.9	+10.4	+6.6

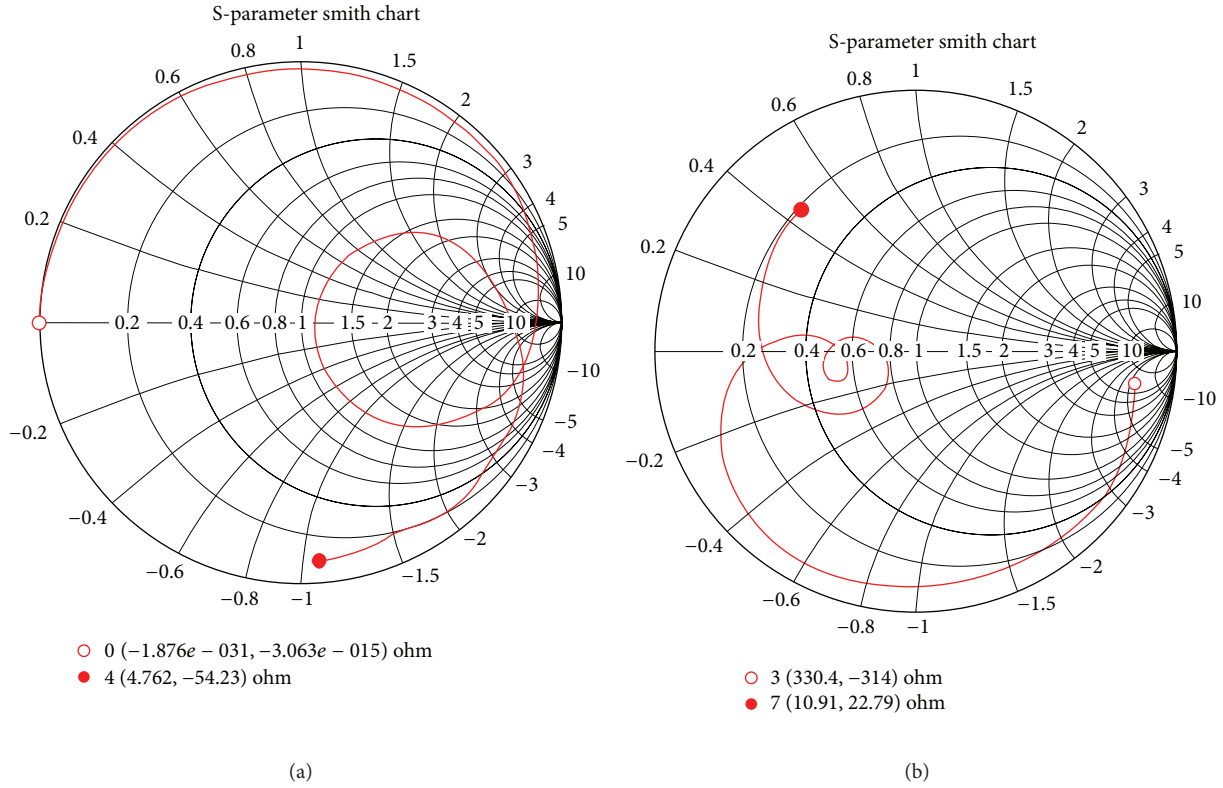


FIGURE 13: Smith chart of the complex reflection coefficient of the dual-band MK2 PIFA in the overlapping frequency ranges DC-4 GHz and 3-7 GHz.

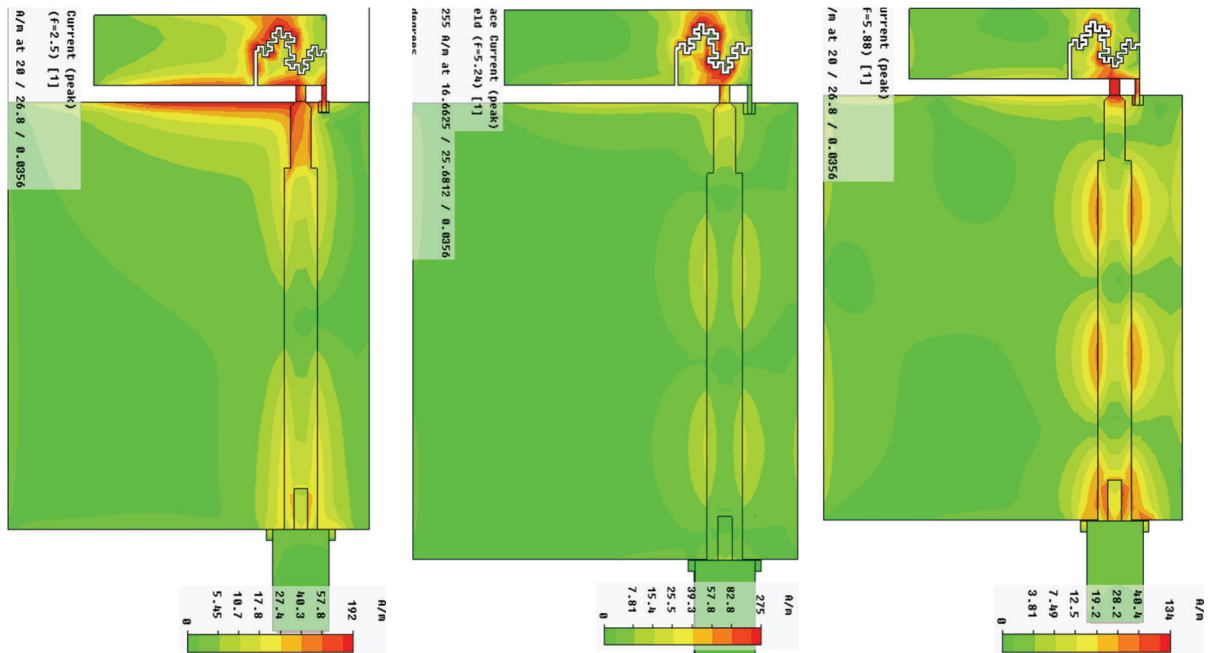


FIGURE 14: Surface current distributions of the dual-band MK2 PIFA at 2.5 GHz, 5.24 GHz, and 5.88 GHz.

Rather, it provides the proper reactive loading (or “tuning reactance”) for a single-resonant PIFA to become dual band. The computational models corroborate Boyle’s theoretical treatment [5, 23, 24].

Referring to the results tabulated in Table 4, the four dual-band PIFAs meet the specifications that were set for the fractional bandwidth, the electrical size, and the mean total radiation efficiency. The choice of a low-loss substrate leads

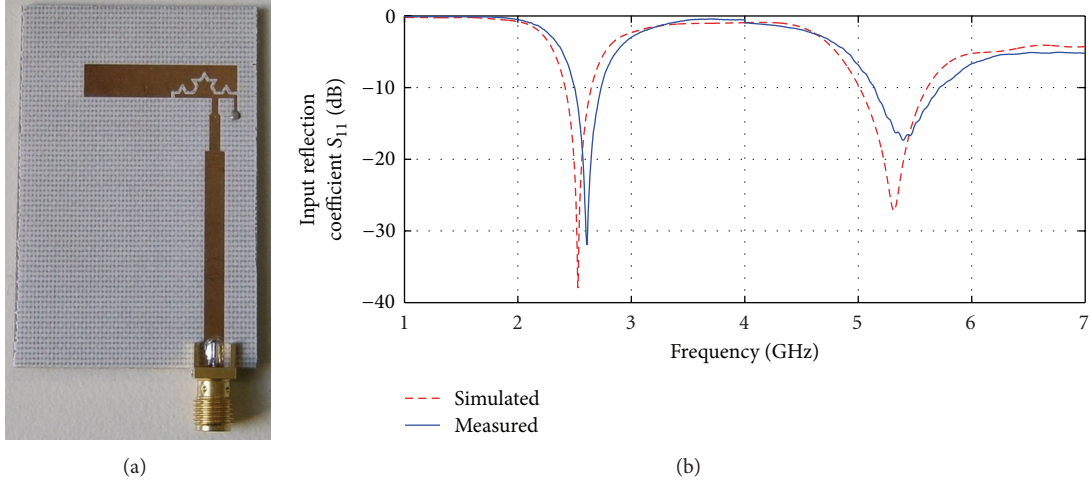


FIGURE 15: (a) Prototype dual-band PIFA reactively loaded by a K2 slot. (b) Comparison of numerical and experimental magnitudes of the reflection coefficient at the input to the dual-band K2 PIFA.

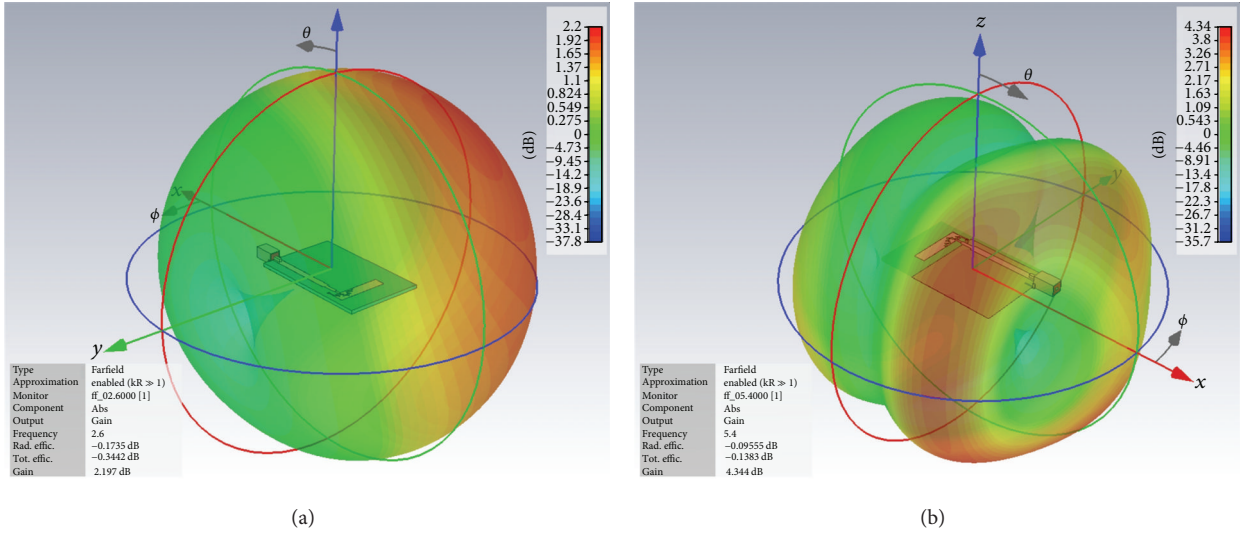


FIGURE 16: Numerically estimated three-dimensional gain patterns of the K2 PIFA at (a) 2.6 GHz and (b) 5.4 GHz. Notice the different amplitude scales (both are given in dBi).

to mean radiation efficiencies in the range 94–97%, that is,  $-0.3 \leq \overline{n}_{\text{rad}} \leq -0.1$  dB. All eight FoM levels take on negative values in decibels. In the lower band, the low FoM values are due to the reduced bandwidth, whereas in the upper band they result from the increased electrical size: in the 5–6 GHz range all four slotted PIFAs are electrically large ( $ka > 2$  rad), a fact that is also attested by the corresponding mean gain values (gain averaged over each band). The expression for the dimensionless figure of merit in decibels is repeated here for convenience,

$$\text{FOM} = 10 + 10 \log(\overline{n}_{\text{total}}) + 10 \log(\text{FBW}) - 10 \log(ka). \quad (3)$$

Karilainen et al. [35] suggested the use of the *radiation quality factor*,  $Q_r$ , for the comparison of overall performance

of antennas featuring different shapes, volumes, and resonant frequencies,

$$Q_r = \frac{Q}{n_{\text{rad}}}. \quad (4)$$

Taking mismatch losses also into account, the *total radiation quality factor*,  $Q_t$ , is proposed here in order to evaluate the performance of the antenna system,

$$Q_t = \frac{Q}{n_{\text{total}}}. \quad (5)$$

The values of the dimensionless  $Q_r$  and  $Q_t$  in decibels are also tabulated in Table 4 (actually, the former is given as  $Q/\overline{n}_{\text{rad}}$ ). The goal of any given design is to maximize FOM and minimize both  $Q_r$  and  $Q_t$ . All three metrics paint the same

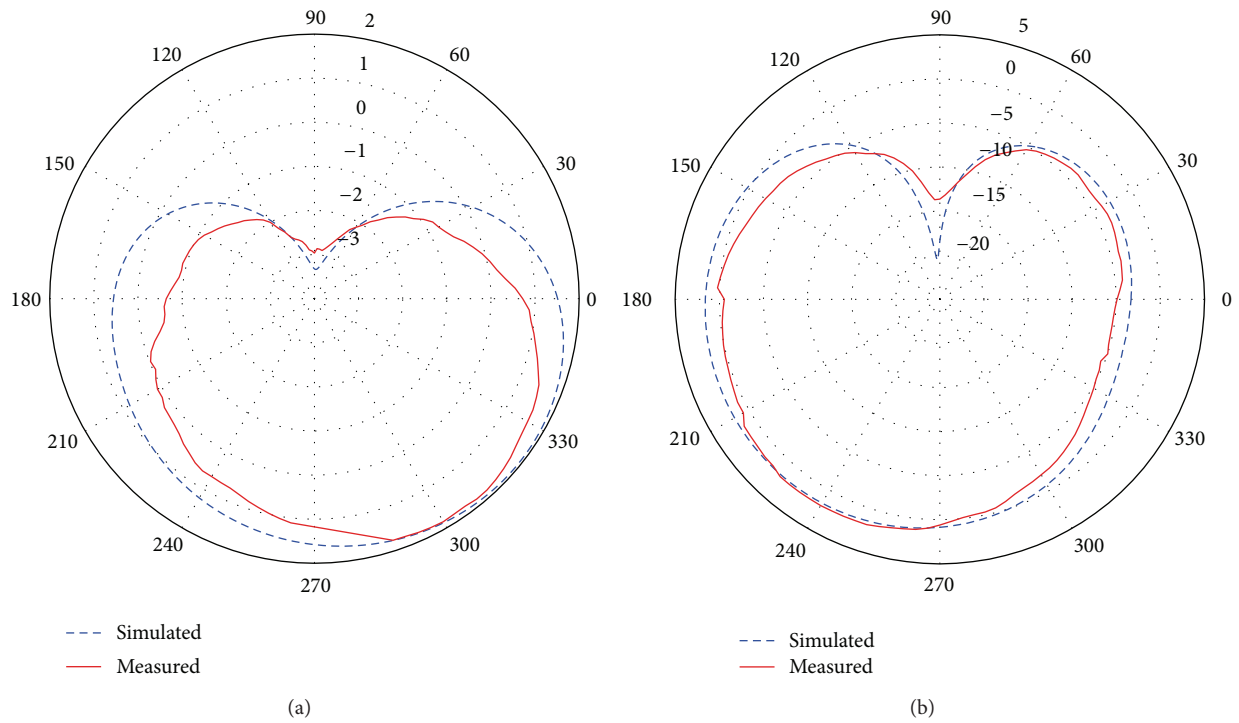


FIGURE 17: Comparison of numerical and experimental gain pattern cuts at 2.6 GHz recorded at the principal planes (a)  $\phi = 0$  and (b)  $\theta = \pi/2$ . Notice the different radial scales (both are given in dBi).

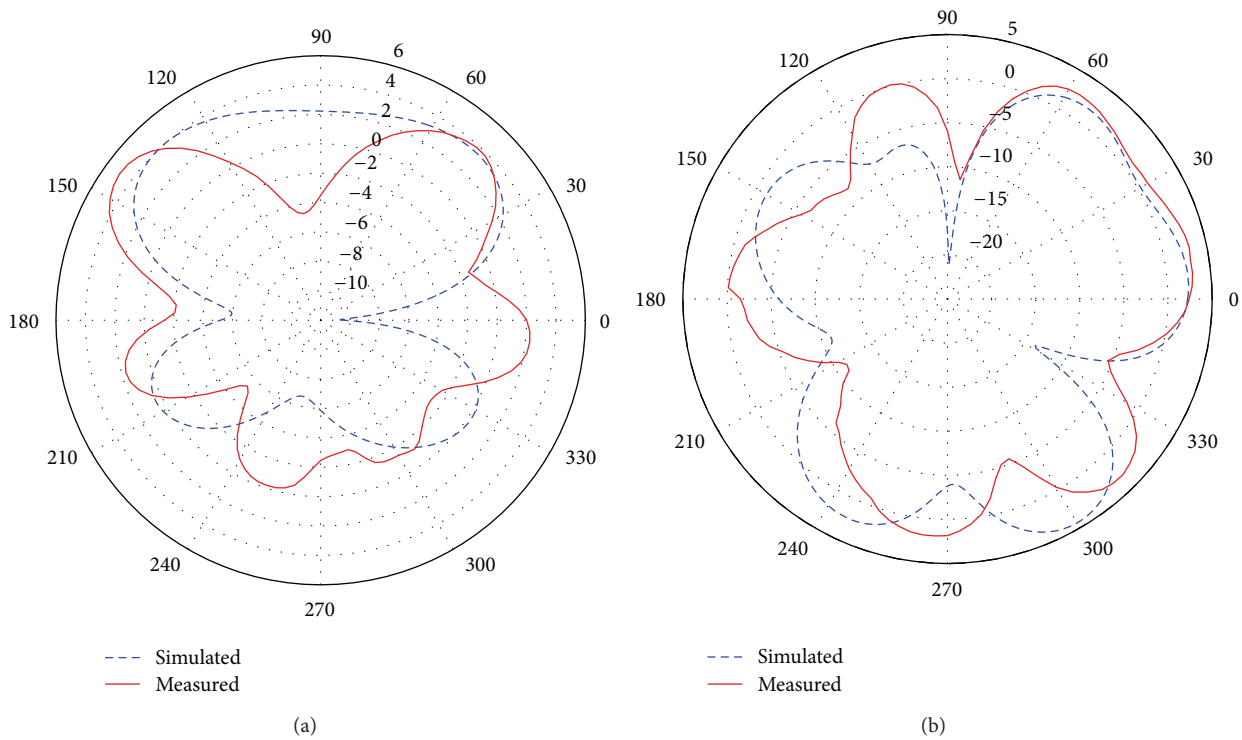


FIGURE 18: Comparison of numerical and experimental gain pattern cuts at 5.4 GHz recorded at the principal planes (a)  $\phi = 0$  and (b)  $\theta = \pi/2$ . Notice the different radial scales (both are given in dBi).

TABLE 5: Aggregate absolute and fractional bandwidths achieved by the four proposed dual-band PIFAs.

	K2	GK2	D-GK2	MK2
$BW_{V\ell} + BW_{Vu}$ (GHz)	0.829	1.182	1.241	1.132
$FBW_{V\ell} + FBW_{Vu}$	0.204	0.258	0.269	0.248

picture with regard to the differential overall performance of the four proposed slotted PIFAs.

Table 5 lists the aggregate bandwidth, absolute and fractional, that was achieved by each PIFA. By comparison of these bandwidth values to the ones given in [26], one concludes that there exist clear indications that the cumulative absolute bandwidth of each antenna is significantly increased. However, this is a superficial conclusion, and it results from the high centre frequency of the upper band, which is more than double the centre frequency of the lower band. The most appropriate indicator of impedance bandwidth is the fractional bandwidth: Table 5 indicates that the aggregate FBW that an antenna, either a single-band or a multi-band one, can yield is strictly limited. Therefore, it is not actually feasible to extract more bandwidth from an antenna by simply triggering more and more resonances. The aggregate FBW of any given antenna is also given, in the sense that it is an intrinsic quality of that particular antenna configuration. The only aspect that the designer can actually influence is how the available fractional bandwidth will be distributed amongst the desired frequency bands.

#### 4.2. Comments on Prior Studies and Performance Comparison.

As mentioned in Section 1.1, the only existing study on dual-band antennas for wireless sensors is the work of Mendes et al. [10]. They designed a chip-size, multilayered, planar IFA for operation at 2.4 and 5.7 GHz. It achieved 50 MHz of bandwidth at 2.4 GHz (2.1% fractional) and 170 MHz at 5.7 GHz (3.0%). The overall size of the radiator was 6 mm × 8.5 mm × 4.5 mm. The circumscribing sphere had a radius  $a_1 = 5.7$  mm, which corresponds to an electrical size equal to  $(ka)_1 = 0.29$  rad  $\ll$  1 rad. The definition of electrical size is given in [26, 34]. Based on data reported in [10], the quality factor of the chip-size planar IFA was estimated at  $Q = 31.6$ . However, the lower bound on  $Q$ , that is, the well-known Chu-Harrington-McLean limit, is equal to  $Q_{\ell b} = 37.6$ . One possible explanation for the discrepancy is the effect of the coaxial connector on this electrically small antenna. The antenna operates in dipole mode; hence, there exist radiating currents on the outer sheath of the coaxial connector. If this is indeed the case, then the connector must be included in the circumscribing sphere. The height of the antenna increases from 4.5 mm to 14.5 mm, and the electrical size becomes  $(ka)'_1 = 0.45$  rad  $\ll$  1 rad. The lower bound on  $Q$  becomes  $Q'_{\ell b} = 13.2$ , hence no violation occurs.

Moving on to the comparison, Table 6 lists the electrical sizes, fractional bandwidths, and aggregate fractional BWs that were obtained from the literature survey. Note that the estimation of all electrical sizes was based on the assumption that the whole extent of the finite GNDP contributes to the

radiation mechanism. The same policy was applied to the four slotted PIFAs (see Table 4). It is also the reason why the work of Wong and Chen [20] was excluded from the comparison; all results reported therein had the antenna mounted on the lid of a laptop, which provided the antenna with an electrically large ground plane. All other structures discussed herein involve strictly finite GNDPs, hence the comparison would not be meaningful.

The aggregate bandwidths listed in Table 6 range between 5–32%, since the listed PIFAs vary in size from electrically small to electrically very large. All bandwidths were calculated at  $VSWR = 1.92 : 1$ , that is, at a reflection level equal to  $-10$  dB. The aggregate bandwidths of the four slotted PIFAs described herein compare favourably with those reported in prior works. The twelve referenced studies can be divided into three main categories:

- (1) PIFA structures that are electrically larger and still produce a smaller aggregate bandwidth compared to the four slotted PIFAs [9, 16–18],
- (2) PIFA structures that are electrically smaller and produce a smaller aggregate bandwidth compared to the four slotted PIFAs either because they are smaller, or because they are *planar* IFAs [10, 11, 14, 15, 21], and
- (3) PIFA structures that are electrically smaller but manage to produce greater aggregate bandwidths compared to the four slotted PIFAs [12, 13, 19].

The design of the four slotted PIFAs opted for maximization of the bandwidth of the lower resonance, hence the antennas reported herein perform worse compared to design approaches that maximized the upper band or both. Moreover, the electrical size of the slotted PIFAs was influenced not only by the maximization of the lower bandwidth, but also by the need for available real-estate on the PCB to solder the RF and baseband electronics of the wireless sensors. Last but not least, the dual-band technique reported herein also achieves design simplicity and low cost of fabrication.

## 5. Measurement Results

Figure 15(a) depicts a fabricated, dual-band, printed IFA that has been reactively loaded with a Koch-shaped slot of the second iteration (K2). The antenna was fabricated on TRF-45 laminated substrate [31]. Parameter values are in accordance with Table 2.

Measurements were conducted in an fully anechoic chamber (far-field test site), suitable for antenna characterization in the range 0.8–40 GHz. The reference antenna was spaced by 4.7 m from the antenna under test (AUT), that is, by approximately  $39\lambda$  at 2.5 GHz. Both AUT and reference antenna were connected through low-loss coaxial cables to the ports of an E8358A vector network analyzer (VNA) [36], which recorded the complex scattering parameters. The settings that were applied to the VNA are listed in Table 7. The measurements were done over two consecutive 3 GHz-wide bands.

**5.1. Measured Input Impedance.** The result illustrated in Figure 15(b) firstly shows that there is a lower-frequency band exhibiting a resonance at  $f_{0,\ell} = 2.610$  GHz, a centre frequency  $f_{c,\ell} = 2.618$  GHz, and an operational bandwidth  $BW_{\ell} = 0.235$  GHz. The corresponding fractional bandwidth is  $FBW_{\ell} = 0.090$ .

At the same time, an upper operating band exists in the 5-6 GHz range. It exhibits a resonance at  $f_{0,h} = 5.395$  GHz, a centre frequency  $f_{c,h} = 5.428$  GHz, and an operational bandwidth  $BW_h = 0.575$  GHz. The corresponding fractional bandwidth is  $FBW_h = 0.106$ .

The results stated above lead to an aggregate absolute bandwidth equal to  $BW_{\ell} + BW_h = 0.810$  GHz. The aggregate fractional bandwidth is equal to  $FBW_{\ell} + FBW_h = 0.196$ . The results reported in this section compare favourably with the corresponding numerical results listed in Tables 4 and 5. The relative error in centre frequencies is equal to +3.5% and +2.2% for the lower and upper band, respectively. Similarly, the differences in absolute bandwidth are +1.7% and -3.8%, whereas the errors in fractional bandwidth read -1.1% and -5.3%. Finally, the deviation in aggregate absolute and fractional bandwidth is -2.3% and -3.9%, respectively.

**5.2. Measured Far-Field Patterns.** The far-field patterns of the K2 PIFA were measured at 2.6 and 5.4 GHz. For the convenience of the reader, the computed three-dimensional patterns of the antenna at these two frequencies are illustrated in Figure 16. The antenna lies on the  $xy$ -plane, as shown by the coordinate system in Figure 16. The surface currents depicted in Figures 4, 7, 10, and 14 indicate that the radiating currents feature strong  $x$ - and  $y$ -components. The orthogonal currents are phased randomly. Thus, as anticipated, the four printed IFAs are elliptically polarized in the general case. Therefore, the gain amplitudes given in Figure 16 correspond to the vectorial sum of the  $\theta$ - and  $\phi$ -components of the  $\mathbf{E}$ -field.

The far-field measurements discussed here report on the results that were harvested from the  $\phi = 0$  and  $\theta = \pi/2$  principal planes. The reference antenna was a linearly polarized, standard-gain horn; hence, the  $\theta$  (vertical) and  $\phi$  (horizontal) components of the far field were measured separately. The results are grouped in Figures 17 and 18; the gain amplitudes again correspond to the vectorial sum of the  $\theta$ - and  $\phi$ -components of the  $\mathbf{E}$ -field.

At 2.6 GHz there is good agreement between computed and measured patterns, especially in the  $\theta = \pi/2$  cut. The directions of maxima and minima have been predicted with considerable accuracy. In the  $\phi = 0$  cut, the measured maximum IEEE gain lags the computed one by 0.1 dB (1.9 dBi versus 2.0 dBi). On the other hand, in the  $\theta = \pi/2$  cut, the measured maximum gain exceeds the computed one by 0.2 dB (2.1 dBi versus 1.9 dBi). A deviation on the order of  $\pm 0.2$  dB lies within the measurement uncertainty of the VNA [36], which can be estimated by the instrument settings listed in Table 7.

At 5.4 GHz the agreement between computed and measured patterns becomes worse, particularly in the  $\phi = 0$  cut. Significant null filling is observed, together with angular

shifting of the side lobes. The deviant behaviour is attributed to radiation from the feed cable, which amplifies the  $\theta$ -component, and to scattering from the mounting pole and tripod; according to the  $2D^2/\lambda$  rule, the reactive and radiating near field of the antenna occupies twice the space when firing in the upper band. Nevertheless, in the  $\phi = 0$  cut, the measured maximum IEEE gain exceeds the computed one by 0.9 dB (4.9 dBi versus 4.0 dBi). On the other hand, in the  $\theta = \pi/2$  cut, the measured maximum gain lags the computed one by 1.2 dB (3.2 dBi versus 4.4 dBi).

## 6. Conclusion

Dual-band communication can play a significant role in current and future wireless sensor networks. Given the scarcity of relevant proper radiators, this paper described how printed antennas can be efficiently designed as simple, compact, device-integrated, dual-band antennas. During the evolution of modern antennas, the planar IFA inherited the properties of the microstrip “patch” antenna, while the printed IFA inherited those of the printed monopole. Printed monopoles are well-known wideband radiators; patch antennas are not. Reactive tuning of printed IFAs was applied in the form of four slotted configurations, in order to exert as much aggregate bandwidth as possible for use in two well-known unlicensed bands.

Electrical performance was characterized through numerous computed results. Slot loading showed a potential to increase the impedance bandwidth compared to prior implementations in terms of achievable  $FBW_v$ . The study of SCDs revealed that most of the area of the element is used for radiation at both resonances. In radiation terms, the antennas provided satisfactory gains and high efficiencies ( $\geq 82\%$ ). A simple figure of merit was used to compare the performance of the three PIFAs head to head. The final comparison displayed in an emphatic way that modern antenna design is an art of compromise.

By exploring the potential for operation at 2.5 GHz and 5.5 GHz, it was discovered that a simple change in slot geometry can almost double the achievable operational bandwidth. Thus, the proposed antennas not only serve the 5.15–5.35 GHz U-NII band, but also the 5.725–5.875 GHz ISM band. The proposed dual-band structures exhibited at the lower band an electrical size less or equal to that of the half-wavelength dipole. Nonetheless, these antennas can indeed be considered compact, even though they are not electrically small *per se*, since their dual-band capability enables them to do the job of two and even three separate antennas. Meanwhile, an educated choice of substrate can enable the combination of ease of fabrication and high radiation efficiency even at mid-C-band.

Yet another important design element that this study of dual-band antennas highlighted is that the aggregate fractional bandwidth of a PIFA is bounded within certain limits, and by degenerating higher-order radiating modes the designer merely re-distributes whatever bandwidth is available by the antenna itself to the desired frequency bands.

TABLE 6: Electrical sizes, fractional bandwidths, and aggregate fractional bandwidths from the literature survey.

Reference work	Lower band		Upper band		Aggr. FBW
	$ka$ (rad)	FBW	$ka$ (rad)	FBW	
Angelopoulos et al. [9]	3.03	0.086	6.47	0.063	0.149
Mendes et al. [10]	0.45	0.021	1.07	0.030	0.051
Moon et al. [11]	0.79	0.041	1.90	0.145	0.186
Cho et al. [12]	0.60	0.057	1.39	0.261	0.318
Nakano et al. [13]	1.11	0.041	2.65	0.282	0.323
Azad and Ali [14]	1.13	0.070	2.36	0.033	0.103
Cho et al. [15]	1.33	0.045	3.02	0.162	0.207
Wang et al. [16] (spiralised tail)	1.97	0.057	4.22	0.144	0.201
Wang et al. [16] (coupling element)	1.94	0.098	4.15	0.128	0.226
Michailidis et al. [17]	1.72	0.095	3.59	0.137	0.232
Chan et al. [18]	2.09	0.109	2.83	0.036	0.145
Yu and Choi [19]	1.14	0.187	2.51	0.153	0.340
Li et al. [21] (IFA mode)	1.16	0.085	3.04	0.078	0.163

TABLE 7: Settings applied to the network analyzer during the measurement of the K2 PIFA.

Network analyzer settings	
Span (Cal + Meas)	1–4 GHz and 4–7 GHz
IF bandwidth	5 kHz
Number of points	601 ( $\Delta f = 5$ MHz)
Sweep time	128 msec (manual)
Averaging (full span)	32 (15 dB)

## Acknowledgments

C. Kakoyiannis thanks Dr. T. Zervos and Dr. A. Alexandridis, both with the Wireless Communications Laboratory, Institute of Informatics and Telecommunications, NCSR “Demokritos,” Athens, Greece, for assisting with the antenna measurements that were conducted in the anechoic facility of the institute. The authors wish to acknowledge Taconic Advanced Dielectric Division (Mullingar, Ireland, and Cheonan, South Korea) for donating the TRF-45 laminated substrate, which was used for design and fabrication of all antennas described herein. This work is part of the “MAGELLAN” research project, implemented within the framework of the “THALIS” Research Programme (NSRF 2007–2013), and co-financed by the Greek Ministry of Education and Religious Affairs, Culture and Sports and the European Union.

## References

- [1] P. S. Hall, E. Lee, and C. T. P. Song, “Planar inverted-F antennas,” in *Printed Antennas for Wireless Communications*, R. Waterhouse, Ed., chapter 7, pp. 197–228, John Wiley & Sons, Chichester, UK, 2007.
- [2] B. S. Collins, “Handset antennas,” in *Antennas for Portable Devices*, Z. N. Chen, Ed., chapter 2, John Wiley & Sons, Chichester, UK, 2007.
- [3] Y. C. Vardaxoglou and J. R. James, “Mobile handset antennas,” in *Antenna Engineering Handbook*, J. L. Volakis, Ed., chapter 36, McGraw-Hill, New York, NY, USA, 4th edition, 2007.
- [4] Z. Ying, M. Ohtsuka, Y. Nishioka, and K. Fujimoto, “Antennas for mobile terminals,” in *Mobile Antenna Systems Handbook*, K. Fujimoto, Ed., chapter 5, pp. 213–320, Artech House, Norwood, Mass, USA, 3rd edition, 2008.
- [5] K. Boyle, “Multiband multisystem antennas in handsets,” in *Multiband Integrated Antennas for 4G Terminals*, D. A. Sánchez-Hernández, Ed., chapter 2, pp. 33–52, Artech House, Norwood, Mass, USA, 2008.
- [6] M. Martínez-Vázquez, E. Antonino-Daviú, and M. Fábado-Cabrés, “Miniaturized integrated multiband antennas,” in *Multiband Integrated Antennas for 4G Terminals*, D. A. Sánchez-Hernández, Ed., chapter 5, pp. 151–186, Artech House, Norwood, Mass, USA, 2008.
- [7] Y. Rahmat-Samii, J. Guterman, A. A. Moreira, and C. Peixeiro, “Integrated antennas for wireless personal communications,” in *Modern Antenna Handbook*, C. A. Balanis, Ed., chapter 22, pp. 1079–1142, John Wiley & Sons, Hoboken, NJ, USA, 2008.
- [8] K. Fujimoto, “Antennas for mobile communications,” in *Modern Antenna Handbook*, C. A. Balanis, Ed., chapter 23, pp. 1143–1228, John Wiley & Sons, Hoboken, NJ, USA, 2008.
- [9] E. S. Angelopoulos, A. I. Kostaridis, and D. I. Kaklamani, “A novel dual-band f-inverted antenna printed on a PCMCIA card,” *Microwave and Optical Technology Letters*, vol. 42, no. 2, pp. 153–156, 2004.
- [10] P. M. Mendes, A. Bartek, J. N. Burghartz, and J. H. Correia, “Novel very small dual-band chip-size antenna for wireless sensor networks,” in *Proceedings of the IEEE Radio and Wireless Conference (RAWCON '04)*, pp. 419–422, Atlanta, Ga, USA, September 2004.
- [11] J. I. Moon, D. U. Sim, and S. O. Park, “Compact PIFA for 2.4/5 GHz dual ISM-band applications,” *Electronics Letters*, vol. 40, no. 14, pp. 844–846, 2004.
- [12] Y. J. Cho, S. H. Hwang, and S. O. Park, “Printed antenna with folded non-uniform meander line for 2.4/5 GHz WLAN bands,” *Electronics Letters*, vol. 41, no. 14, pp. 786–788, 2005.
- [13] H. Nakano, Y. Sato, H. Mimaki, and J. Yamauchi, “An inverted FL antenna for dual-frequency operation,” *IEEE Transactions on Antennas and Propagation*, vol. 53, no. 8, pp. 2417–2421, 2005.
- [14] M. Z. Azad and M. Ali, “A miniaturized hilbert PIFA for dual-band mobile wireless applications,” *IEEE Antennas and Wireless Propagation Letters*, vol. 4, no. 1, pp. 59–62, 2005.

- [15] Y. J. Cho, Y. S. Shin, and S. O. Park, "Internal PIFA for 2.4/5 GHz WLAN applications," *Electronics Letters*, vol. 42, no. 1, pp. 8–9, 2006.
- [16] Y. S. Wang, M. C. Lee, and S. J. Chung, "Two PIFA-related miniaturized dual-band antennas," *IEEE Transactions on Antennas and Propagation*, vol. 55, no. 3, pp. 805–811, 2007.
- [17] E. Michailidis, C. C. Tsimenidis, and E. G. Chester, "Parametric study of dual and wide band PIFA," in *Proceedings of the IET Seminar on Wideband Multiband Antennas and Arrays for Defence or Civil Applications*, pp. 145–159, London, UK, March 2008.
- [18] P. W. Chan, H. Wong, and E. K. N. Yung, "Dual-band printed inverted-F antenna for DCS, 2.4 GHz WLAN applications," in *Proceedings of the Loughborough Antennas and Propagation Conference (LAPC '08)*, pp. 185–188, Loughborough, UK, March 2008.
- [19] Y. Yu and J. Choi, "Compact internal inverted-F antenna for USB dongle applications," *Electronics Letters*, vol. 45, no. 2, pp. 92–94, 2009.
- [20] K. L. Wong and W. J. Chen, "Small-size microstrip-coupled printed PIFA for 2.4/5.2/5.8 GHz WLAN operation in the laptop computer," *Microwave and Optical Technology Letters*, vol. 51, no. 9, pp. 2072–2076, 2009.
- [21] Y. Li, Z. Zhang, J. Zheng, Z. Feng, and M. F. Iskander, "A compact hepta-band loop-inverted F reconfigurable antenna for mobile phone," *IEEE Transactions on Antennas and Propagation*, vol. 60, no. 1, pp. 389–392, 2012.
- [22] N. Cho, J. Bae, and H. J. Yoo, "A 10.8 mW body channel communication/MICS dual-band transceiver for a unified body sensor network controller," *IEEE Journal of Solid-State Circuits*, vol. 44, no. 12, pp. 3459–3468, 2009.
- [23] K. Boyle, *Antennas for multi-band RF front-end modules [Ph.D. thesis]*, Delft University of Technology, Delft, The Netherlands, 2004.
- [24] K. R. Boyle and L. P. Ligthart, "Radiating and balanced mode analysis of PIFA antennas," *IEEE Transactions on Antennas and Propagation*, vol. 54, no. 1, pp. 231–237, 2006.
- [25] Z. D. Liu, P. S. Hall, and D. Wake, "Dual-frequency planar inverted-F antenna," *IEEE Transactions on Antennas and Propagation*, vol. 45, no. 10, pp. 1451–1458, 1997.
- [26] C. G. Kakoyiannis, A. Kyrlikitsi, and P. Constantinou, "Bandwidth enhancement, radiation properties and ground-dependent response of slotted antennas integrated into wireless sensors," *IET Microwaves, Antennas and Propagation*, vol. 4, no. 5, pp. 609–628, 2010.
- [27] C. Puente, J. Romeu, and A. Cardama, "Fractal-shaped antennas," in *Frontiers in Electromagnetics*, D. Werner and R. Mittra, Eds., chapter 2, pp. 48–93, IEEE Press, New York, NY, USA, 2000.
- [28] J. P. Gianvittorio and Y. Rahmat-Samii, "Fractal antennas: a novel antenna miniaturization technique, and applications," *IEEE Antennas and Propagation Magazine*, vol. 44, no. 1, pp. 20–36, 2002.
- [29] D. H. Werner and S. Ganguly, "An overview of fractal antenna engineering research," *IEEE Antennas and Propagation Magazine*, vol. 45, no. 1, pp. 38–57, 2003.
- [30] W. J. Krzystofik, "Printed multiband fractal antennas," in *Multiband Integrated Antennas for 4G Terminals*, D. A. Sánchez-Hernández, Ed., chapter 4, pp. 95–150, Artech House, Norwood, Mass, USA, 2008.
- [31] *Advanced PCB Materials Product Selection Guide*, Taconic, Petersburg, NY, USA, 2010.
- [32] T. Weiland, M. Timm, and I. Munteanu, "A practical guide to 3-D simulation," *IEEE Microwave Magazine*, vol. 9, no. 6, pp. 62–75, 2008.
- [33] I. Munteanu, M. Timm, and T. Weiland, "It's about time," *IEEE Microwave Magazine*, vol. 11, no. 2, pp. 60–69, 2010.
- [34] C. G. Kakoyiannis and P. Constantinou, "Radiation properties and ground-dependent response of compact printed sinusoidal antennas and arrays," *IET Microwaves, Antennas and Propagation*, vol. 4, no. 5, pp. 629–642, 2010.
- [35] A. O. Karilainen, P. M. T. Ikonen, C. R. Simovski et al., "Experimental studies on antenna miniaturisation using magneto-dielectric and dielectric materials," *IET Microwaves, Antennas and Propagation*, vol. 5, no. 4, pp. 495–502, 2011.
- [36] *Agilent PNA Series RF Network Analyzers E8356/7/8A, E8801/2/3A, N3381/2/3A Data Sheet*, Agilent Technologies Inc., Santa Rosa, Calif, USA, 2006.

## Research Article

# Dual-Band Antenna/AMC Combination for RFID

**M. E. de Cos and F. Las-Heras**

*Area de Teoría de la Señal y Comunicaciones, Departamento de Ingeniería Eléctrica, Universidad de Oviedo, Edificio Polivalente, Modulo 8, Campus Universitario de Gijón, Asturias, 33203 Gijón, Spain*

Correspondence should be addressed to M. E. de Cos, medecos@tsc.uniovi.es

Received 27 February 2012; Accepted 18 May 2012

Academic Editor: Leena Ukkonen

Copyright © 2012 M. E. de Cos and F. Las-Heras. This is an open access article distributed under the Creative Commons Attribution License, which permits unrestricted use, distribution, and reproduction in any medium, provided the original work is properly cited.

A novel antenna/Artificial Magnetic Conductor (AMC) combination usable in dual-band Radio Frequency Identification (RFID) tags over metallic objects is presented. A compact and low thickness prototype is manufactured and characterized in terms of return loss and radiation properties in an anechoic chamber both alone and on a metallic plate. The performance exhibited by the presented antenna/AMC prototype is proper for RFID tags on both metallic and nonmetallic objects.

## 1. Introduction

In Radio Frequency Identification (RFID) systems, it would be desirable that the tagged objects do not have influence on the tag antenna performance. However, on the one hand if the object surface is made of a dielectric material, then the readable range is decreased due to frequency shift of the resonance frequency. On the other hand, antennas placed nearby metallic objects suffer from performance degradation. In passive RFID systems, this fact causes important problems and it hinders their global deployment [1–3]. Metallic objects seriously degrade the input impedance matching, bandwidth, radiation efficiency, and readable range of the tag antenna [4, 5]. The electromagnetic wave is greatly reflected by a conductor surface yielding a significant reduction of operating distance in RFID tags applications or total antenna malfunctioning. The negative effects increase at higher frequencies and so RFID operation in the Super High Frequency (SHF) band with tags attached to metallic objects presents an even more critical problem to be overcome.

In addition, another important question in RFID tags usable with people and wearable antennas [6–8] is the backward radiation to the human body which should be reduced as much as possible.

Different approaches have been proposed aiming to solve antennas on metals problems: patch antennas (already including a metallic ground plane) with the drawback of narrow bandwidth, new antenna designs like Planar Inverted

F Antennas (PIFAs) with the inconvenience of shorting planes not proper for flexible devices or tags, and the use of ferroelectric materials to insulate the antenna from metal, which is rather expensive.

A novel solution is proposed in this contribution combining a simple broadband antenna as a coplanar waveguide- (CPW-) fed bow-tie [9–11] with a compact dual-band Artificial Magnetic Conductor (AMC) [12] without vias. Through this combination, a dual-band compact low-cost antenna proper to be used on both dielectric and metallic objects and with reduced backward radiation [13] is obtained.

The paper is organized as follows: firstly, Section 2 describes the design of a CPW-fed bow-tie antenna for operation at 5.8 GHz. Then, Section 3 shows the design of a dual-band AMC resonating at 2.48 GHz and 5.8 GHz to be combined with the antenna, aiming to obtain a dual-band antenna and to insulate the antenna from metallic objects. Section 4 explains the characterization of the manufactured prototypes in terms of return loss and radiation patterns. Finally some conclusions are described in Section 5.

## 2. Antenna Design

Figure 1 shows the geometry of the proposed CPW-fed bow-tie antenna suitable for operating at 5.8 GHz. Double slot bow-tie geometry has been chosen as it exhibits wider bandwidth and smaller size than simple bow-tie. The antenna is

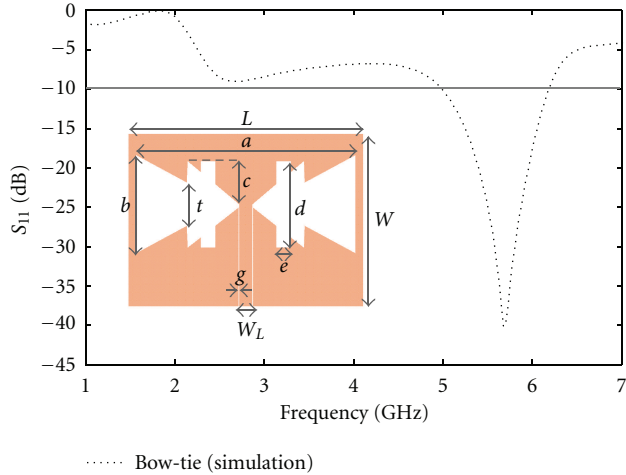


FIGURE 1: Top-view of the CPW-fed bow-tie antenna geometry. Simulation results for return loss of the CPW-fed bow-tie antenna.

TABLE 1: Bow-tie antenna dimensions.

Dimensions (mm)									
$L$	$W$	$W_L$	$g$	$a$	$b$	$c$	$d$	$e$	$t$
35	23.8	2	0.1	32.8	13.6	6	12	2.16	6

fed through a  $50\ \Omega$  CPW line with  $W_L$  strip width and  $g$  gap, and it is printed on ARLON 25N dielectric substrate with  $h = 0.762$  mm (30 mil) thickness,  $\epsilon_r = 3.28$  relative dielectric permittivity and less than 0.0025 loss tangent. There is no metallization on the backside. The antenna design and optimization have been carried out by a set of MoM simulations with commercial software [14].

The antenna resonance frequency is given by  $a$  (increasing  $a$  shifts the operating band to a lower frequency range), whereas the bandwidth and the level of the return loss at the main resonance frequency are controlled by  $b$ . A trade-off is necessary between parameters  $c$  and  $t$  as they are opposite in behavior. Increasing the value of  $c$  results in a reduction of both the frequency of operation as well as the impedance matching. Finally  $e$  and  $d$  can be, respectively, used for a fine bandwidth and frequency adjustment. Table 1 details the optimized antenna dimensions for operation at 5.8 GHz.

From simulated return loss shown in Figure 1, it can be concluded that the operating bandwidth of the bow-tie antenna is 1.235 GHz (21.26%).

### 3. Dual-Band AMC Design

An AMC is a resonating periodic structure. The resonance frequency and the AMC operation bandwidth of an AMC structure depend on the unit-cell geometry together with the dielectric substrate's relative permittivity and thickness.

Generally AMCs [15–24] are implemented by using two-dimensional periodic metallic lattices patterned on a conductor-backed dielectric surface. Recent research efforts focus on the development of low-cost AMCs easily integrable in RF, microwave, and millimeter wave circuits. Aiming

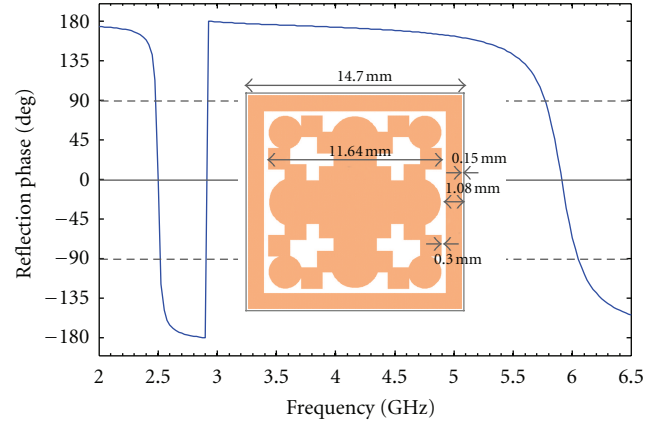


FIGURE 2: Dual-band AMC unit-cell geometry and dimensions. Simulated reflection coefficient phase of the AMC structure.

this, geometries without via holes [15] (in contrast to designs accomplished by patches with via holes [16]) as well as the use of a unilayer periodic Frequency Selective Surface (FSS) over a metallic ground plane (in contrast to multilayered FSSs [17]) should be considered. Both facts, removing via holes and using unilayer FSSs, reduce AMC operation bandwidth (which can be relevant depending on the application) and so an optimized unit-cell geometry design has to be carried out to overcome it.

The inherent in-phase reflection exhibited by AMCs makes possible the reduction of backward radiation for antennas placed on them and so by combining antenna and AMC in RFID tag design, low backward radiation to the human body can be obtained.

The unit-cell geometry presented in [24] is taken as reference to design a dual-band AMC. For this purpose the aforementioned geometry is surrounded by a rectangular frame (see Figure 2). The same dielectric substrate as for the antenna (ARLON 25N) is used. The unit-cell dimensions are optimized with Ansoft's HFSS [25] so that the AMC resonates at 2.48 GHz and 5.8 GHz. Optimized dimensions are detailed in Figure 2.

Neither via holes nor multilayer substrates are required in the low-thickness dual-band AMC, simplifying implementation and reducing its cost.

From Figure 2 it can be concluded that the structure exhibits AMC performance from 2.48 GHz to 2.51 GHz resonating at 2.49 GHz and from 5.77 GHz to 6.05 GHz resonating at 5.91 GHz. The inner geometry mainly determines the higher resonance frequency, whereas the outer square frame has more influence on the lower resonance frequency, as it can be concluded from the surface current distribution on the metallic parts of the AMC unit-cell geometry depicted in Figure 3.

The AMC performance for different polarization of the electrical incident field (under normal incidence) and under oblique incidence is very important in AMC applications for RFID tags or wearable antennas. In the case of RFID tags, the angular stability of the AMC will influence the antenna radiation performance and this will have direct impact on

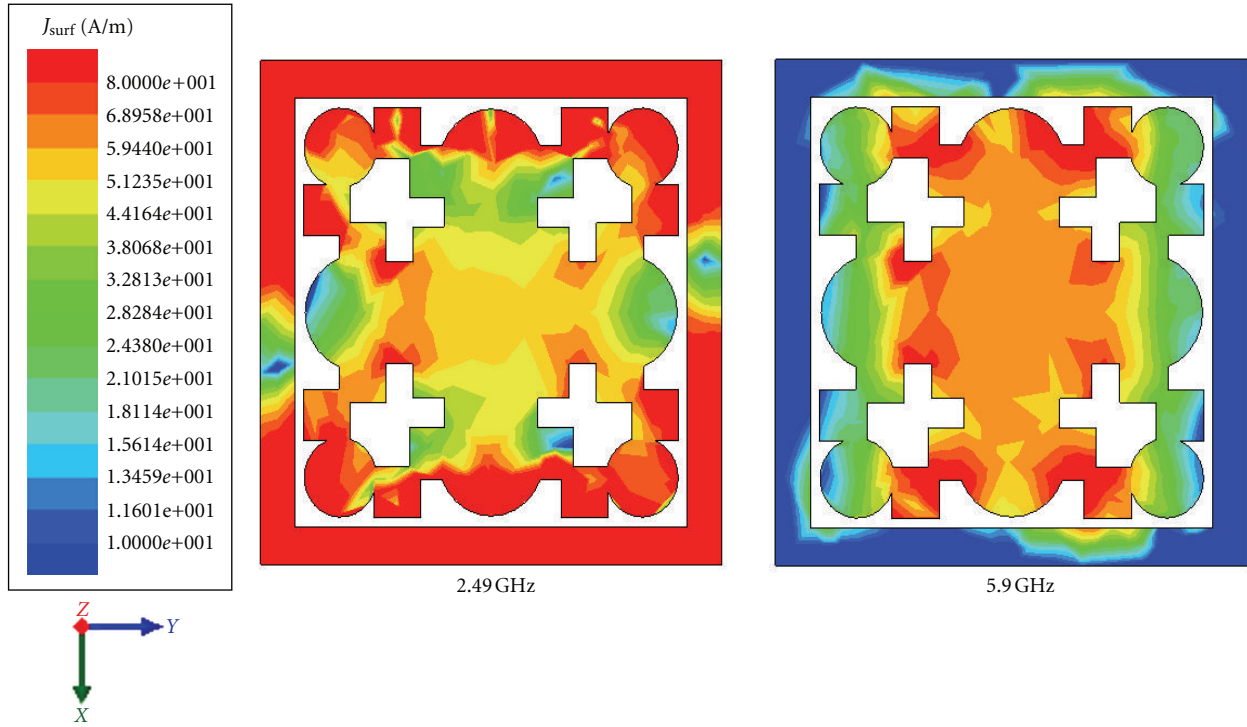


FIGURE 3: Surface currents distribution on the AMC unit-cell geometry metallic parts at 2.49 GHz and 5.9 GHz.

the angular reading range depending on the position of the reader with respect to the tagged object. So an AMC design with as higher angular stability as possible is desirable.

The AMC has been designed so that it operates identically for any polarization of the incident field (assuming normal incidence) due to the unit-cell design geometry which exhibits four symmetry planes. With the aim of studying the angular stability margin [26] of the presented structure, the reflection coefficient phase versus frequency for different incident angles  $\theta_{inc}$  between  $0^\circ$  and  $60^\circ$  has been simulated for transverse electric (TE) polarized waves. The absolute and relative deviations of the resonance frequencies can be obtained from Figure 4. For the lower frequency band: 30 MHz, 1.2% for  $\theta_{inc} = 45^\circ$  and 149 MHz, 6% for  $\theta_{inc} = 60^\circ$ . For the upper frequency band: 20 MHz, 0.3% for  $\theta_{inc} = 45^\circ$  and 100 MHz, 1.7% for  $\theta_{inc} = 60^\circ$ . The AMC operation bandwidth is slightly reduced from  $\theta_{inc} = 45^\circ$ . From these obtained results, it can be concluded that the presented AMC design is highly stable as its angular margin ranges from  $0^\circ$  to  $45^\circ$  for the lower frequency band and from  $0^\circ$  to  $60^\circ$  for the upper frequency band. The upper frequency band is more stable regarding oblique incidence.

#### 4. Characterization Results

Laser micromachining is used to manufacture prototypes (see Figure 6) of the CPW-fed bow-tie antenna alone and combined with the AMC to be characterized in terms of return loss and radiation pattern for comparison.

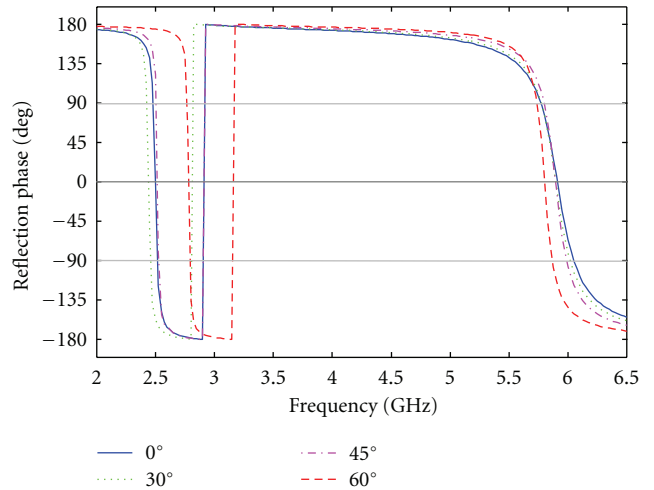


FIGURE 4: Simulated reflection phase of the AMC surface for TE polarizations for different incident angles  $\theta_{inc} = 0^\circ, 30^\circ, 45^\circ,$  and  $60^\circ$ .

4.1. Return Loss. The results of measured return loss for the manufactured prototypes are detailed in Figures 5 and 6 and Table 2.

The bow-tie antenna exhibits a measured operating bandwidth of 1.358 GHz (23.89%), which is slightly wider than the 1.235 GHz (21.66%) obtained by simulation due to the fact that the commercial MoM software considers infinite

TABLE 2: Prototypes comparison.

CPW-antenna	Frequencies (GHz)			Bandwidth	
	$f_{Low}$	$f_r$	$f_{Up}$	Total (MHz)	%
Bow-tie	—	—	—	—	—
	5124	5683	6482	1358	23.89
Bow-tie-AMC	2160	2255	2315	155	6.87
	5743	6137	6248	505	8.22
Bow-tie-AMC metallic plate	2056	2204	2285	229	10.39
	5767	5914	6588	821	13.88

TABLE 3: Measured gain, directivity, and radiation efficiency.

CPW-antenna	$f = 2.20$ GHz			$f = 5.80$ GHz		
	$G$ (dB)	$D$ (dB)	$\eta$ (%)	$G$ (dB)	$D$ (dB)	$\eta$ (%)
Bow-tie	—	—	—	2.2	5.4	48
Bow-tie-AMC	3.1	6.5	46	2.4	5.9	45
Bow-tie-AMC metallic plate	2.9	6.9	40	2.1	6.4	37

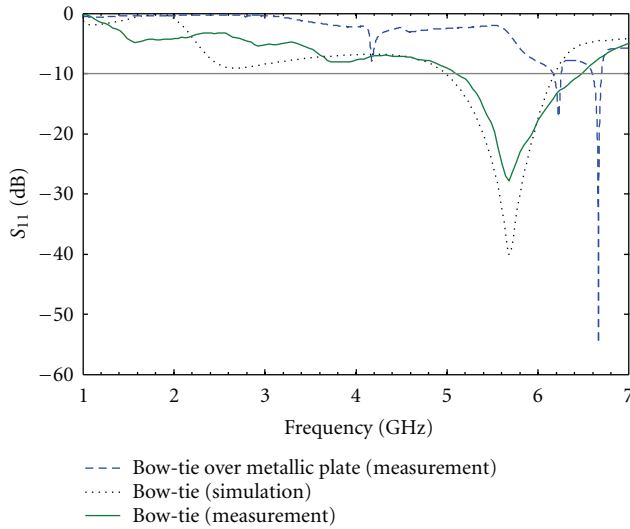


FIGURE 5: Bow-tie antenna's return loss.

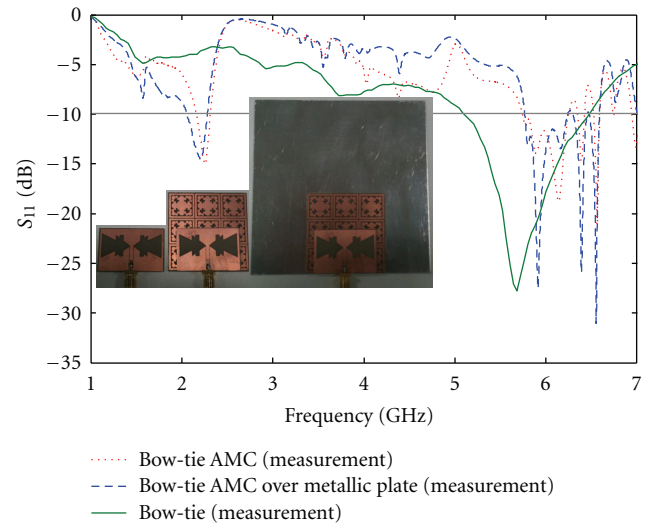


FIGURE 6: Measured input return loss for the prototypes: bow-tie, bow-tie-AMC, and bow-tie-AMC on a metallic plate.

extension for the dielectric substrate or even more likely to manufacturing tolerances.

When the bow-tie antenna is placed on the AMC, the antenna resonance frequency is shifted upwards, as the AMC resonance frequency is higher than the antenna one and in addition, it has higher quality factor. Also a new resonance frequency appears at 2.255 GHz which makes the Bow-tie-AMC combination proper for dual-band applications.

As it could be expected, when the bow-tie antenna alone is placed on a metallic plate the antenna resonance frequency has been shifted out of the 5.8 GHz band leading to its total malfunctioning (see Figure 5). However, from Figure 6 and Table 2, the bow-tie-AMC combination exhibits proper dual-band performance both alone and when placed on a metallic plate, even showing bandwidth enhancement on a metallic plate.

**4.2. Radiation Pattern.** Measured radiation pattern cuts in the  $E$ - and  $H$ -planes of the manufactured prototypes at 2.2 GHz (lower band) and at 5.8 GHz (upper band) are, respectively, plotted in Figures 7 and 8.  $H$ -plane tends to be omnidirectional as it could be expected. The radiation pattern properties of the bow-tie-AMC for RFID application are still preserved even when it is placed on a metallic plate, as the AMC electromagnetically insulates the antenna from the metal and so the bow-tie-AMC currents distribution is not modified. From Figure 8, it can be observed how the AMC reduces the antenna backward radiation between 10 and 20 dB.

The measurement set-up is shown in Figure 9. Table 3 shows the measured Gain, directivity, and radiation efficiency at 2.2 GHz and 5.8 GHz for the manufactured prototypes.

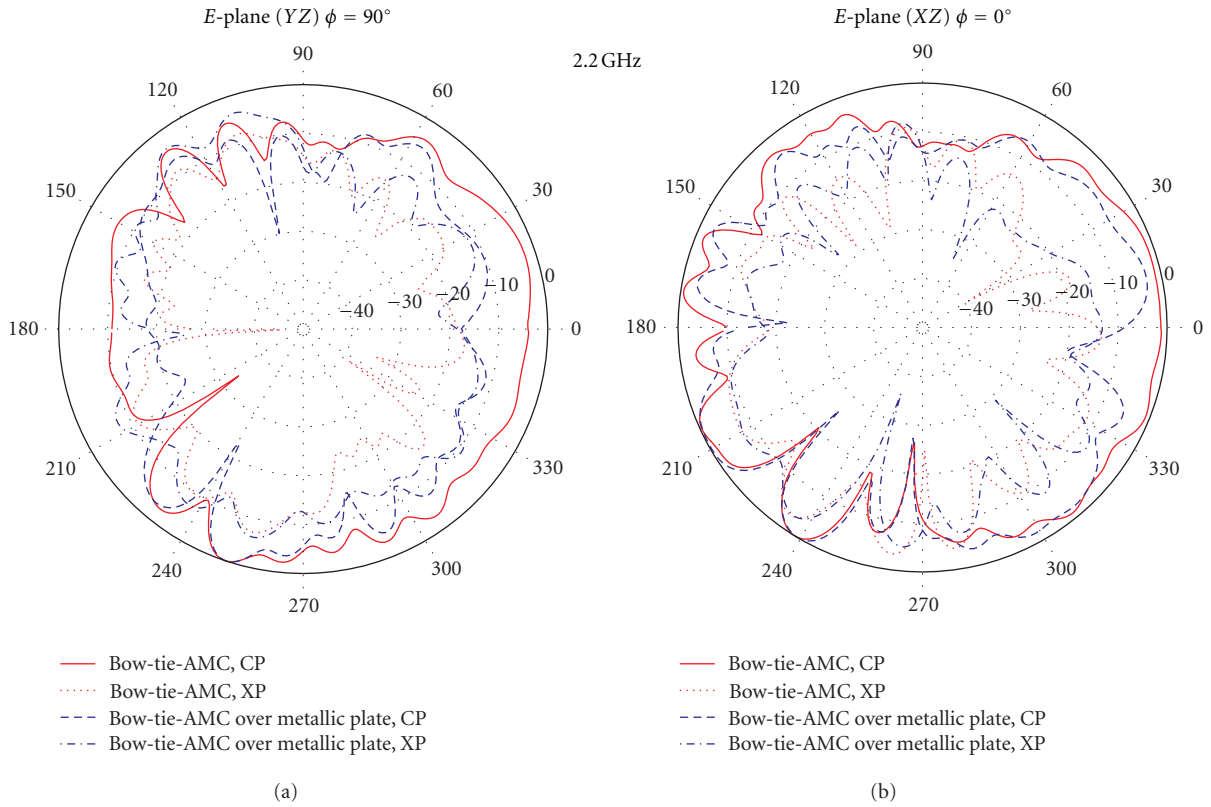


FIGURE 7: Measured radiation pattern (normalized, in dB)  $E$ -plane (a) and  $H$ -plane (b) at 2.2 GHz.

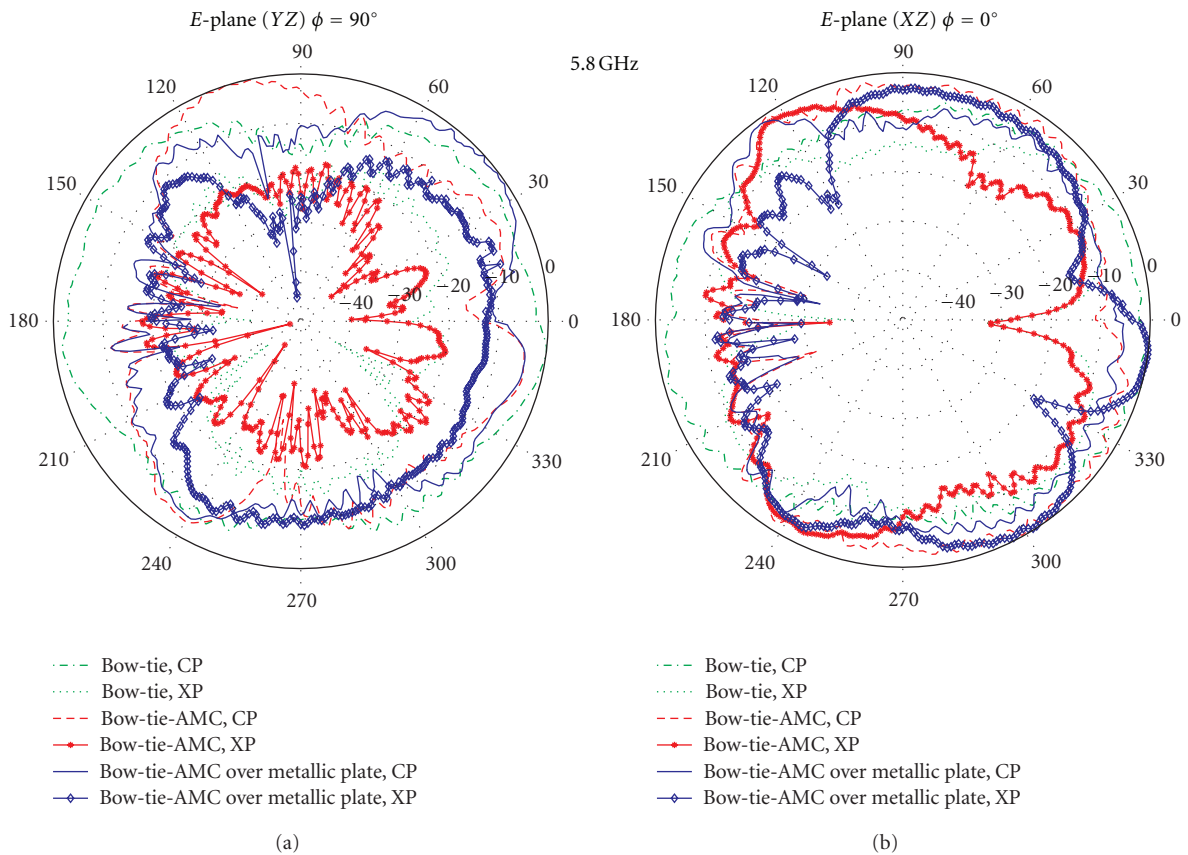


FIGURE 8: Measured radiation pattern (normalized, in dB)  $E$ -plane (a) and  $H$ -plane (b) at 5.8 GHz.

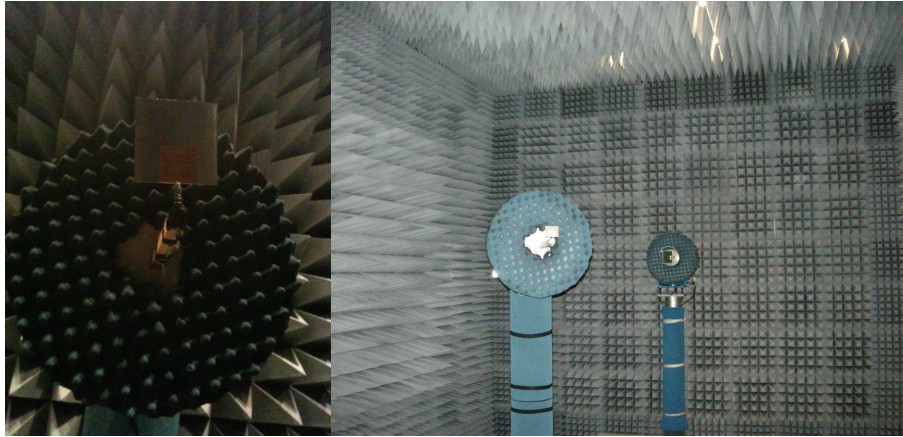


FIGURE 9: Measurement setup in anechoic chamber.

From the obtained results, it can be concluded that the bow-tie-AMC combination makes possible to obtain proper dual-band operation on metallic objects preserving the antenna gain around 3 dB for the lower band and 2.2 dB for the upper band. When the bow-tie-AMC combination is placed on a metallic object, the radiation efficiency is slightly reduced. However, it is remarkable that the measurements on metallic plate have been carried out placing the bow-tie-AMC combination on the edge of the plate, which can be considered the worst case. If the bow-tie-AMC combination were centered on the metallic plate, theoretically, a 6 dB improvement on gain with respect to bow-tie antenna alone should be obtained with slight variation on directivity, leading to radiation efficiency improvement.

## 5. Conclusions

Through a proper bow-tie-AMC combination, consisting of a CPW-fed double bow-tie antenna and a dual AMC, dual-band operation on metallic objects preserving antenna gain and with slight variation on radiation efficiency can be obtained. In addition, the antenna's backward radiation is reduced, which is a key point in wearable antennas and RFID tags usable with people.

A remarkable characteristic of the bow-tie-AMC combination is its compact size: 44.1 mm ( $\lambda_0/3.1$  at 2.2 GHz) and low thickness: 1.524 mm ( $\lambda_0/90$  at 2.2 GHz) its thicker part, which makes it proper for integration in dual-band wireless communication systems. The presented design could be used in RFID applications as tag antennas for both metallic and nonmetallic objects but it could be also used in other dual-band RF systems in the SHF band.

## Acknowledgments

This paper has been supported by the Ministerio de Ciencia e Innovación of Spain/FEDER under Projects TEC2011-24492/TEC (iScat) and CONSOLIDER-INGENIO CSD2008-00068 (TERASENSE), and by the Gobierno del Principado de Asturias (PCTI)/FEDER-FSE under Projects PC10-06 (FLEXANT).

## References

- [1] D. M. Dobkin and S. M. Weigand, "Environmental effects on RFID tag antennas," in *Proceedings of the IEEE MTT-S International Microwave Symposium*, pp. 135–138, Sunnyvale, Calif, USA, June 2005.
- [2] R. H. Clarke, D. Twede, J. R. Tazelaar, and K. K. Boyer, "Radio frequency identification (RFID) performance: the effect of tag orientation and package contents," *Packaging Technology and Science*, vol. 19, no. 1, pp. 45–54, 2006.
- [3] K. V. S. Rao, P. V. Nikitin, and S. F. Lam, "Antenna design for UHF RFID tags: a review and a practical application," *IEEE Transactions on Antennas and Propagation*, vol. 53, no. 12, pp. 3870–3876, 2005.
- [4] P. Raunonen, L. Sydänheimo, L. Ukkonen, M. Keskilammi, and M. Kivikoski, "Folded dipole antenna near metal plate," in *Proceedings of the IEEE International Antennas and Propagation Symposium and USNC/CNC/URSI North American Radio Science Meeting*, pp. 848–851, June 2003.
- [5] L. Ukkonen, L. Sydänheimo, and M. Kivikoski, "Effects of metallic plate size on the performance of microstrip patch-type tag antennas for passive RFID," *IEEE Antennas and Wireless Propagation Letters*, vol. 4, no. 1, pp. 410–413, 2005.
- [6] S. Zhu and R. Langley, "Dual-band wearable textile antenna on an EBG substrate," *IEEE Transactions on Antennas and Propagation*, vol. 57, no. 4, pp. 926–935, 2009.
- [7] M. Mantash, A. C. Tarot, S. Collardey, and K. Mahdjoubi, "Dual-band CPW-fed G-antenna using an EBG structure," in *Proceedings of the 6th Loughborough Antennas and Propagation Conference (LAPC'10)*, pp. 453–456, Loughborough, UK, November 2010.
- [8] P. Salonen, F. Yang, Y. Rahmat-Samii, and M. Kivikoski, "WEBGA—wearable electromagnetic band-gap antenna," in *Proceedings of the IEEE Antennas and Propagation Society International Symposium*, vol. 1, pp. 451–454, Monterrey, Calif, USA, June 2004.
- [9] E. A. Soliman, S. Brebels, P. Delmotte, G. A. E. Vandenbosch, and E. Beyne, "Bow-tie slot antenna fed by CPW," *Electronics Letters*, vol. 35, no. 7, pp. 514–515, 1999.
- [10] Y. L. Chen, C. L. Ruan, and L. Peng, "A novel ultra-wideband bow-tie slot antenna in wireless communication systems," *Progress in Electromagnetics Research Letters*, vol. 1, pp. 101–108, 2008.

- [11] R. C. Hadarig, M. E. de Cos, Y. Álvarez, and F. Las-Heras, "Novel bow-tie—AMC combination for 5.8-GHz RFID tags usable with metallic objects," *IEEE Antennas and Wireless Propagation Letters*, vol. 9, pp. 1217–1220, 2010.
- [12] M. Mantash, A. C. Tarot, S. Collardey, and K. Mahdjoubi, "Dual-band CPW-fed G-antenna using an EBG structure," in *Proceedings of the 6th Loughborough Antennas and Propagation Conference (LAPC'10)*, pp. 453–456, Loughborough, UK, November 2010.
- [13] E. Rajo-Iglesias, L. Inclán-Sánchez, and O. Quevedo-Teruel, "Back radiation reduction in patch antennas using planar soft surfaces," *Progress in Electromagnetics Research Letters*, vol. 6, pp. 123–130, 2009.
- [14] ADS Momentum EM simulation tool, <http://www.agilent.com/find/eesof>.
- [15] F. R. Yang, K. P. Ma, Y. Qian, and T. Itoh, "A uniplanar compact photonic-bandgap (UC-PBG) structure and its applications for microwave circuits," *IEEE Transactions on Microwave Theory and Techniques*, vol. 47, no. 8, pp. 1509–1514, 1999.
- [16] D. Sievenpiper, L. Zhang, R. F. Jimenez Broas, N. G. Alexopoulos, and E. Yablonovitch, "High-impedance electromagnetic surfaces with a forbidden frequency band," *IEEE Transactions on Microwave Theory and Techniques*, vol. 47, no. 11, pp. 2059–2074, 1999.
- [17] A. Monorchio, G. Manara, and L. Lanuzza, "Synthesis of artificial magnetic conductors by using multilayered frequency selective surfaces," *IEEE Antennas and Wireless Propagation Letters*, vol. 1, pp. 196–199, 2002.
- [18] F. Yang and Y. Rahmat-Samii, *Electromagnetic Band-Gap Structures in Antenna Engineering*, The Cambridge RF and Microwave Engineering Series, Cambridge University Press, New York, NY, USA, 2008.
- [19] M. E. de Cos, F. Las-Heras, and M. Franco, "Design of planar artificial magnetic conductor ground plane using frequency-selective surfaces for frequencies below 1 GHz," *IEEE Antennas and Wireless Propagation Letters*, vol. 8, pp. 951–954, 2009.
- [20] M. E. de Cos, Y. Álvarez, and F. Las-Heras, "Planar artificial magnetic conductor: design and characterization setup in the RFID SHF band," *Journal of Electromagnetic Waves and Applications*, vol. 23, no. 11-12, pp. 1467–1478, 2009.
- [21] D. J. Kern, D. H. Werner, A. Monorchio, L. Lanuzza, and M. J. Wilhelm, "The design synthesis of multiband artificial magnetic conductors using high impedance frequency selective surfaces," *IEEE Transactions on Antennas and Propagation*, vol. 53, no. 1 I, pp. 8–17, 2005.
- [22] J. R. Sohn, K. Y. Kim, and H. S. Tae, "Comparative study on various artificial magnetic conductors for low-profile antenna," *Progress in Electromagnetics Research*, vol. 61, pp. 27–37, 2006.
- [23] A. P. Feresidis, G. Goussetis, S. Wang, and J. C. Vardaxoglou, "Artificial magnetic conductor surfaces and their application to low-profile high-gain planar antennas," *IEEE Transactions on Antennas and Propagation*, vol. 53, no. 1 I, pp. 209–215, 2005.
- [24] M. E. de Cos, Y. Álvarez, R. C. Hadarig, and F. Las-Heras, "Novel SHF-band uniplanar artificial magnetic conductor," *IEEE Antennas and Wireless Propagation Letters*, vol. 9, pp. 44–47, 2010.
- [25] Ansoft HFSS, From Ansoft Corporation, Four Station Square Suite 200, Pittsburgh, PA, 15219.
- [26] C. R. Simovski, P. de Maagt, S. A. Tretyakov, M. Paquay, and A. A. Sochava, "Angular stabilisation of resonant frequency of artificial magnetic conductors for TE-incidence," *Electronics Letters*, vol. 40, no. 2, pp. 92–93, 2004.

## Research Article

# A Novel Electrically Small Meandered Line Antenna with a Trident-Shaped Feeding Strip for Wireless Applications

Xueyao Ren, Xing Chen, and Kama Huang

*College of Electronics and Information, SiChuan University, Chengdu 610064, China*

Correspondence should be addressed to Xing Chen, xingch@263.net

Received 6 April 2012; Revised 7 June 2012; Accepted 17 June 2012

Academic Editor: Leena Ukkonen

Copyright © 2012 Xueyao Ren et al. This is an open access article distributed under the Creative Commons Attribution License, which permits unrestricted use, distribution, and reproduction in any medium, provided the original work is properly cited.

A novel electrically small antenna (ESA) which based on the meandered line structure is designed, fabricated, and measured. The proposed antenna whose total size is  $13.50 \text{ mm} \times 13.51 \text{ mm} \times 0.8 \text{ mm}$  is designed to cater for the ISM (industrial, scientific, and medical) band of 2.45 GHz with a  $S_{11} < -10 \text{ dB}$  bandwidth of 3.9%. By introducing a trident-shaped feeding strip and inserting 4 pairs of triangular slot stubs at the central feed line, the resonant frequency of the antenna drops to 2.45 GHz from 2.50 GHz and the impedance matching is improved significantly. The dimension parameters of this antenna are optimized to achieve wide impedance bandwidth, reasonably high gain, as well as omnidirectional radiation pattern.

## 1. Introduction

Recently, wireless communication has become more and more widespread. As compact wireless communication systems become a greater focus in our lives, the demand for small-size and high-performance antennas escalates. Therefore, antenna miniaturization has received significant attention in the latest years.

For an antenna which is categorized to electrically small, it should fulfill the definition:  $ka < 0.5$ , where  $k$  is defined as the free space wave number and  $a$  the radius of the sphere inclosing the maximum dimensions of the antenna [1, 2]. The size reduction of antennas will result in the performance degradation such as narrow bandwidth, high voltage standing wave ratio (VSWR), low gain, among others. Accordingly, the key of designing an electrically small antenna is always an art of compromise among size, bandwidth, and gain.

Numerous designs of electrically small antenna have been presented in the recent literatures, such as the disk-loaded monopole antenna [3], inductively coupled feed antenna [4], arbitrarily shaped wire antennas designed by genetic algorithms (GA) [5, 6], folded monopoles and meandered dipoles [7, 8], resistively or reactively lumped components loading antennas [9, 10], metamaterial-based electrically small antennas [11, 12], superconducting electrically small

antennas [13, 14], among others. It is noted that most of their structures are complicated, which increases manufacturing difficulty and cost. Some of them are not planar structures that are suitable for connected with monolithic microwave integrated circuit (MMIC). Some of them must work together with external inductors or capacitors, which cause extraohmic losses that could be critical for some applications. Some of them are born with narrow bandwidth which is less than 1% because the permeability or permittivity of the metamaterial could be zero only in a particular frequency. Others might meet the strict definition of ESA but only under rigorous conditions, for example, superconductivity.

The coplanar waveguide- (CPW-) fed antennas have many attractive features, such as low radiation loss, less dissipation, easy fabrication, and integration with MMIC without any need of via holes as used in microstrip technology.

In this paper, a novel electrically small antenna with a trident-shaped feeding strip is proposed. The trident-shaped feeding strip is introduced to reduce the electrical size of the antenna. At the same time, 4 pairs of triangular slot stubs are used to improve the performance in terms of bandwidth. Section 2 describes the configuration of the proposed antenna. Section 3 includes numerical results simulated by the software Ansoft High Frequency Structure Simulator (HFSS) [15] which is based on 3D full-wave finite-element method (FEM). To examine the antenna

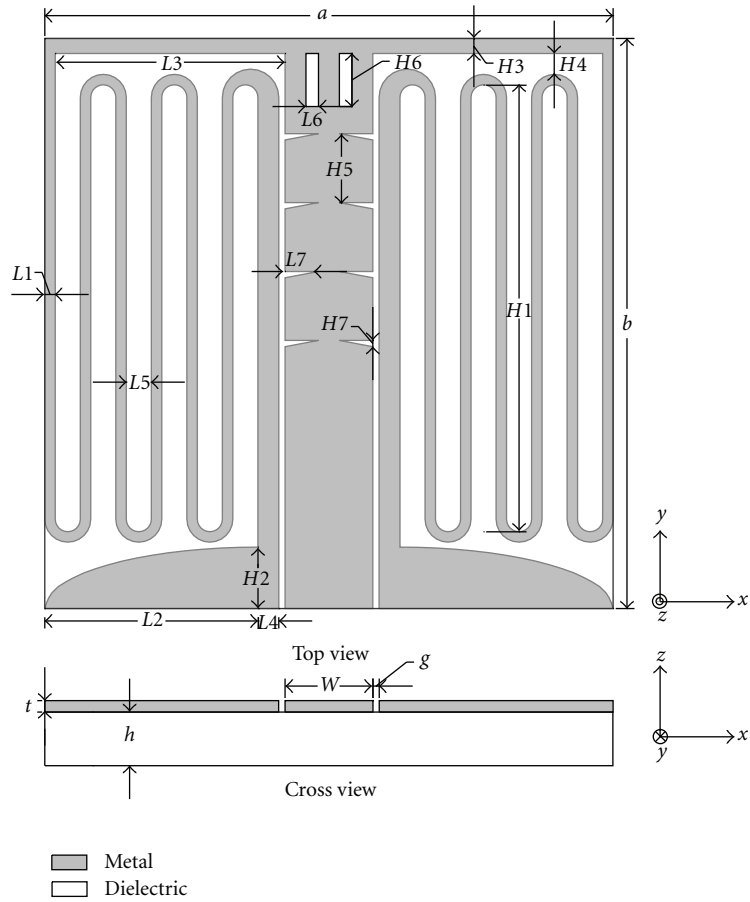


FIGURE 1: Geometry configuration of proposed antenna.

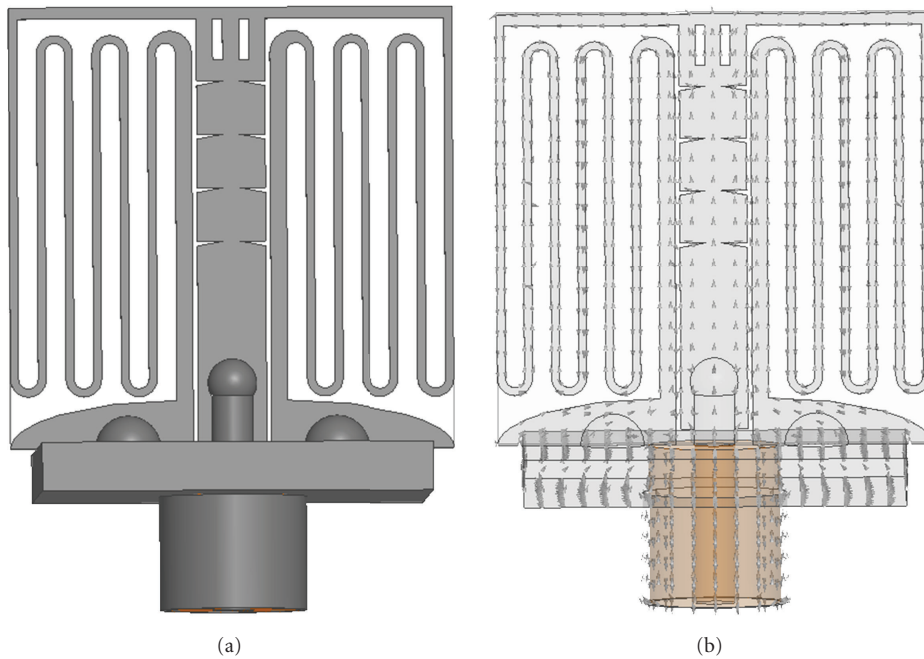


FIGURE 2: The simulation model of the proposed antenna and the surface current distribution.

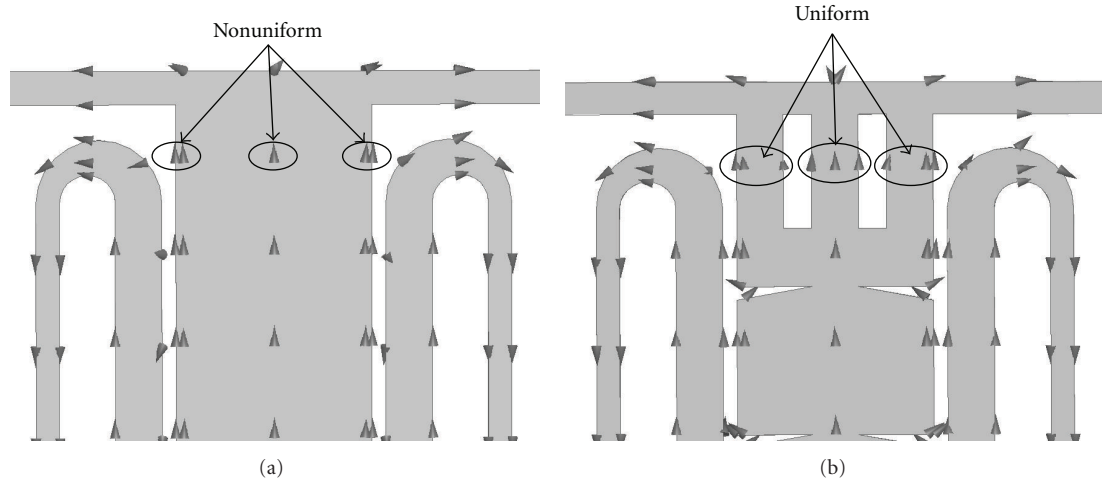


FIGURE 3: (a) A common CPW feeding line (b) A CPW feeding line with a trident-shaped feeding strip and triangular slot stubs.

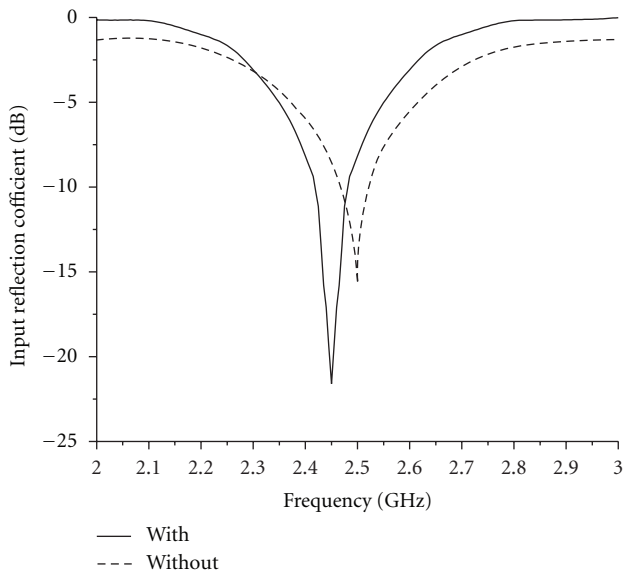


FIGURE 4: Input reflection coefficient comparison of the antenna with or without a trident-shaped feeding strip and 4 pairs of triangular slot stubs.

performance, experimental results are also involved and discussed.

## 2. Antenna Configuration

The geometry configuration of the proposed CPW-fed antenna is shown in Figure 1. The antenna is based on nongrounded coplanar waveguide which has a single-layer metallic structure (thickness  $t = 0.018$  mm) and etched on a side of an FR-4 substrate. The selected substrate material is Rogers RO4003C [16] with a dielectric constant  $\epsilon_r = 3.38$  and thickness  $h = 0.8$  mm. The overall dimension of the proposed antenna is  $13.50$  mm  $\times$   $13.51$  mm. A  $50 \Omega$  CPW central transmission line of strip with width  $W = 2$  mm and gap  $g = 0.15$  mm is used for feeding the antenna.

This antenna is based on two meandered parallel resonant arms whose lengths are  $H1$  and widths are  $L1$  to further reduce the antenna dimensions because this meandering leads to an extended current path for a fixed length, so that the antenna seems electrically larger [17]. The latitudinal distance between two meandered arms is  $L5$ . There is a strip whose length is  $L3$  and width is  $H3$ , connecting the central transmission line to the two meandered arms. One-quarter of elliptical ground is introduced to improve the impedance bandwidth. Lengths of the semimajor axis and the semiminor axis of this elliptical ground are  $L2$  and  $H2$  respectively. A tapered parallel arm with length  $H1$ , width  $L4$  is used to realize impedance transformation between ground and meandered parallel resonant arm. By inserting a pair of longitude direction's symmetrical slots whose lengths are  $H6$  and widths are  $L6$ , a trident-shaped feeding strip is achieved. The impedance matching is improved significantly by using this trident-shaped feeding strip working with 4 pairs of triangular slot stubs whose lengths are  $L7$  and widths are  $H7$ . The longitudinal distance between each pair of triangular slot stubs is  $H5$ . Finally, the other dimensions of the proposed antenna are optimized as follow:  $a = 13.50$  mm,  $b = 13.51$  mm,  $L1 = 0.25$  mm,  $H1 = 10.70$  mm,  $L2 = 5.10$  mm,  $H2 = 1.45$  mm,  $L3 = 5.50$  mm,  $H3 = 0.36$  mm,  $L4 = 0.50$  mm,  $H4 = 0.50$  mm,  $L5 = 0.60$  mm,  $H5 = 1.65$  mm,  $L6 = 0.25$  mm,  $H6 = 1.27$  mm,  $L7 = 0.75$  mm,  $H7 = 0.15$  mm.

## 3. Antenna Design

The whole antenna mounting structure of the simulation model, including its driving connector and the corresponding surface current vector distribution are shown in Figure 2. Three metal balls were used to simulate the solder joints.

A key idea of the proposed novel feeding structure can be most conveniently explained by consideration of an equivalent current path on the metallic conductor which can be seen in Figure 3. It is seen from Figure 3(a) that most of the current focuses on both sides of the central feeding

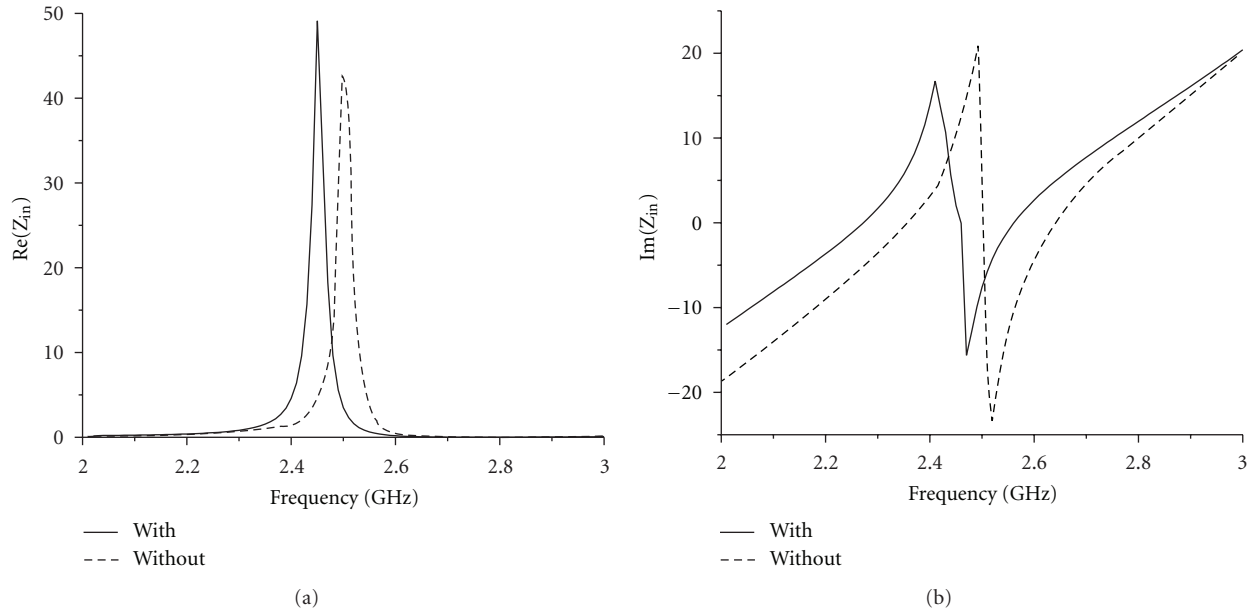


FIGURE 5: Input impedance comparison of the antenna with or without a trident-shaped feeding strip and 4 pairs of triangular slot stubs.

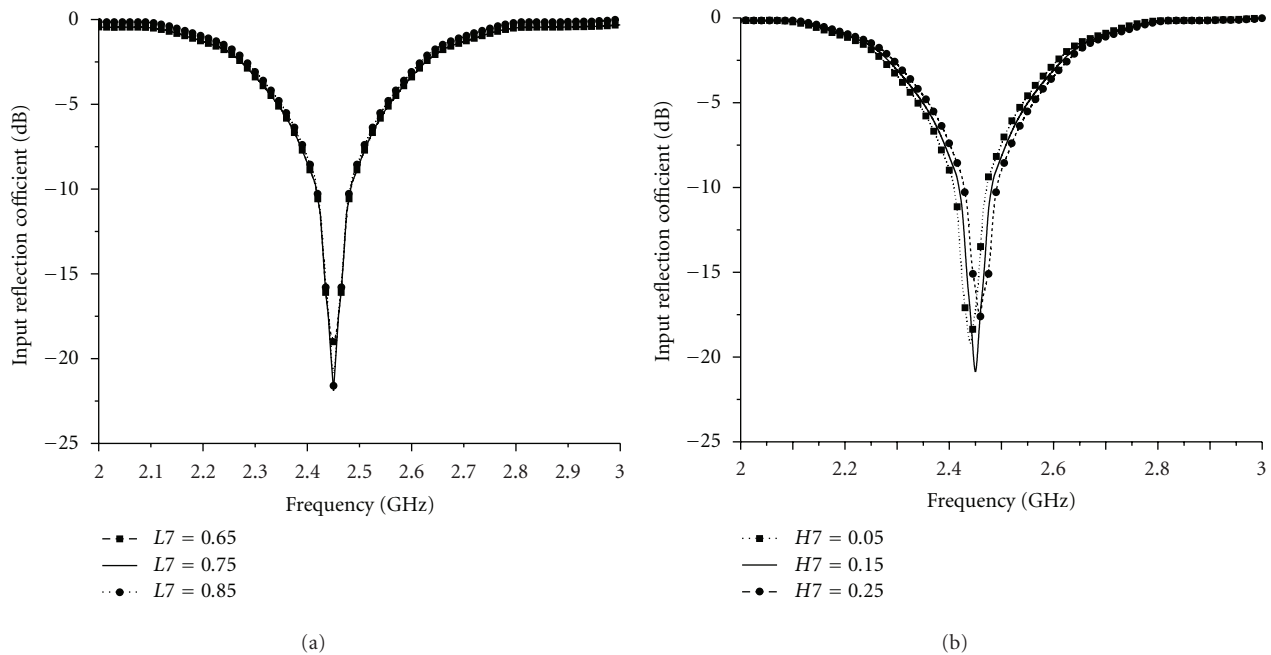


FIGURE 6: The input reflection coefficient changes with the length  $L7$  and width  $H7$ .

line because the radiation is along the slot of CPW structure. The current distributions between the middle and both sides are nonuniform. It is also seen from Figure 3(b) that, the middle current distribution becomes more uniform due to a trident-shaped feeding structure which is used to shunt the current that focus on both sides of the central feeding line, and increase current that flows to two meandered arms from middle. As a result, the equivalent path of current distribution becomes slightly longer for a fixed dimension. So the resonant frequency of the antenna from 2.50 GHz drops to 2.45 GHz.

However, this structure changes the antenna to unbalance. By adding 4 pairs of triangular slot stubs symmetrically on each side of the central CPW feeding line, the impedance matching condition is improved observably, which is shown in Figure 4.

Figure 4 illustrates the computed input reflection coefficient of the common CPW feeding antenna (dash line) in comparison with that of the antenna having the novel feeding structure (solid line). It observed that  $S_{11} < -10$  dB bandwidth of the antenna with proposed feeding structure amounts to 65 MHz from 2.415 GHz to 2.480 GHz with

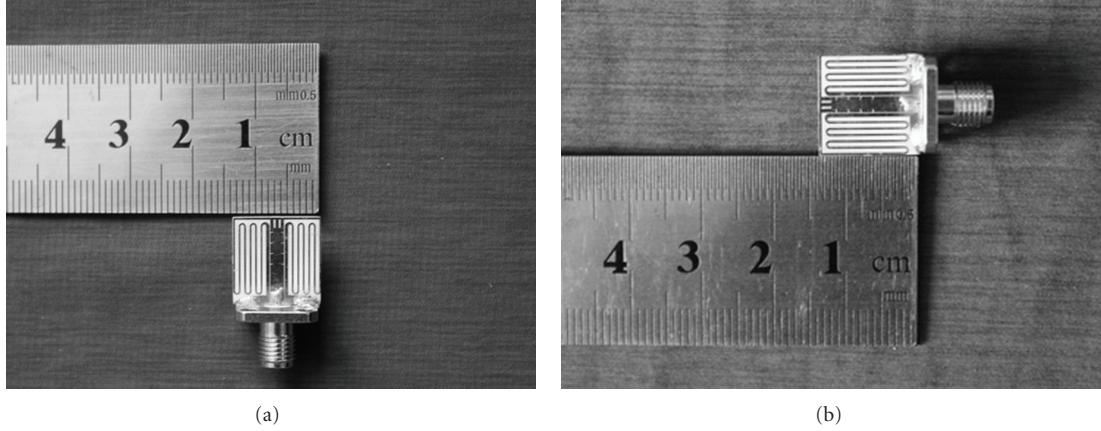


FIGURE 7: The prototype of the proposed antenna (a) top view (b) side view.

the center frequency at 2.45 GHz, while the corresponding bandwidth of the common CPW antenna is 45 MHz from 2.470 GHz to 2.515 GHz with the center frequency at 2.50 GHz. Thus, the  $S_{11} < -10$  dB bandwidth of novel antenna is wider by 44% than the common one. At the same time, the electrical size of the antenna  $ka$  drops to 0.49 from 0.50. As proven above, the bandwidth enhancement and impedance matching condition have been achieved exclusively owing to the trident-shaped feeding strip and the triangular slot stubs, the changes of input impedance with or without the trident-shaped feeding strip and the triangular slot stubs are shown in Figure 5. The changes of input reflection coefficient with the length  $L7$  and width  $H7$  of the slot-stubs can be seen in Figure 6. One can observe that the length  $L7$  has little effect on input reflection coefficient, while the width  $H7$  has a major influence on it.

#### 4. Results and Discussion

To validate the theoretical design, a prototype of the antenna has been fabricated which shown in Figure 7. The input reflection coefficient of the fabricated electrically small antenna has been measured by an Agilent N5230A Network Analyzer.

Measured input reflection coefficient and the computed one by simulation are shown in Figure 8.

The designed resonant frequency of the proposed antenna is 2.45 GHz, the measured one, shown in Figure 8, is observed at 2.46 GHz (0.4% error). It also can be seen that the antenna has a good match at 2.46 GHz with an input reflection coefficient of  $-30.80$  dB. The measured  $S_{11} < -10$  dB bandwidth is 95 MHz from 2.410 GHz to 2.505 GHz, corresponding to 3.9% of the center frequency versus the simulated one 2.7% from 2.415 GHz to 2.480 GHz. These errors may be caused by the error of dielectric constant and manufacturing tolerances.

The dimensions of the proposed antenna are  $13.50 \text{ mm} \times 13.51 \text{ mm} \times 0.8 \text{ mm}$ , namely,  $0.11\lambda_0 \times 0.11\lambda_0 \times 0.0065\lambda_0$ ,  $\lambda_0$  is the wavelength in free space at the center frequency. For this antenna, the electrical size of the antenna  $ka = 0.49$ , so it can be categorized to electrically small antenna strictly.

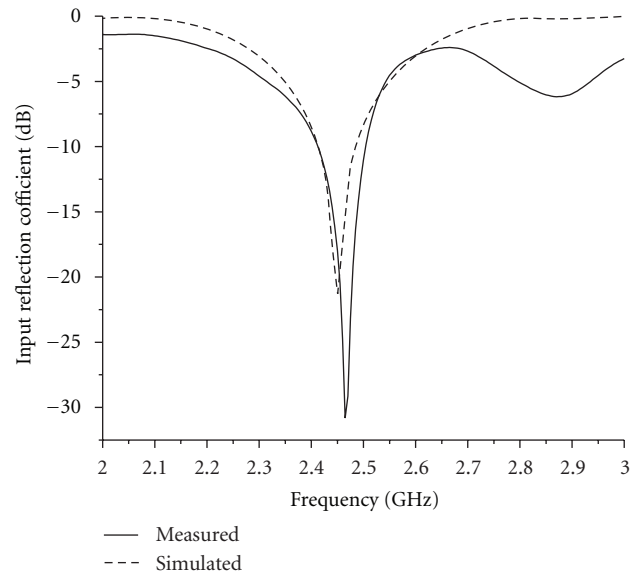


FIGURE 8: The simulated and measured input reflection coefficient.

As we known, when the electrical size of an antenna is small to a certain degree ( $ka < 0.5$ ), it is difficult to make it smaller and maintain the same performance as well.

Radiation patterns of the proposed antenna are measured in a standard anechoic chamber. Simulated and measured radiation patterns in H-plane and E-plane in the working bandwidth are shown in Figure 9. They are also roughly the same, and show a good omnidirectional radiation pattern is realized. The simulated gain as a function of frequency from 2.4 GHz to 2.5 GHz is shown in Figure 10.

#### 5. Conclusion

A novel electrically small antenna with a refined configuration of the trident-shaped feeding strip and the triangular slot stubs has been proposed in this paper. It has a simple structure based on a CPW feeding line and allows the use of low-cost and accurate planar print techniques. Precise prototyping and accurate measurement guarantee the veracity of

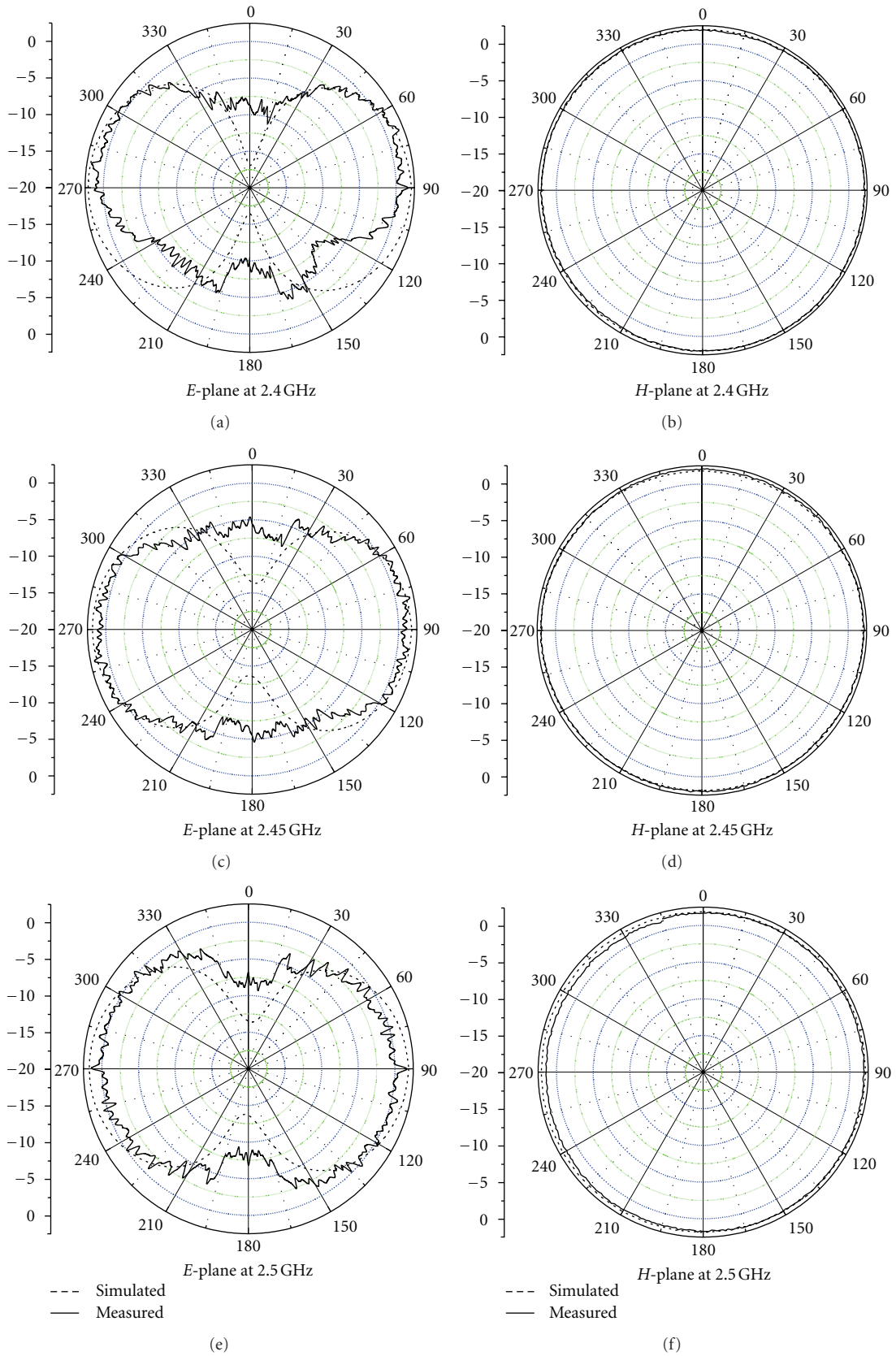


FIGURE 9: The radiation pattern of the proposed antenna in the working bandwidth.

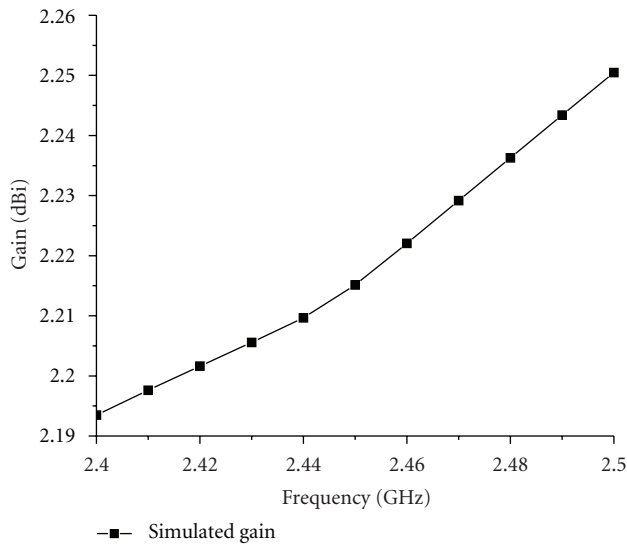


FIGURE 10: The simulated gain as a function of frequency from 2.4 GHz to 2.5 GHz.

the results. It provides a  $S_{11} < -10$  dB bandwidth about 3.9% (from 2.410 GHz to 2.505 GHz), and an input reflection coefficient of  $-30.80$  dB at the working frequency 2.46 GHz. The computed gain is up to 2.2 dBi at 2.45 GHz. Those properties make this antenna to be a probable candidate for wireless communication applications.

## References

- [1] H. A. Wheeler, "Fundamental limitations of small antennas," *Proceedings of the IRE*, vol. 35, no. 12, pp. 1479–1484, 1947.
- [2] H. R. Stuart and A. Pidwerbetsky, "Electrically small antenna elements using negative permittivity resonators," *IEEE Transactions on Antennas and Propagation*, vol. 54, no. 6, pp. 1644–1653, 2006.
- [3] H. D. Foltz, J. S. McLean, and G. Crook, "Disk-loaded monopoles with parallel strip elements," *IEEE Transactions on Antennas and Propagation*, vol. 46, no. 12, pp. 1894–1896, 1998.
- [4] H. Choo and H. Ling, "Design of electrically small planar antennas using inductively coupled feed," *Electronics Letters*, vol. 39, no. 22, pp. 1563–1565, 2003.
- [5] E. E. Altshuler, "Electrically small self-resonant wire antennas optimized using a genetic algorithm," *IEEE Transactions on Antennas and Propagation*, vol. 50, no. 3, pp. 297–300, 2002.
- [6] H. Choo, R. Rogers, and H. Ling, "Design of electrically small wire antennas using genetic algorithm taking into consideration of bandwidth and efficiency," in *Proceedings of the IEEE Antennas and Propagation Society International Symposium*, pp. 330–333, June 2002.
- [7] M. S. Sharawi, Y. S. Faouri, and S. S. Iqbal, "Design and fabrication of a dual electrically small MIMO antenna system for 4G terminals," in *Proceedings of the German Microwave Conference (GeMiC'11)*, pp. 1–4, March 2011.
- [8] K. M. Chan, E. Lee, P. Gardner, and P. S. Hall, "A differentially fed electrically small antenna," in *Proceedings of the IEEE Antennas and Propagation Society International Symposium (AP-S'07)*, pp. 2447–2450, Honolulu, Hawaii, USA, June 2007.
- [9] P. Jin and R. W. Ziolkowski, "Multiband extensions of the electrically small, near-field resonant parasitic Z antenna," *IET Microwaves, Antennas and Propagation*, vol. 4, no. 8, pp. 1016–1025, 2010.
- [10] M. C. Scardelletti, G. E. Ponchak, S. Merritt, J. S. Minor, and C. A. Zorman, "Electrically small folded slot antenna utilizing capacitive loaded slot lines," in *Proceedings of the IEEE Radio and Wireless Symposium (RWS'08)*, pp. 731–734, Orlando, Fla, USA, January 2008.
- [11] F. Qureshi, M. A. Antoniadis, and G. V. Eleftheriades, "A compact and low-profile metamaterial ring antenna with vertical polarization," *IEEE Antennas and Wireless Propagation Letters*, vol. 4, no. 1, pp. 333–336, 2005.
- [12] Y. J. Kim, J. K. Kim, J. H. Kim, H. Y. Kim, and H. M. Lee, "Negative permeability metamaterial structure based electrically small loop antenna," in *Proceedings of the 10th International Conference on Advanced Communication Technology (ICACT'08)*, pp. 769–773, Gangwon-Do, Korea, February 2008.
- [13] P. S. Excell and N. McN Alford, "Superconducting electrically-small dipole antenna," in *Proceedings of the 7th International Conference on Antennas and Propagation (ICAP'91)*, pp. 446–447, April 1991.
- [14] Y. Tsutsumi, H. Kanaya, and K. Yoshida, "Design and performance of an electrically small slot loop antenna with a miniaturized superconducting matching circuit," *IEEE Transactions on Applied Superconductivity*, vol. 15, no. 2, pp. 1020–1023, 2005.
- [15] *An Introduction To HFSS, V12. 1*, 1st edition, 2010.
- [16] RO4000 laminates-Data sheet, Rogers corporation.
- [17] A. K. Skrivervik, J. F. Zürcher, O. Staub, and J. R. Mosig, "PCS antenna design: the challenge of miniaturization," *IEEE Antennas and Propagation Magazine*, vol. 43, no. 4, pp. 12–27, 2001.

## Research Article

# Resonant Frequency Calculation and Optimal Design of Peano Fractal Antenna for Partial Discharge Detection

Jian Li, Changkui Cheng, Lianwei Bao, and Tianyan Jiang

State Key Laboratory of Power Transmission Equipment & System and New Technology, Chongqing University, Chongqing 400044, China

Correspondence should be addressed to Jian Li, lijian@cqu.edu.cn

Received 23 January 2012; Revised 3 May 2012; Accepted 17 May 2012

Academic Editor: Harish Rajagopalan

Copyright © 2012 Jian Li et al. This is an open access article distributed under the Creative Commons Attribution License, which permits unrestricted use, distribution, and reproduction in any medium, provided the original work is properly cited.

Ultra-high-frequency (UHF) approaches have caught increasing attention recently and have been considered as a promising technology for online monitoring partial discharge (PD) signals. This paper presents a Peano fractal antenna for UHF PD online monitoring of transformer with small size and multiband. The approximate formula for calculating the first resonant frequency of the Peano fractal antenna is presented. The results show that the first resonant frequency of the Peano fractal antenna is smaller than the Hilbert fractal antenna when the outer dimensions are equivalent approximately. The optimal geometric parameters of the antenna were obtained through simulation. Actual PD experiments had been carried out for two typically artificial insulation defect models, while the proposed antenna and the existing Hilbert antenna were both used for the PD measurement. The experimental results show that Peano fractal antenna is qualified for PD online UHF monitoring and a little more suitable than the Hilbert fractal antenna for pattern recognition by analyzing the waveforms of detected UHF PD signals.

## 1. Introduction

Partial discharge (PD) online monitoring is an effective approach to inspect insulation defects and identify potential faults in power transformer [1]. Hence, it is important for monitoring PD signals online for power transformer. Compared with traditional detection methods, the ultra-high-frequency (UHF) technology has advantages such as high sensitivity and strong anti-interference, which make it more suitable for PD online monitoring [2]. By receiving the UHF electromagnetic waves of PD occurred in a power transformer, the UHF detection technology can measure the PD magnitudes and locate the PD source [3–7].

Antenna is the core component of an UHF PD online monitoring system. The performance of antenna will affect the extraction and postprocessing of PD signals. Currently, there are many types of UHF antennas used in PD detection for electrical plants. Literatures [8, 9] presented a two-wire Archimedean planar spiral antenna and its application in PD detection. A dipole antenna model and its waveform characteristics were introduced in [10], and a small loop

antenna was given in [11] to detect PD signals in transformer insulation oil. In addition to transformers, UHF antennas have been used for PD detection for other high voltage apparatuses. The horn antenna, biconical log-periodic antenna, loop antenna, and dipole antenna were used for PD detection for gas insulated switchgear (GIS) [12, 13].

Two criteria have to be considered for design of UHF antennas detecting PD in transformer [14]. On the one hand, the resonant frequencies of UHF PD antennas are required to fall into a lower range between 300 MHz and 1000 MHz with a wide bandwidth [5]. The lower first resonant frequency is important for the fractal antenna used in detecting UHF PD signals. Publication [15] presented the fundamental frequencies of Hilbert fractal antenna, while the calculated formula was presented in publication [16]. On the other hand, for the purpose of not affecting the safe operation of transformers and the convenience of installation, an antenna as small as possible is needed. The fractal antenna showed superior in these two respects, and publication [17] presented a compact Hilbert fractal antenna for UHF PD detection for power transformer. Literature [18] presented that the Peano fractal

antenna resonated at a lower fundamental frequency than the same order Hilbert antenna. It is expected that the outer dimension of Peano antenna is smaller than Hilbert antenna when their performances are both good.

This paper presents an approximate resonant frequency calculation formula and optimal design of UHF Peano fractal antenna for online monitoring PD of power transformers. The operation principle and the approximate resonant frequency calculation formula of the antenna are proposed. Besides, the antenna optimal design procedure is also addressed in the paper. The performances of the optimal antenna are given and discussed through simulation. To validate its performance, actual experiments were carried out on the proposed antenna and the existing Hilbert antenna for PD measurements of two typically artificial oil-paper defects in laboratory. The compared results show that the Peano fractal antenna is a little more suitable than the Hilbert fractal antenna for PD online UHF monitoring. The paper is organized as follows: Section 2 proposes the approximate resonant frequency calculation formula of the Peano fractal antenna. The actual optimal design procedure of antenna is given in Section 3. Section 4 presents the experiments and the experimental results. The conclusions are given in Section 5.

## 2. Resonant Frequency of Peano Fractal Antenna

Design of Peano fractal antennas is based on Peano fractal curves. Figure 1 shows a set of Peano fractal curves from the first to the third order. A Peano fractal curve is a continuous curve with a characteristic of strict self-similarity [19]. It is clear that the length of a Peano fractal curve is greater if the order of the curve is higher. If a Peano fractal curve has an infinite order, the curve will fill out all the space of the two-dimensional plane. For a Peano antenna with a side dimension  $L$  and an order of  $n$ , the length of each line segment  $d$  (shown in Figure 1) and the sum of all the line segments  $S$  are given by:

$$d = \frac{L}{3^n - 1}; \quad S = (3^{2n} - 1)d = (3^n + 1)L. \quad (1)$$

The resonant frequency calculated formula of the meander line antennas can be referred to [20]. Peano fractal wires are divided into parallel wire section, short circuit termination, and additional wire section, which are illustrated in Figure 2.

In a Peano fractal geometry of order  $n$ , there are  $m$  short circuited parallel wire sections, which can be expressed as follows:

$$m = \frac{3^{2n} - 1}{4}. \quad (2)$$

The length of the line segments  $s$  except the parallel wire sections is expressed as follows:

$$s = \frac{3^{2n} - 1}{2}d. \quad (3)$$

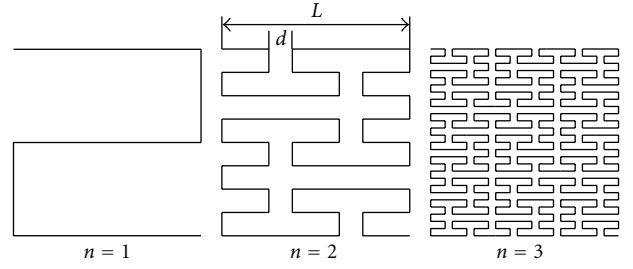


FIGURE 1: Peano curves from the first to the third order.

The characteristic impedance of a parallel wire transmission line consisting of wires with diameter  $b$ , spacing  $d$  is expressed as follows:

$$Z_0 = \frac{Z_c}{\pi} \log \frac{2d}{b}, \quad (4)$$

where  $Z_c$  is the intrinsic impedance of free space,  $Z_c = 120 \pi \Omega$ .  $Z_0$  can be used to calculate the input impedance at the ends of the line, which is purely inductive;

$$L_{in,s} = \frac{Z_0}{\omega} \tan \beta d, \quad (5)$$

where  $\omega$  is angular frequency, and  $\omega = 2\pi f$ ,  $\beta$  is phase constant, and  $\beta = 2\pi/\lambda$  and  $\lambda$  is the wavelength of the electromagnetic wave. The total input impedance of parallel wire transmission line of a Peano fractal antenna with  $n$  order can be expressed by

$$L_{in} = m \cdot \frac{Z_c}{\pi \omega} \cdot \log \frac{2d}{b} \cdot \tan \beta d. \quad (6)$$

When  $d$  is sufficiently small compared to the wavelength of the electromagnetic wave,  $\tan(\beta d)$  can be expressed by the following Taylor formula [19]:

$$\tan \beta d = \beta d + \frac{1}{3}(\beta d)^3 + \frac{1}{5}(\beta d)^5 + \dots \quad (7)$$

The self-inductance due to a straight line of lengths  $s$  as defined in (3) is

$$L_s = \frac{\mu_0}{2\pi} \cdot s \cdot \left( \log \frac{4s}{b} - 1 \right). \quad (8)$$

The total inductance of a Peano antenna with  $n$  orders is expressed as follows:

$$L_T = m \cdot \frac{Z_c}{\pi \omega} \cdot \log \frac{2d}{b} \cdot \tan \beta d + \frac{\mu_0}{2\pi} \cdot s \cdot \left( \log \frac{4s}{b} - 1 \right). \quad (9)$$

The total inductance of fractal antenna equals to inductance of the half-wave dipole antenna approximately referenced to publication [15]. And the inductance of the half-wave dipole antenna is expressed by

$$L_d = \frac{\mu_0}{\pi} \cdot \frac{\lambda}{4} \cdot \left( \log \frac{2\lambda}{b} - 1 \right), \quad (10)$$

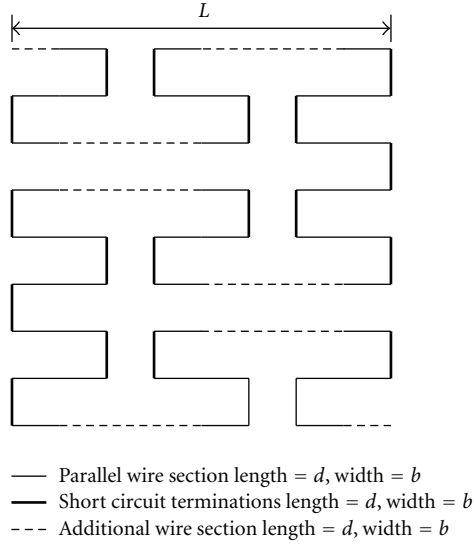


FIGURE 2: Composition of Peano fractal wires for calculating the resonant frequency.

where  $\mu_0$  is the permeability of vacuum and equals to  $4\pi \times 10^{-7} \text{ Hm}^{-1}$ , for half-wave dipole antenna,  $\lambda = 2L$ . The resonant frequencies of the Peano fractal antenna with  $n$  order are calculated by the equation  $L_T \approx L_d$ . If the equivalent arm length of dipole antenna is changed, the multi-resonant frequencies can be obtained. All resonant frequencies of the Peano fractal antenna with  $n$  orders are obtained as follows:

$$\begin{aligned} m \cdot \frac{Z_c}{\pi\omega} \cdot \log \frac{2d}{b} \tan \beta d + \frac{\mu_0}{2\pi} \cdot s \cdot \left( \log \frac{4s}{b} - 1 \right) \\ = \frac{\mu_0}{\pi} \cdot \frac{k\lambda}{4} \cdot \left( \log \frac{2k\lambda}{b} - 1 \right) \end{aligned} \quad (11)$$

$$f_r = \frac{c}{\lambda}$$

where  $c$  is velocity of light,  $c = 3 \times 10^8 \text{ m/s}$ ,  $k$  is an odd number.

This paper focuses on the calculation for the first resonant frequency of the Peano fractal antenna. With (11), the first resonant frequency of the Peano fractal antenna with  $n$  order can be calculated by (12) as follows:

$$\begin{aligned} m \cdot \frac{Z_c}{\pi\omega} \cdot \log \frac{2d}{b} \cdot \beta d + \frac{\mu_0}{\pi} \cdot s \cdot \frac{\mu_0}{2\pi} \cdot s \cdot \left( \log \frac{4s}{b} - 1 \right) \\ = \frac{\mu_0}{\pi} \cdot \frac{\lambda}{4} \cdot \left( \log \frac{2\lambda}{b} - 1 \right) \end{aligned} \quad (12)$$

$$f_r = \frac{c}{\lambda}$$

It is clear that the first resonant frequency of the fractal antenna is mainly related to the order and side dimension of the antenna and width of conductor. Table 1 shows the first resonant frequencies of the Peano and Hilbert fractal antennas with different parameters calculated by (12), respectively.

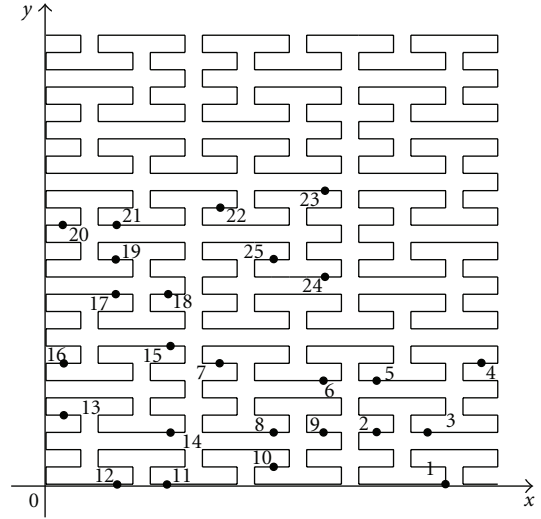


FIGURE 3: Feed points selected of Peano fractal antenna for simulation.

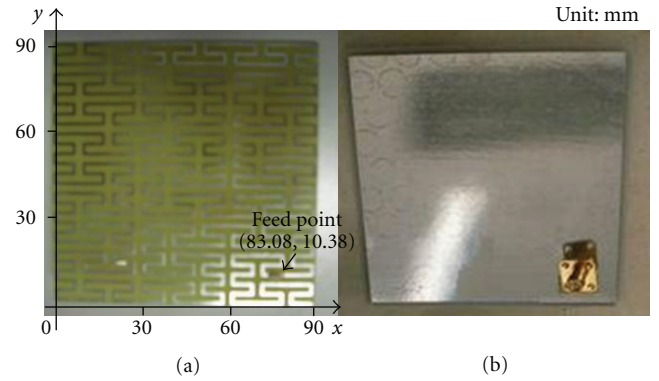


FIGURE 4: The third Peano fractal antenna: (a) front face of antenna, (b) back of antenna.

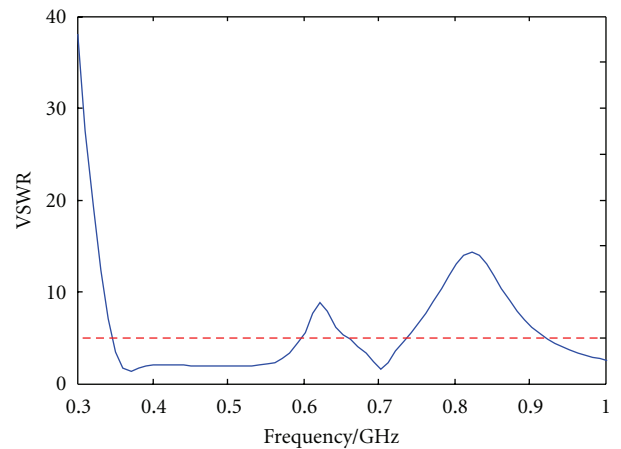


FIGURE 5: VSWR curve of the Peano fractal antenna.

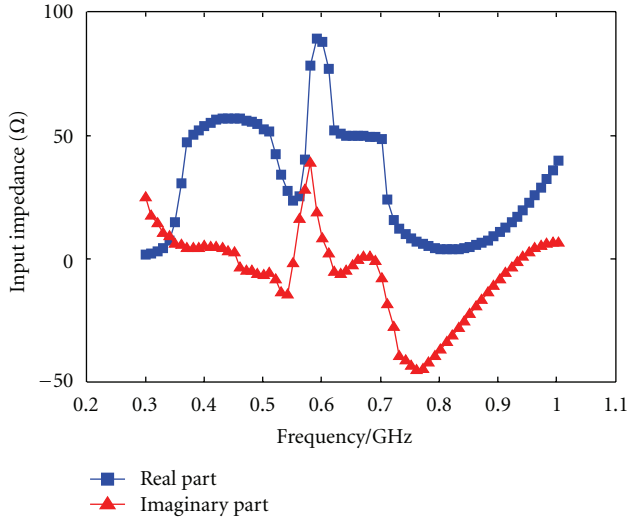


FIGURE 6: Input impedance of the Peano fractal antenna.

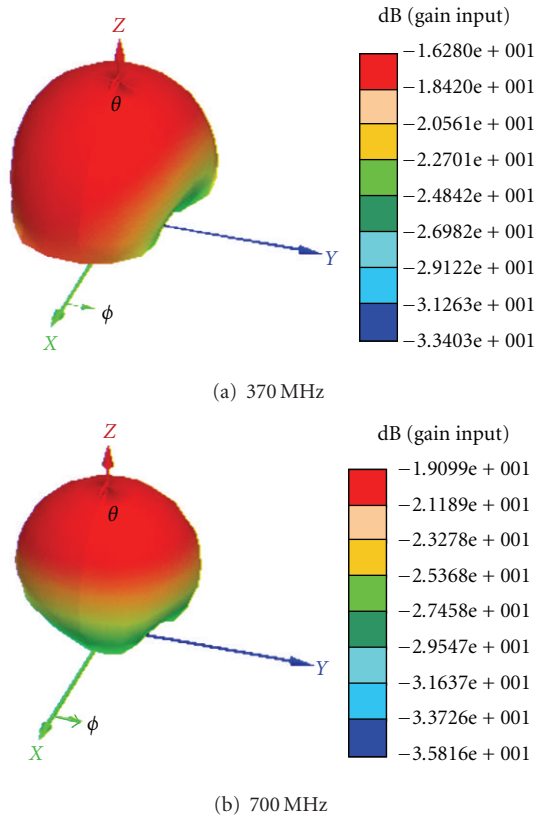
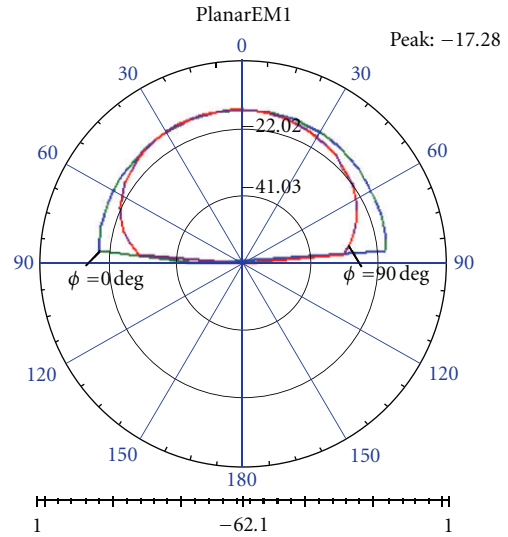
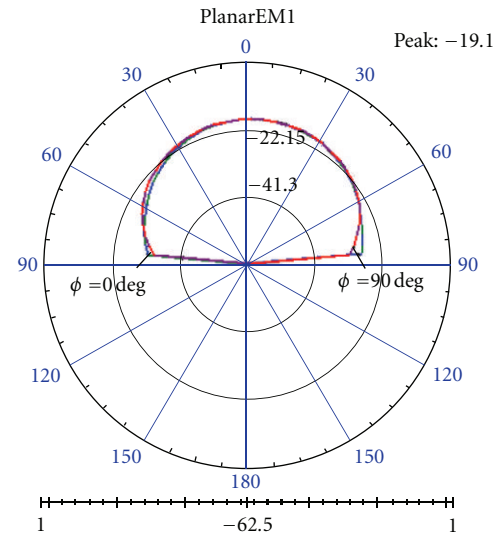


FIGURE 7: 3 D Radiation patterns at the select frequency.

The results show that the first resonant frequencies of fractal antennas become lower with the order increasing, which are in accord with the conclusions presented in publication [18]. Furthermore, the outer dimension of the third order Peano antenna is smaller than the fourth order Hilbert antenna when they resonate at the similar fundamental frequency. Since the lowest frequency of UHF PD signals is about



(a) 370 MHz



(b) 700 MHz

FIGURE 8: 2 D Radiation patterns at the select frequency.

300 MHz, it is then necessary to have a third order Peano fractal antenna to detect PDs in power transformers.

### 3. Optimal Design of Peano Fractal Antenna

Previous research results [14] show that the performance of a fractal antenna is affected by many factors such as the side dimension ( $L$ ), thickness ( $k$ ) of the print circuit board (PCB), width of conductor ( $b$ ), feed point, and dielectric constant of the PCB. To obtain a Peano antenna with desired performance, the above factors need to be included and optimized in the design procedure.

A Peano fractal antenna with desirable performance and size for detecting PDs in transformers can be designed synthetically through simulation studies. The simulation model

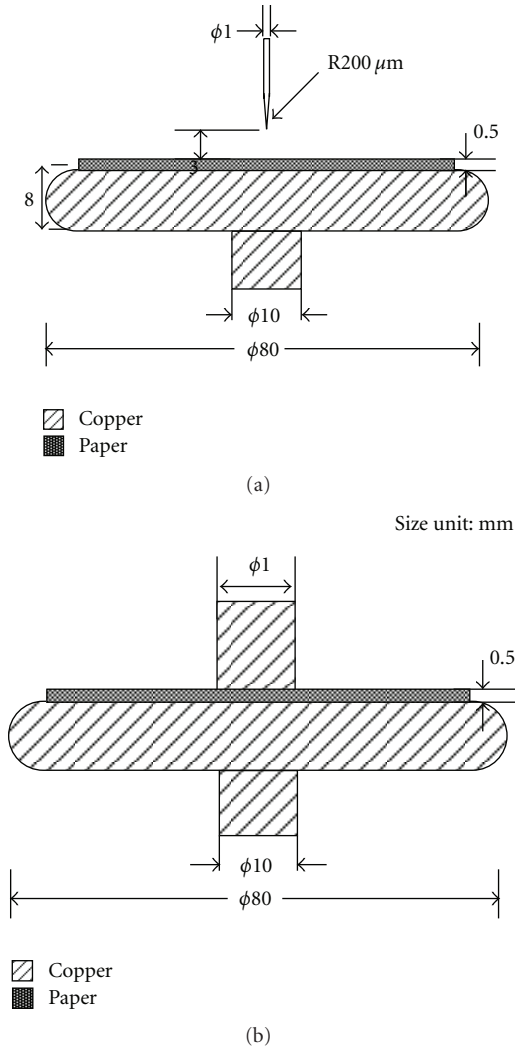


FIGURE 9: Two types of artificial defect models: (a) corona-in-oil model, (b) surface discharging-in-oil model.

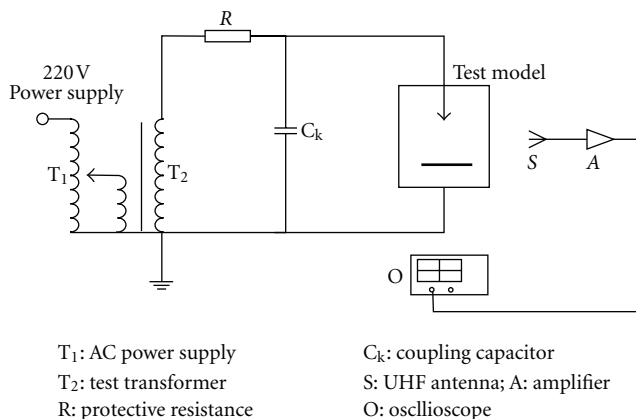


FIGURE 10: The PD experiment setup in laboratory.

TABLE 1: Resonant frequencies of Peano and Hilbert fractal antennas with different geometry parameters.

Antennas	$L$ (mm)	$n$	$b$ (mm)	$f_r$ (MHz)	
Peano	90	2	2	247.32	
		3	2	102.89	
	70	2	2	323.73	
		3	2	135.50	
	Hilbert	100	2	2	395.51
			3	2	242.92
90		4	2	141.37	
		2	2	441.73	
70		3	2	271.78	
		4	2	158.41	
		2	2	575.45	
		3	2	355.63	
		4	2	208.09	

TABLE 2: Different widths of conductor and thicknesses of PCB for antennas with different side dimension.

$L$ (mm)	$k$ (mm)			$b$ (mm)		
	Min	Step	Max	Min	Step	Max
60	1.0	—	1.0	1.0	0.5	3.0
70	1.0	0.1	1.5	1.0	0.5	3.0
80	1.0	0.1	1.5	1.0	0.5	3.0
90	1.0	0.1	2.0	1.0	0.5	3.0
100	1.0	0.1	2.0	1.0	0.5	3.0

in Ansoft contains 3 layers. The upper layer is filled with Peano curves (see Figure 1) constituted by copper; the middle layer is a board of insulating material, which is FR4 epoxy board with dielectric constant of 4.4. The down layer is a copper grounding shield.

The optimal UHF PD antenna should be with small size and wide frequency bandwidth, which was depicted in Section 1. The optimal process of a Peano fractal antenna is shown as follows. Firstly, five different side dimensions of Peano antenna were selected for simulation,  $L = 60$  mm, 70 mm, 80 mm, 90 mm, and 100 mm. For each side dimension, different widths of conductor were explored. Other factors such as thickness of PCB feed points were also simulated for the voltage standing wave ratio (VSWR), gain, and radiation pattern. The parameters used for simulation are given in Table 2. Because the Peano curve is symmetrical, 25 feed points on half of the curve are obtained as the simulation condition, which are shown in Figure 3. Parameter  $r$  is used to describe the relative locations of these feed points.  $r$  is defined as the ratio of the distance along the conductor between a feed point and its closest end to the total conduct length of the antenna. By the simulations, the optimal antenna was selected with the smallest size and the widest frequency bandwidth. The parameters of the optimal antenna are determined as  $L = 90$  mm,  $k = 2$  mm,  $b = 2$  mm, and  $r = 0.059$  (i.e., point 3 in Figure 3).

Figure 4 shows the prototype of the designed third order Peano fractal antenna. Performance curves (e.g, voltage

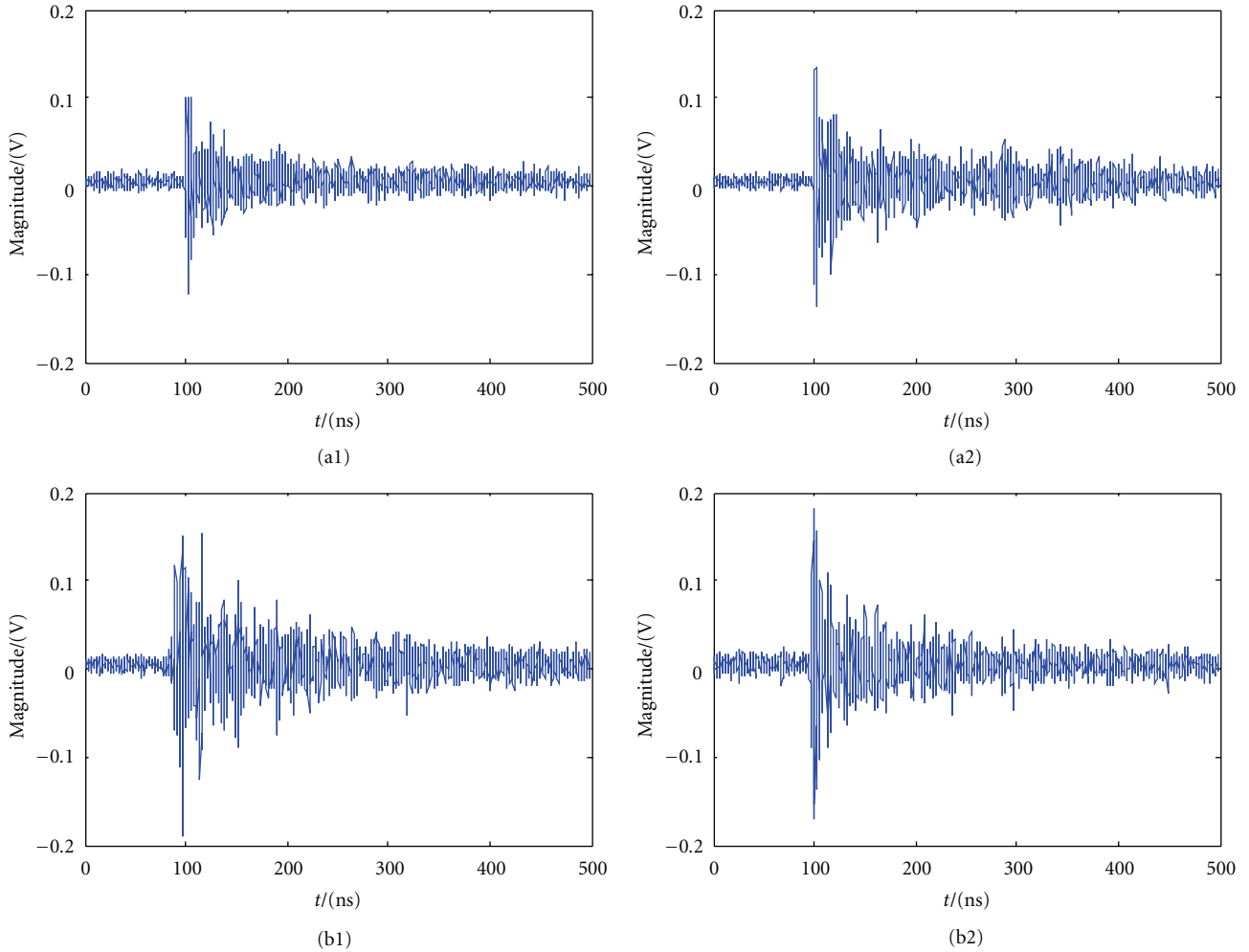


FIGURE 11: Waveforms of UHF PD signals from the two defects: (a) signals from corona and surface models detected by Hilbert antenna; (b) signals from corona and surface models detected by Peano antenna.

TABLE 3: PD experiment conditions.

Defect model	Inception voltage (kV)	Breakdown voltage (kV)	Test voltage (kV)	Sample numbers
Corona discharge	5.7	12.5	7.0	50
			8.0	50
			9.0	50
Surface discharge	8.4	13.2	9.0	50
			10.0	50
			11.0	50

standing wave ratio (VSWR), input impedance, and radiation patterns) of the antenna are given from Figures 5 to 8. Figure 5 shows that between 0.3 GHz and 1 GHz the multiband antenna has 2 resonant frequencies (370 MHz, 700 MHz), where  $VSWR < 5$ . The pass frequency bands of the antenna are approximate 340 MHz~580 MHz, 650 MHz~740 MHz, and 920 MHz~1000 MHz. Figure 6 shows the input impedance of the antenna. It is noted that the absolute

value of real part is about 50 ohms, and the absolute value of imaginary part is less than 10 ohm when frequencies are within the bandwidth of the antenna. The results show that the antenna can match with a 50 ohms coaxial cable as needed. The three-dimensional radiation patterns and two-dimensional radiation patterns ( $\phi = 0$  and  $90$  deg) at different frequencies, namely, 370 MHz and 700 MHz, are shown in Figures 7 and 8. Its patterns at the two frequencies are all nearly a hemisphere, and the gain variations at the two frequencies are relatively stable. The simulated results show that the optimal Peano fractal antenna has desirable performance with nearly wide frequency bandwidth but smaller size in comparison with the Hilbert fractal antenna reported in [14].

Figure 8 shows the minimum gain of the antenna is about -18 dBi. Besides, the detected UHF PD signals will be transferred to the processing center by the coaxial cable with the length of tens of meters. It is motivated to develop a signal processing circuit with an amplifier and a filter for the wideband detection in the frequency range between 300 MHz and 1 GHz. The gain of the amplifier is about 40 dB

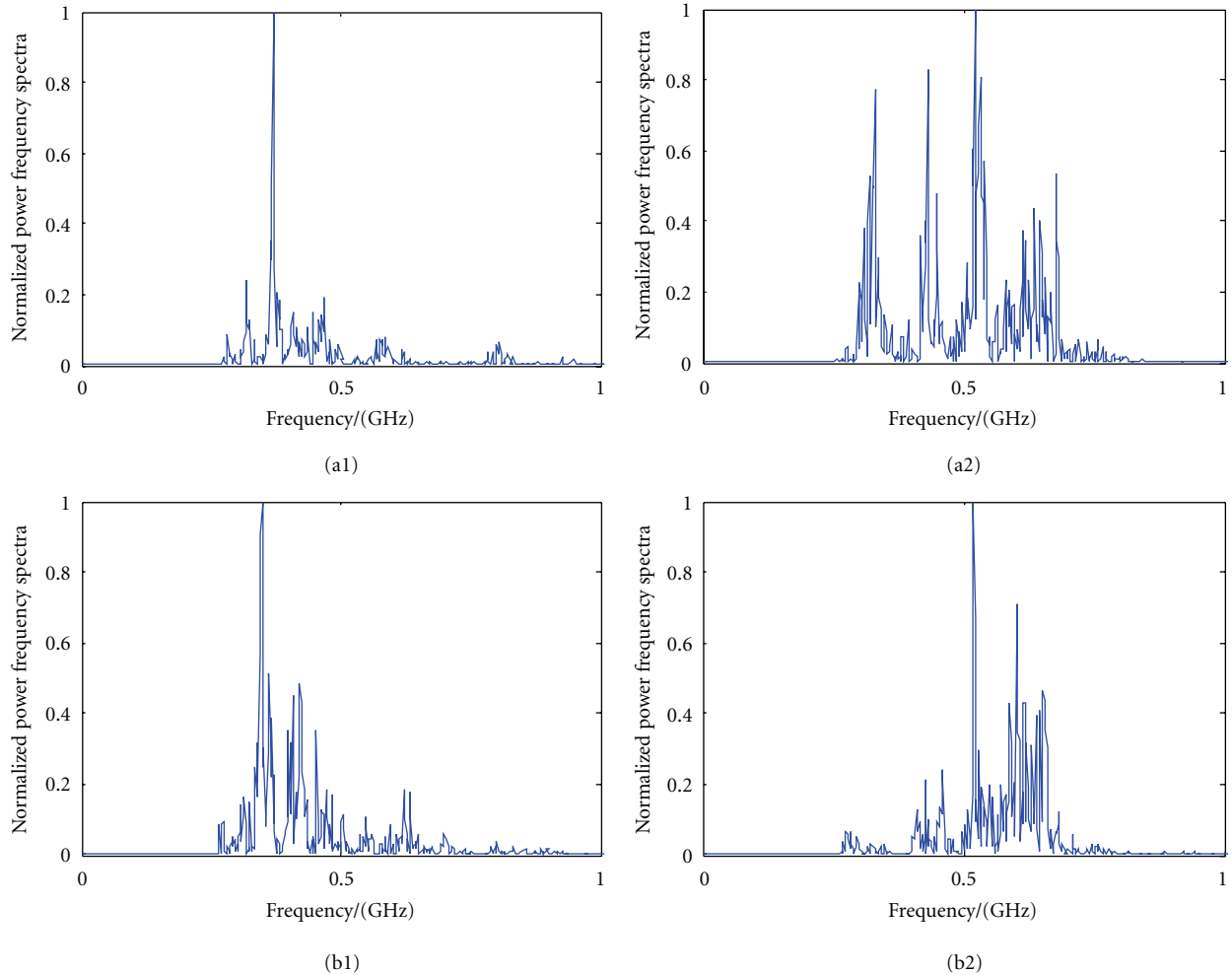


FIGURE 12: Normalized power frequency spectra of UHF PD signals from the two models: (a) signals from corona and surface models detected by Hilbert antenna; (b) signals from corona and surface models detected by Peano antenna.

between 300 MHz and 1 GHz, and the gain of the whole UHF PD system is about 20 dBi.

#### 4. Experiments and Results

To validate the performance of the designed UHF Peano fractal antenna, actual PD experiments with two typical transformer insulation defects were carried out in laboratory. The Peano and Hilbert antennas were both used to detect PD signals, as presented as follows. The performance of the existing Hilbert antenna is referred to [14].

**4.1. Defect Models Experiments.** There are two types of defect models built in experiment to generate UHF PD signals. Figure 9(a) shows the corona discharge model, which basically is a needle-to-plate electrode system. Figure 9(b) shows an experiment model of a cylinder-to-board electrode for surface discharge defects in oil. The thickness of the pressboard of each model is 0.5 mm. The experiment setup of UHF PD detection is shown in Figure 10. The artificial defect models were put into a container filled with transformer oil,

and the experiments were carried out in an electromagnetic shielded laboratory. The UHF antenna was placed beside the testing models. A digital oscilloscope was used to observe and record the UHF PD signals. The sampling frequency of the oscilloscope for recording the UHF PD signals was 5 GHz.

Table 3 shows the inception voltages, breakdown voltages, test voltages, and sample numbers of the two defect models in experiments. The Peano fractal antenna and the existing Hilbert antenna detected the PD signals at the same time. The dimension of the existing Hilbert antenna is 100 mm, and the pass frequency bands are about 450 MHz~610 MHz and 750 MHz~1000 MHz. When the test voltages were higher than the inception voltages, the transient UHF PD signals were detected by the antennas. The number of the PD samples was 50 for each model. One UHF PD signal was obtained at each voltage for every sample.

**4.2. Analysis of UHF PD Waveforms.** The differences in frequency spectra of UHF PD signals generated from the same defected model are significantly smaller than those generated from different types of defected models. Thus Figure 11

shows the examples of detected UHF PD signals of the two defect models by the two antennas. The UHF PD signals look similar but differ in details. The examples of normalized power frequency spectra of the measured UHF PD signals, generated by the two defect models, detected by the two antennas, are shown in Figure 12. The results show that the Peano fractal antenna with smaller dimension is also qualified for UHF PD detection. Besides, the spectra of the UHF PD signals detected by the proposed antenna even are a little wider than that detected by the Hilbert antenna, especially for the UHF PD signal generated by the corona discharge model. This implies that the Peano fractal antenna is a little more suitable than the Hilbert fractal antenna for pattern recognition by analyzing the waveforms of detected UHF PD signals.

## 5. Conclusions

This paper presents a compact multiband UHF Peano fractal antenna for PD online monitoring of high voltage power transformers. The approximate formula for calculating the first resonant frequency of the Peano fractal antenna was presented. The actual antenna was developed based on the optimal design procedure. The actual PD experiments were carried out to verify the performance of the antenna. The results of the work are concluded as follows.

- (a) In comparison with the first resonant frequency of the Hilbert fractal antenna calculated by the formula, the outer dimension of the third order Peano antenna is smaller than the fourth order Hilbert antenna when they resonate at the similar fundamental frequency. This implies that the outer dimension of the Peano fractal antenna is smaller than the Hilbert fractal antenna when their performances are similar.
- (b) The frequency passband of the developed Peano fractal antenna is hundreds of MHz. The radiation patterns show that the antenna can receive electromagnetic waves from the front of the antenna. The actual PD experiments including two typically artificial oil-paper defects were carried out to verify the performance of the antenna. In comparison with the existing Hilbert fractal antenna, the experimental results show that the proposed antenna with smaller dimension is also effectively applied for PD online monitoring of transformers.
- (c) The spectra of the UHF PD signals detected by the two antennas show that the PD signals measured by the UHF Peano fractal antenna are a little wider than that detected by the Hilbert antenna, especially for the corona discharge. It implies that the Peano fractal antenna is a little more suitable for pattern recognition by analyzing the waveforms of detected UHF PD signals.

In the future, there is still scope for improvement in manufacturing a compact fractal antenna with higher gain. The modeling of the fractal antenna including the dielectric loading effect will be investigated. Further studies are also

needed to establish protocols for recognition of UHF PD signals.

## Acknowledgments

This work was supported in part by the funding of the 863 Program (no. 2011AA05A120) of China. The Natural Science foundation of China (Project no. 51021005) and the 111 Project of Ministry of Education, China (B08036), are also appreciated for supporting this work.

## References

- [1] F. H. Kreuger, *Partial Discharge Detection in High-Voltage Equipment*, Butterworths, London, UK, 1989.
- [2] W. Gao, D. Ding, and W. Liu, "Research on the typical partial discharge using the UHF detection method for GIS," *IEEE Transactions on Power Delivery*, vol. 26, pp. 2621–2629, 2011.
- [3] Y. Shibuya, S. Matsumoto, M. Tanaka, H. Muto, and Y. Kaneda, "Electromagnetic waves from partial discharges and their detection using patch antenna," *IEEE Transactions on Dielectrics and Electrical Insulation*, vol. 17, no. 3, pp. 862–871, 2010.
- [4] T. Pinpart and M. D. Judd, "Differentiating between partial discharge sources using envelope comparison of ultra-high-frequency signals," *IET Science, Measurement and Technology*, vol. 4, no. 5, pp. 256–267, 2010.
- [5] S. Tenbohlen, D. Denisov, S. M. Hoek, and S. M. Markalous, "Partial discharge measurement in the ultra high frequency (UHF) range," *IEEE Transactions on Dielectrics and Electrical Insulation*, vol. 15, no. 6, pp. 1544–1552, 2008.
- [6] D. Aschenbrenner, H. G. Kranz, W. R. Rutgers, and P. Van Den Aardweg, "On line PD measurements and diagnosis on power transformers," *IEEE Transactions on Dielectrics and Electrical Insulation*, vol. 12, no. 2, pp. 216–222, 2005.
- [7] R. Sarathi and G. Koperundeivi, "UHF technique for identification of partial discharge in a composite insulation under AC and DC voltages," *IEEE Transactions on Dielectrics and Electrical Insulation*, vol. 15, no. 6, pp. 1724–1730, 2008.
- [8] G. Wang, Y. Hao, and Y. Li, "Study on the ultra-high-frequency sensors for PD detection in power transformer," in *Proceedings of the International Symposium on Electrical Insulation Materials (ISELM '01)*, pp. 793–796, Himeji, Japan, November 2001.
- [9] W. Wang, C. R. Li, Z. Tang, Z. Li, and Y. Ding, "An on-line UHF PD monitoring system for power transformers," in *Proceedings of the Conference Record of IEEE International Symposium on Electrical Insulation*, pp. 50–53, Indianapolis, Ind, USA, September 2004.
- [10] Z. Lixing, L. Weiguo, and S. Sheng, "The deduction of partial discharge pulse current from its radiating UHF signal," in *Proceedings of the 7th International Power Engineering Conference (IPEC '05)*, pp. 189–193, Singapore, December 2005.
- [11] Z. Jin, C. Sun, C. Cheng, and J. Li, "Two types of compact UHF antennas for partial discharge measurement," in *Proceedings of the International Conference on High Voltage Engineering and Application (ICHVE '08)*, pp. 616–620, Chongqing, China, November 2008.
- [12] J. Tang, G. Wei, and X. Zhang, "External sensors in partial discharge ultra-high-frequency measurements in gas-insulated substations," *European Transactions on Electrical Power*, vol. 22, no. 4, pp. 559–570, 2012.

- [13] S. Kaneko, S. Okabe, M. Yoshimura, H. Muto, C. Nishida, and M. Kamei, "Detecting characteristics of various type antennas on partial discharge electromagnetic wave radiating through insulating spacer in gas insulated switchgear," *IEEE Transactions on Dielectrics and Electrical Insulation*, vol. 16, no. 5, pp. 1462–1472, 2009.
- [14] J. Li, T. Jiang, C. Wang, and C. Cheng, "Optimization of UHF hilbert antenna for partial discharge detection of transformers," *IEEE Transactions on Antennas and Propagation*, vol. 60, pp. 2536–2540, 2012.
- [15] J. Zhu, A. Hoorfar, and N. Engheta, "Bandwidth, cross-polarization, and feed-point characteristics of matched Hubert antennas," *IEEE Antennas and Wireless Propagation Letters*, vol. 2, pp. 2–5, 2003.
- [16] K. J. Vinoy, K. A. Jose, V. K. Varadan, and V. V. Varadan, "Resonant frequency of Hilbert curve fractal antennas," in *Proceedings of the IEEE Antennas and Propagation Society International Symposium—FDTD and Multi-Resolution Methods-*, pp. 648–651, Boston, Mass, USA, July 2001.
- [17] Z. Jin, C. Sun, C. Cheng, and J. Li, "Two types of compact UHF antennas for partial discharge measurement," in *Proceedings of the International Conference on High Voltage Engineering and Application (ICHVE '08)*, pp. 616–620, Chongqing, China, November 2008.
- [18] J. Zhu, A. Hoorfar, and N. Engheta, "Peano antennas," *IEEE Antennas and Wireless Propagation Letters*, vol. 3, no. 1, pp. 71–74, 2004.
- [19] X. Chen, S. N. Safieddin, and Y. Liu, "A down-sized printed Hilbert antenna for UHF band," in *2003 IEEE International Antennas and Propagation Symposium and USNC/CNC/URSI North American Radio Science Meeting*, pp. 581–584, Columbus, Ohio, USA, June 2003.
- [20] T. Endo, Y. Sunahara, S. Satoh, and T. Katagi, "Resonant frequency and radiation efficiency of meander line antennas," *Electronics and Communications in Japan, Part 2*, vol. 83, pp. 52–58, 2000.

## Research Article

# A Selective Ink Deposition Method for the Cost-Performance Optimization of Inkjet-Printed UHF RFID Tag Antennas

J. Virtanen,<sup>1</sup> J. Virkki,<sup>1</sup> A. Z. Elsherbeni,<sup>2</sup> L. Sydänheimo,<sup>1</sup> and L. Ukkonen<sup>1</sup>

<sup>1</sup>Department of Electronics, Rauma Research Unit, Tampere University of Technology, 33720 Tampere, Finland

<sup>2</sup>Department of Electrical Engineering, University of Mississippi, Oxford, MS 38677, USA

Correspondence should be addressed to J. Virtanen, juha.virtanen@tut.fi

Received 27 January 2012; Accepted 14 March 2012

Academic Editor: Fan Yang

Copyright © 2012 J. Virtanen et al. This is an open access article distributed under the Creative Commons Attribution License, which permits unrestricted use, distribution, and reproduction in any medium, provided the original work is properly cited.

A selective ink deposition method is proposed for fabricating inkjet-printed passive UHF RFID tag antennas with optimized cost-performance ratios. The deposition method is based on identifying areas with high surface current densities on a given tag antenna and applying additional silver nanoparticle ink onto such areas to increase tag read range. In this paper, the proposed method is experimentally verified by utilizing the method on a small dipole tag antenna. Several ink deposition schemes are created, and their read range performances and ink consumptions are presented.

## 1. Introduction

Inkjet-printing technology is a prominent technique of manufacturing low-cost passive ultra-high frequency (UHF) radio frequency identification (RFID) tag antennas using inks with metal content. Inkjet printing provides a fully additive, noncontact deposition method and thus lowers production costs by minimizing material waste [1] and by allowing fast mass customization [2]. Furthermore, inkjet-printing technology enables the use of ultra-low cost and environmentally safe materials, for example, paper and wood, as substrates in diverse electronic applications.

One of the possible applications of inkjet-printing technology in electronics is printable antennas, especially RFID tag antennas as inkjet printing could lower tag manufacturing costs and allow tags to be printed directly onto product packages. Thus, inkjet-printed antennas have been developed for various kinds of RFID tags in [3–8] and for wireless sensor networks in [9, 10]. At the moment, despite the obvious benefits and possible cost savings of inkjet-printed antennas, their cost remains too high due to the high cost of conductive inks.

A special feature of additive fabrication methods is their ability to vary the amounts of materials used to form structures on the substrate. Significant material savings are therefore possible by selectively depositing materials to areas

within the design that gain the greatest benefits from it, for example, in the form of increased performance.

In the case of antenna structures, such selective deposition of materials, mainly metals, can be done in three ways. In the first approach, the antenna structure can be printed using multiple overlapping layers of conducting ink, as in [11], to create tags with varying read ranges and costs. In [11], the read range, that is, the operating range of the tags, was greatly improved with this method.

In the second approach, solid antenna structures can be divided into grids, as in [12]. In [12], material savings in excess of 50% are reported. However, dividing the antenna into grids will change the input impedance of the antenna and eventually decrease the power transfer between the antenna and RFID IC. Furthermore, the effects of this method on the performance of the antenna and in the read range of the tag are not known.

A third, more sophisticated approach is to add conductive metallization to areas with high current density. In [13], the authors have used flexographic printing to increase the thickness of the conducting ink layer in selective areas with supposedly high surface currents. This has also led to great savings in the ink consumption. This method does not cause any additional impedance mismatching, eliminating the need for retuning the antenna impedance after optimization.

This paper presents a further developed version of the latter approach especially for inkjet-printed tag antennas fabricated using silver nanoparticle ink. The developed selective ink deposition method relies on high-precision simulations to identify areas in the antenna structure with sufficiently high surface current density on a given tag. As the method relies on results from a full-wave 3D simulator, the antenna geometry, on which the deposition method is utilized, can be extremely complex. Furthermore, the positional accuracy of individual droplets deposited by and inkjet-printed is excellent and allows pixels to be printed with micrometer precision. The method is demonstrated with a case example, where the ink consumption to fabricate a high performance dipole-type tag antenna is optimized.

## 2. Ink Deposition Method for Cost-Performance Optimization

The need for methods reducing the amount of conductive ink to produce well performing inkjet-printed UHF RFID tag antennas is caused by the intrinsic property of the fabrication technology. Typically, the thicknesses of conductors formed by inkjet printing are well below the skin depth of the typical printed metals at the global 860 MHz to 960 MHz UHF RFID band. This leads to poor radiation efficiency due to power losses in the conductors.

Power losses in an arbitrary conductor are proportional to the square of the current flow through the conductor

$$P_{\text{loss}} = \int_S RI^2 \cdot dS. \quad (1)$$

The resistance of the conductor is related to the resistivity of the conductive material, to the length of the conductor and to its cross-sectional area. At high frequencies, the effective conducting cross-sectional area of the conductor is decreased due to the skin effect. Due to this effect, the current travels almost completely at the surface of the conductor. The depth, at which the amplitude of the electric field has decayed by  $1/e$ , is known as the skin depth of the conductor. The skin depth of a conductor can be calculated as [14]

$$\delta = \sqrt{\frac{2}{\omega\mu\sigma}} = \sqrt{\frac{\rho}{\pi f\mu}}, \quad (2)$$

where  $\omega$  is the angular frequency,  $\mu$ ,  $\sigma$ , and  $\rho$  are the permeability, conductivity and resistivity of the conducting material. For a conductor to have minimal losses due to the skin effect, its thickness needs to be around four to five times as thick as the skin depth of the conducting material.

For example, the skin depth of the silver nanoparticle ink used in the experiments made for this study at 900 MHz is 3.4–4.1  $\mu\text{m}$  according to the data provided by the ink manufacturer [15]. Inkjet-printed conductors are usually at around 0.5 to 2  $\mu\text{m}$  in thickness [16, 17], depending on the process parameters such as the type of ink and substrate, printing resolution, and so forth. Therefore, in order to fabricate tag antennas with good radiating efficiencies, multiple overlapping layers of ink need to be used. This will

lead to high productions costs if the whole antenna structure is printed multiple times.

The power losses in the antenna can be minimized without printing the whole antenna structure using multiple layers, additional metal needs to be added only to areas with high surface current levels. In order to optimize the ink consumption, these areas with high surface currents need to be identified as accurately as possible. For this purpose, a full-wave 3D electromagnetic field simulator is utilized. The simulator is used to plot the magnitude of the complex surface current on the surface of any arbitrary planar antenna suitable for inkjet printing. Choosing to plot the complex magnitude of the surface current allows for a quick way of plotting the amplitudes of the apparent surface current density vectors. Therefore, layouts for inkjet printing are obtainable directly from a single image.

The complex surface current is plotted at the design frequency of the tag antenna. It is crucial that the tag antenna's metallization is modeled using the electrical properties of the ink used in the process since it will have an effect on the current distribution on the surface of the antenna.

After the surface current distribution has been plotted, the resulting plot is used as a printing mask for the printer to add ink to these areas. The key research problem at this stage is to determine a sufficient magnitude of surface current density which is used as a printing mask to optimize the radiation efficiency and ink consumption. This research problem is addressed in Section 3, where multiple printing masks are created, each based on different surface current density levels, to discover the optimal mask pattern.

Inkjet-printing technology is perfectly suited for this type of deposition method since individual drops of ink can be placed on the substrate with great accuracy. For example, the positional repeatability of the printer used in the experiments made for this study is  $\pm 25 \mu\text{m}$ . Therefore, the printing masks which selectively add ink can be created using high resolution. As such, the thickness of the resulting antenna can be controlled pixel by pixel.

## 3. Experimental Verification

This section presents the experimental verification of the selective deposition method in order to optimize the performance of a typical tag antenna while minimizing the amount of ink required to fabricate the antenna.

*3.1. Test Antenna Structure.* A short dipole-type tag antenna, shown in Figure 1, was chosen for these experiments as it represents a typical antenna found in passive UHF RFID tags. The antenna is attached to a passive Higgs-3 RFID IC from Alien Technology [18].

The test tag antenna will be printed on top of 51  $\mu\text{m}$  thick 200 HN Kapton film [19]. Kapton is a low-loss, polyimide film which provides a smooth, heat-resistant surface for high precision inkjet printing. The test tag antenna is equipped with a T-match, an impedance matching structure [20], to match the input impedance of the tag antenna to the complex conjugate of the RFID IC input impedance. The T-matching

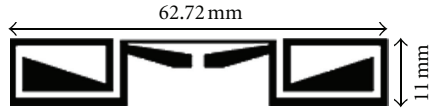


FIGURE 1: Tag antenna layout used in the experiments.

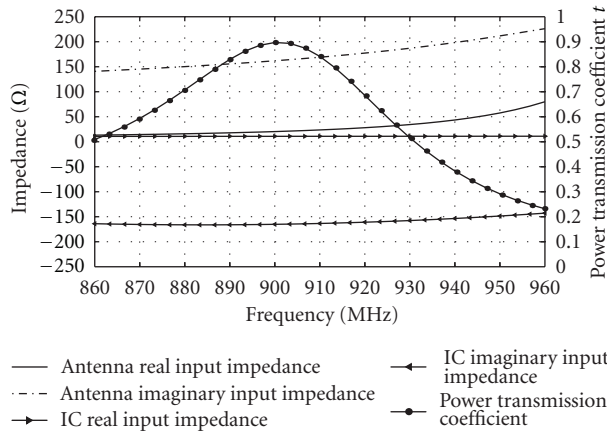


FIGURE 2: Simulated tag antenna input impedances and power transmission coefficient between the IC and tag antenna.

network is thus used to provide maximal power transfer between the IC and tag antenna [21]. The magnitude of the power transfer is described by a power transmission coefficient.

The power transmission coefficient illustrates the amount of power loss due to improper impedance matching between the tag antenna and RFID IC [22]. The power transmission coefficient  $\tau$  can be calculated by

$$\tau = \frac{4\text{Re}_A\text{Re}_{IC}}{|Z_A + Z_{IC}|^2}, \quad (3)$$

where  $\text{Re}_A$  and  $\text{Re}_{IC}$  are the real parts of the tag antenna and RFID IC, respectively.  $Z_A$  and  $Z_{IC}$  are the corresponding input impedances of the antenna and IC. The simulated input impedances of the antenna and Higgs-3 IC, obtained from [23], as well as the resulting power transmission coefficient are shown in Figure 2.

The simulations were performed using Ansoft HFSS 13 [24], a finite element method-based, 3-D full-wave electromagnetic simulator software. The ink layer thickness in these simulations was set to  $1.5 \mu\text{m}$  (uniform) and the conductivity of the ink to 20 MS/m. Kapton 200 HN was simulated using a relative permittivity of 3.5 and a loss tangent of 0.002.

The test antenna is optimally matched around 880 MHz to 920 MHz to the input impedance of IC. Figure 3 shows the simulated directivity, gain, realized gain, and radiation efficiency of the tag antenna.

The simulated radiation efficiency is only approximately 0.25 at the optimal operating frequency band. This indicates that the thickness of the conductor is not sufficient to provide low-loss operation if only a single layer of ink is deposited.

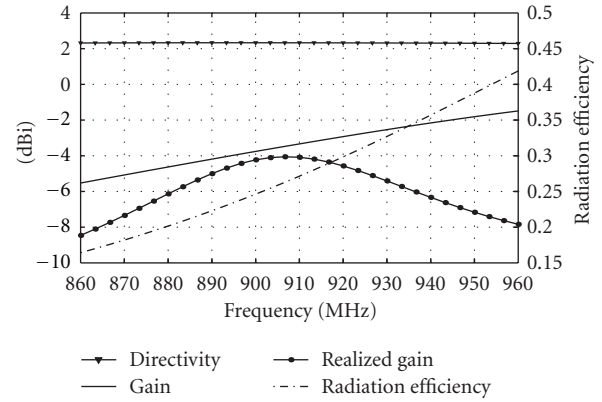


FIGURE 3: Simulated tag antenna directivity, gain, and radiation efficiency.

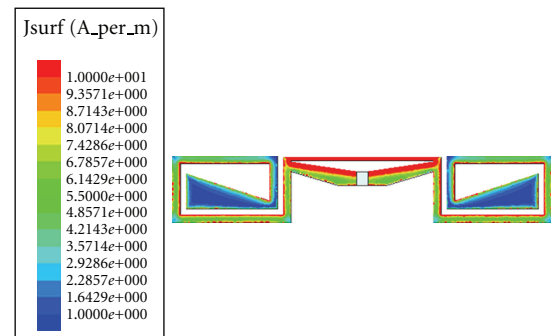


FIGURE 4: Simulated magnitude of complex surface density on the test antenna at 900 MHz.

**3.2. Selective Deposition Masks.** To identify the areas in need for a thicker ink layer, the surface current density on the tag antenna was plotted, in Figure 4, at the tag's optimal operating frequency.

At this stage, there are many options on how to form the selective deposition masks. The main problem is to define the current density level which justifies increasing the ink layer. Selecting an inadequate level will lead to increased ink consumption, while selecting a level too high will lead to poor performance. In this study, the problem has been addressed so that the surface current density level at the center of the dipole arm ends (dark blue areas in Figure 4) was used as a reference level.

To test which surface current level is adequate for optimizing the cost-performance relation, three different selective deposition masks were created. First of these masks, called *5 mask*, was created by plotting the complex surface currents that exceed the reference surface current density level by 500%. The final two masks were created similarly using 1000%, *10 mask*, and 4000%, *40 mask*, as the relative surface current levels. All three resulting printing masks formed using the simulated surface current levels are shown in Figure 5.

Two additional selective deposition masks were created without EM simulations to verify the effectiveness of the masks created via EM simulations. One of these masks

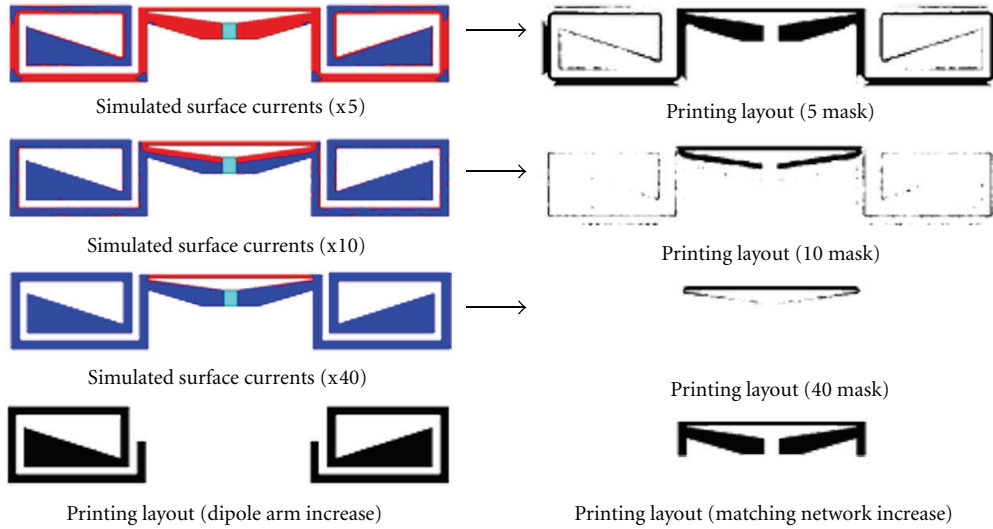


FIGURE 5: Deposition masks used in this study.

TABLE 1: Absolute and relative amount of printed pixels in each deposition mask (1 layer).

Deposition mask	Printed pixels (abs.)	Relative amount of printed pixels
Full antenna	$3.95 \cdot 10^4$	100%
5 mask	$2.31 \cdot 10^4$	58.4%
10 mask	$6.65 \cdot 10^3$	16.9%
40 mask	$2.40 \cdot 10^3$	6.10%
Dipole arms (DA)	$3.05 \cdot 10^4$	77.4%
Matching network (DM)	$9.27 \cdot 10^3$	23.6%

increases the ink thickness on the dipole arms only, while the other increases the ink layer only in the matching network area. The matching network increase mask also serves as a good example of a case in which the selective deposition is made based on assumption that high surface currents are found on the impedance-matching network.

Table 1 lists the amount of printed pixels, at 282 dpi which is used as the printing resolution of the samples, and the relative difference in total amount of pixels compared against the full increase case. As it is seen from Table 1, the selective deposition masks bring significant savings in the manufacturing costs by reducing the amount of printed pixels to a small portion of the amount required to print the full antenna pattern.

**3.3. Printing Process Parameters.** Tag antenna samples were printed by Dimatix DMP-2800 inkjet material printer [25] equipped with 10 pl print head nozzles. Harima NPS-JL silver nanoparticle ink [15] was used as the conductive ink. The printing resolution was set to 282 dpi, 90  $\mu\text{m}$  drop spacing as the mean drop size on the Kapton HN200 was found to be around 120  $\mu\text{m}$ . The substrate, Kapton HN200, was cleaned with isopropyl alcohol before printing. After

printing, the samples were cured for 40 minutes at 200°C between layers.

The workflow of the process involving selective deposition was as follows. First the full antenna patterns were printed on the substrate and cured. Samples were brought back from the oven, and additional ink was applied using the selective deposition masks. Finally, the samples were brought back for curing.

The full antenna structure was printed using one to five layers of ink, while the specific deposition masks were printed using one to four layers onto a single layer full antenna structure. Therefore, for example, samples printed using two full antenna layers, and single specific deposition masks should share similar maximum thicknesses.

**3.4. Results.** The thickness of the inkjet-printed layer was measured optically through cross-sectional images. The thickness per printed layer was found to be around 1.4  $\mu\text{m}$ . Therefore, the printed antennas have thicknesses ranging from 1.4  $\mu\text{m}$  to 7.0  $\mu\text{m}$ . Figure 6 shows a cross-sectional image from a sample printed with five ink layers.

However, the thickness of the ink layer depends on the printing direction line width of the conductor, and, therefore, thickness varies significantly in a given sample in different areas.

The obtained thickness results agree with other inkjet-related research publications, for example, in [26, 27], that show that the typical thickness per layer is between 0.5  $\mu\text{m}$  and 1.5  $\mu\text{m}$  if no surface treatment is made for the substrate material. Using 5  $\mu\Omega \cdot \text{cm}$  as the mean resistivity for the NPS-JL ink, the printed tag antenna sample thicknesses, expressed in terms of skin depths, range from 0.4 to 1.9.

Figure 7 shows microscopic images taken from the surface of the inkjet-printed tag antenna samples. Figures 7(a) and 7(b) show the quality of the printed surface with one and four layers of ink. These images show that the surface becomes smoother as more layers are added. Figures 7(c) and

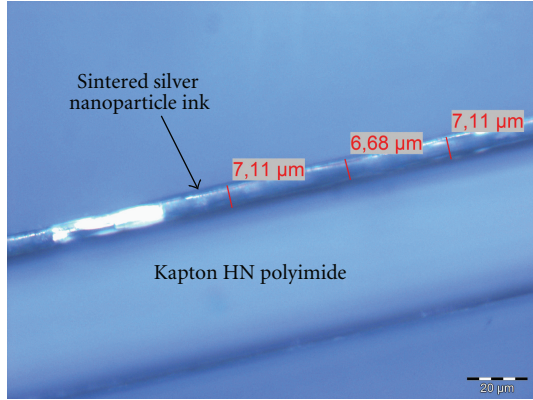


FIGURE 6: Cross-sectional image from an inkjet-printed tag antenna printed using five ink layers. The measured mean thickness of the silver ink layer is  $6.97 \mu\text{m}$ .

7(d) show examples from surfaces which have additional ink layers selectively deposited using one and four layers.

Using selective deposition to add ink on top of the existing ink surface does not change the dimensions of the tag antenna if the alignment of the additional layer is done properly. It was also verified optically that the ink does not spread excessively when new layers are added using the printing parameters described in Section 3.3.

Theoretical read range was selected as the main tag performance metric in this study. Theoretical read range is the maximal read range, that is, maximum tag to reader antenna distance at which the tag is still able to gather enough power to provide a valid response in free-space conditions. This performance is affected by both the RFID IC sensitivity level as well as the tag antenna radiation properties. As the IC properties remain constant in the measurements performed in this study, any changes in the read range can be considered due to the alternated operation characteristics of the tag antenna.

The theoretical read ranges of the fabricated samples were measured using Tagformance measurement equipment [28] in a compact anechoic UHF RFID measurement chamber. A linear patch-type antenna was used as the reader antenna with a 0.45 cm separation to the tag under test. Tagformance measurement system calculates the theoretical read range based on the measured path-loss and threshold power, that is, transmit power level at the generator output required to activate the tag under test. This calculation is made according to the following equation:

$$d_{\text{Tag}} = \frac{\lambda}{4\pi} \sqrt{\frac{\text{EIRP}}{P_{\text{TS}} L_{\text{fwd}}}}, \quad (4)$$

where EIRP is the maximal allowed equivalent radiated power by the regulations (3.28 W in Europe [29]),  $P_{\text{TS}}$  is the threshold power of the tag under test, and  $L_{\text{fwd}}$  is the measured path loss in the forward link in the measurement setup.

The measured theoretical read range of each deposition mask and layer quantity is shown in Figure 8. Table 2 lists the

TABLE 2: Ink consumptions to form the deposition masks and their maximal achieved read ranges.

Deposition mask	Ink consumption to form the mask	Overall achieved peak read range
Full antenna	$0.40 \mu\text{L}$	7.2 m
5 mask	$0.23 \mu\text{L}$	6.8 m
10 mask	$0.06 \mu\text{L}$	5.1 m
40 mask	$0.02 \mu\text{L}$	4.0 m
Dipole arms	$0.30 \mu\text{L}$	3.5 m
Matching network	$0.09 \mu\text{L}$	4.6 m

achieved peak read ranges of each deposition masks as well as the total ink consumption required to print the masks using 10 pl print nozzles.

The deposition mask in which the full antenna is printed multiple times shows great performance increase as additional layers are added. The peak read range rises from 3.2 meters (1 layer) to 7.2 meters (5 layers), equaling a relative increase of 125%.

The selective deposition masks also show great gains in the peak range of the tag although the increase in the amount of printed pixels is significantly lower than in the case in which the full antenna was printed. Samples printed with the selective deposition mask *5 mask* nearly match the performance of the full antenna increase mask. In this case the peak read range rises monotonically from 3.9 meters (1 layer) to 6.8 meters (4 layers), a 74% increase.

Samples printed with the *10 mask* also show great read range improvements. The maximal read range rises monotonically from 4 meters to 5.1 meters, a 27.5% increase in read range. In this case, the data shows that the maximal read range has already saturated between samples printed with four and five layers.

Samples made with selective deposition mask *40 mask* show the smallest increases in their read ranges between layers. In this case, the read ranges increase monotonically from 3.4 meters to 4 meters, an 18% relative increase. The measured results show that *40 mask* has the potential to provide further gains in the peak read range if more layers are added.

The reference selective deposition masks *dipole arm increase* and *matching network increase* show mixed performances. The read range results acquired with samples printed with the *dipole arm increase* actually decrease slightly as more layers are added. The decrease in the read range is likely to be caused by variations in the RFID IC sensitivities or in the IC-antenna joint. Thus, it can be considered that the read range of the *dipole arm increase* samples remains constant regardless of the amount of ink layers. The peak read range starts at 3.5 meters (1 layer) and drops down to 3.4 meters (4 layers). These results show clearly that increasing the ink layer thickness only in the dipole arms is highly inefficient.

Samples printed with the *matching network increase*, however, show monotonically increasing peak read ranges. In this case, the peak read range starts at 3.2 meters and rises

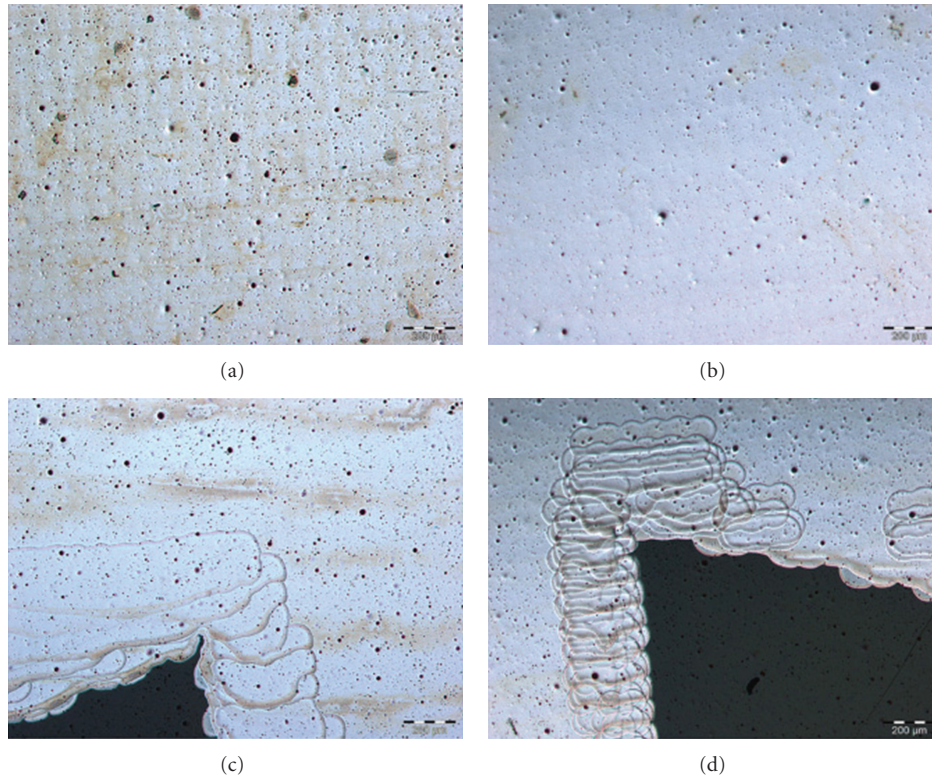


FIGURE 7: Microscopic images from the inkjet-printed tag antennas. (a) Surface of a sample printed with a single layer. (b) Surface of a sample printed with four full layers. (c) Selective ink deposition with one layer. (d) Selective deposition with four layers.

to 4.6 meters, a relative increase of 43.8%. The performance of these samples is starting to saturate between three and four layer samples. This result shows that moderate read range gains are possible by printing the area around the impedance matching network without any EM simulation optimization.

To examine the cost performance of each deposition mask, the peak read range results of each sample need to be plotted against their ink consumption (uncured volume). The peak read ranges of each sample are plotted as a function of their ink consumptions in Figure 9. In Figure 9, the measured peak ranges of each sample are indicated by round markers. The solid lines represent second-order polynomial fits that describe the trend of the read range behavior as layers are added. Dashed lines represent the estimated performance increase if more layers were to be added to selected deposition masks.

Judging from the data on Figure 9, each of the selective deposition masks acquired through EM simulations shows greater performance-to-cost ratio than the full increase mask. Considering only their efficiencies, *10 mask* is clearly the most efficient deposition mask as it produces relatively long read ranges with low ink consumption. The most inefficient method is to add ink to the dipole arms only.

One of the interesting points in Figure 9 is the estimated future trend of *5 mask*. According to the projected performance of *5 mask*, a tag antenna printed using such selective deposition could match the peak read range of a tag

antenna printed using full antenna pattern while providing cost savings.

Figure 10 shows the calculated performance to cost ratio of each deposition mask. The ratio in this case is calculated by dividing the peak read range by the total volume of ink needed to form the resulting antenna.

The performance-to-cost ratios reveal the deposition masks which are the most efficient in terms of producing long read ranges with a set volume of ink. The selective deposition masks made through EM simulations are all showing greater performance-to-cost ratios, after two printed layers, than the full increase mask. Also, the *matching network increase* shows good ratios, exceeding even the *5 mask* in each layer quantity. The poor performance of the *dipole arm increase* is again highlighted by this graph. *10 mask* is showing greater performance to cost ratio than the full increase mask at every amount of layers.

Table 3 lists the possible savings in ink consumption per tag antenna at different performance criteria. The data presented is based on Figure 9. For example, if a read range of five meters is only needed, it can be achieved by printing a single full antenna layer followed by three layers made with *10 mask*. Such printing process would nearly half the ink consumption compared to the case where the full antenna would have to be printed using three full layers. In Table 3, the seven meter performance criteria result is based on the projected performance of a *5 mask* sample with five layers of ink.

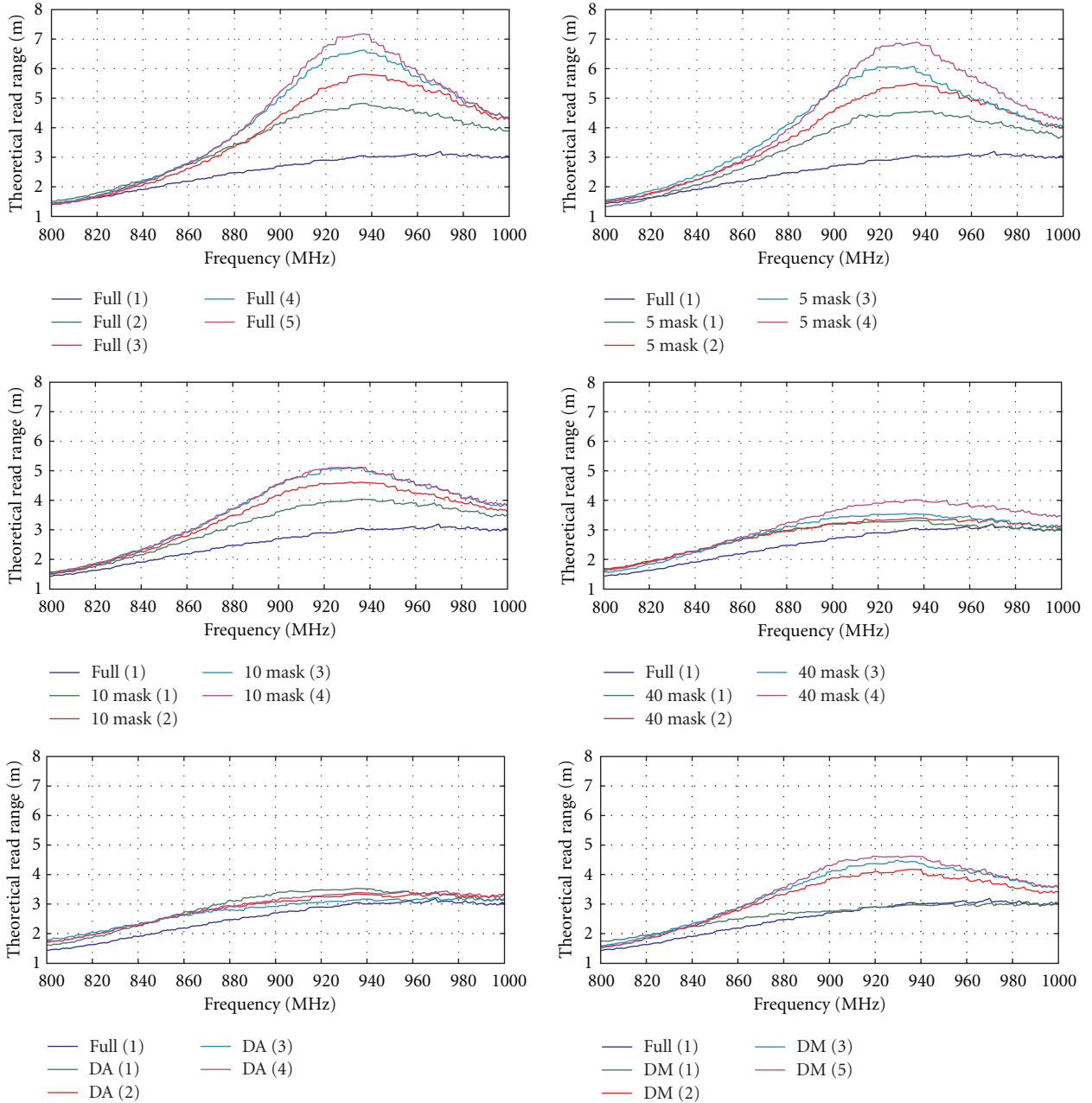


FIGURE 8: Measured theoretical read ranges of each deposition mask.

TABLE 3: Ink savings at different tag performance criteria.

Performance criteria	Selected deposition mask	Possible savings in ink consumption
7 m	5 mask ( <i>projected</i> )	22.1%
6 m	5 mask	31.1%
5 m	10 mask	49.8%
4 m	10 mask	41.6%

The results in Table 3 show that the use-selective deposition masks can greatly drop the ink consumption needed

to produce high performance UHF RFID tag antennas. Furthermore, the use of selective ink deposition speeds up the fabrication process as the printer is able to skip the empty pixels in the printing pattern. Therefore, the production costs of inkjet-printed tag antennas can be reduced significantly without any major changes in the production processes or design stages of the antennas.

#### 4. Discussion of Experimental Results

The obtained results show that selective deposition can be used to significantly reduce the amount of conductive ink and time to fabricate a passive, high performance, UHF

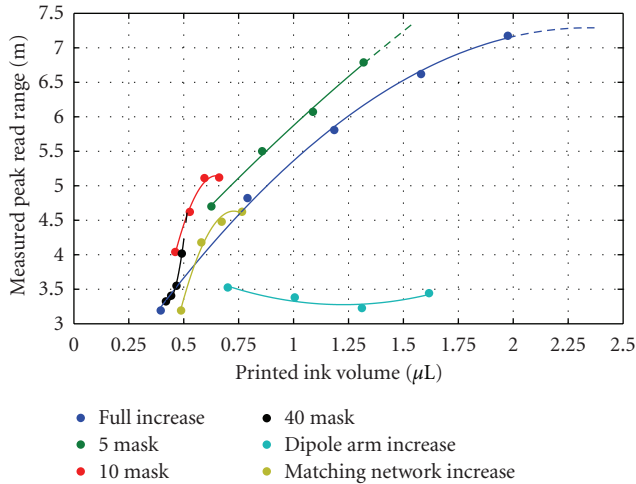


FIGURE 9: Measured peak read ranges as a function of ink consumption (uncured volume).

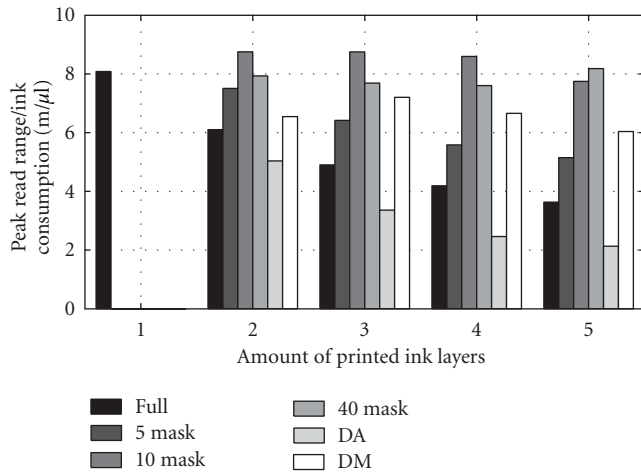


FIGURE 10: Peak read range to ink consumption ratios.

RFID tag antenna using inkjet printing. The impedance matching between the tag antenna and IC remains unaffected by the use of selective deposition. This shows that selective deposition can be used with arbitrary planar tag antenna designs without considering nonuniform ink layer thickness in their design stage.

Read range wise, the samples printed with the full antenna pattern using multiple layers produced the highest read ranges with the amount of ink layers used in this study. None of the samples printed with selective deposition neither matched nor reached the read range of the samples printed using the full antenna pattern. However, if more ink layers were to be added, the performance of the samples printed with *5 mask* could match and even exceed the read range levels of the full increase case. This suggests that tag arbitrary antennas printed with selective deposition can achieve similar maximal read ranges as tags which are printed using full layers if the optimal surface current level is used as the printing mask.

Of the three selective deposition masks created via simulations, the one, which adds ink to areas exhibiting ten times higher surface current density than the dipole arm end areas, *10 mask*, has the greatest performance to cost ratio. Therefore, in the case of the test antenna, the best cost-performance ratio is achieved when ink is added to the inner portions of the impedance-matching network and dipole arms.

The selective deposition mask not created via simulations and that adds ink only to the impedance-matching network area in the tag antenna performs reasonably well in terms of cost performance. Thus, such selective deposition is advised if no simulation tools are available for further cost-performance optimization.

## 5. Conclusions

This paper has presented a selective ink deposition method for performance-cost optimization of inkjet-printed UHF RFID tag antennas. The performance-cost optimization in this study has been made by identifying the areas on the tag antenna which exhibit high surface current density levels. A high-resolution printing mask is then created based on these surface currents. The printing mask selectively adds conductive ink only to these areas, possibly allowing for significant savings in the ink consumption and time required to print a high-performance tag antenna.

The results shown in this paper demonstrate the great potential of selective deposition masks acquired through simulations to reduce ink consumption while maintaining adequate performance levels. Moreover, these results show that it should be possible to match the read range distances of a case in which the tag antenna is printed using the full antenna pattern by using the selective deposition technique.

In terms of savings in ink consumption, the selective deposition masks showed decreases between 22% and 50% in the required ink volume against the full antenna pattern increase in case of the dipole-type tag antenna. These savings are possible between attainable read ranges of three to seven meters. Even greater ink savings and attainable read ranges could be achieved by discovering the optimal surface current level used as the selective deposition mask.

Future work involving selective deposition is how to provide further improvements in the performance-to-cost ratio. One of the possible approaches is to use different selective deposition masks in the fabrication of a single tag antenna.

## Acknowledgments

This research work was funded by the Finnish Funding Agency for Technology and Innovation (TEKES), the Academy of Finland, the Centennial Foundation of Finnish Technology Industries, the Finnish Foundation for Technology Promotion (TES), and KAUTE foundation. The authors would like to thank Jukka Lindfors and Marko Silvennoinen from Tampere University of Technology, Optoelectronics

Research Center for their help with the thickness measurements of the ink layer.

## References

- [1] H. C. Jung, S. H. Cho, J. W. Joung, and Y. S. Oh, "Studies on inkjet-printed conducting lines for electronic devices," *Journal of Electronic Materials*, vol. 36, no. 9, pp. 1211–1218, 2007.
- [2] S. Molesca, D. R. Redinger, D. C. Huang, and V. Subramanian, "High quality inkjet-printed multilevel interconnects and inductive componentson plastic for ultra-low-cost RFID applications," *Materials Research Society Symposium Proceedings*, vol. 769, pp. 831–836, 2003.
- [3] Z. Konstas, A. Rida, R. Vyas, K. Katsibas, K. N. Uzunoglu, and M. M. Tentzeris, "A novel "Green" inkjet-printed Z-shaped monopole antenna for RFID applications," in *Proceedings of the 3rd European Conference on Antennas and Propagation (EuCAP '09)*, pp. 2340–2343, March 2009.
- [4] J. Mujal, E. Ramon, E. Diaz et al., "Inkjet printed antennas for NFC systems," in *Proceedings of the 17th IEEE International Conference on Electronics, Circuits, and Systems (ICECS '10)*, pp. 1220–1223, December 2010.
- [5] Y. Amin, S. Prokkola, B. Shao, J. Hallstedt, H. Tenhunen, and Z. Li-Rong, "Inkjet printed paper based quadrate bowtie antennas for UHF RFID tags," in *Proceedings of the 11th International Conference on Advanced Communication Technology (ICACT '09)*, vol. 1, pp. 109–112, February 2009.
- [6] Z. Linlin, S. Rodriguez, L. Zhang, B. Shao, and L. R. Zheng, "Design and implementation of a fully reconfigurable chipless RFID tag using inkjet printing technology," in *Proceedings of the IEEE International Symposium on Circuits and Systems (ISCAS '08)*, pp. 1524–1527, May 2008.
- [7] P. V. Nikitin, S. Lam, and K. V. S. Rao, "Low cost silver ink RFID tag antennas," in *Proceedings of the IEEE Antennas and Propagation Society International Symposium and USNC/URSI Meeting*, vol. 2, pp. 353–356, July 2005.
- [8] J. Virtanen, L. Ukkonen, T. Björninen, A. Z. Elsherbeni, and L. Sydänheimo, "Inkjet-printed humidity sensor for passive UHF RFID systems," *IEEE Transactions on Instrumentation and Measurement*, vol. 60, no. 8, pp. 2768–2777, 2011.
- [9] V. Lakafosis, A. Rida, R. Vyas, Y. Li, S. Nikolaou, and M. M. Tentzeris, "Progress towards the first wireless sensor networks consisting of inkjet-printed, paper-based RFID-enabled sensor tags," *Proceedings of the IEEE*, vol. 98, no. 9, pp. 1601–1609, 2010.
- [10] M. M. Tentzeris, "Novel paper-based inkjet-printed antennas and wireless sensor modules," in *Proceedings of the IEEE International Conference on Microwaves, Communications, Antennas and Electronic Systems (COMCAS '08)*, pp. 1–8, May 2008.
- [11] J. Virtanen, T. Björninen, L. Ukkonen et al., "The effect of conductor thickness in passive inkjet printed RFID tags," in *Proceedings of the IEEE Antennas and Propagation Society International Symposium (APSURSI '10)*, pp. 1–4, July 2010.
- [12] J. Siden, T. Olsson, A. Koptioug, and H. E. Nilsson, "Reduced amount of conductive ink with gridded printed antennas," in *Proceedings of the 5th International Conference on Polymers and Adhesives in Microelectronics and Photonics, Polytronic*, pp. 86–89, October 2005.
- [13] J. Siden, M. K. Fein, A. Koptuyug, and H. E. Nilsson, "Printed antennas with variable conductive ink layer thickness," *IET Microwaves, Antennas & Propagation*, vol. 1, no. 2, pp. 401–407, 2007.
- [14] D. M. Pozar, *Microwave Engineering*, John Wiley & Sons, New York, NY, USA, 3rd edition, 2002.
- [15] Harima, "NPS-JL Silver Nanoparticle Ink, NanoPaste series, Metal Paste for Thin Film Formation," Datasheet, <http://www.harima.co.jp/en/products/pdf/16-17e.pdf>.
- [16] V. Pynttari, R. Mäkinen, J. Lilja, V. Pekkanen, P. Mansikkamäki, and M. Kivikoski, "Significance of conductivity and thickness of thin inkjet printed microstrip lines," in *Proceedings of the 12th IEEE Workshop on Signal Propagation on Interconnects (SPI '08)*, pp. 1–4, May 2008.
- [17] M. Mantysalo, P. Mansikkamäki, J. Miettinen et al., "Evaluation of inkjet technology for electronic packaging and system integration," in *Proceedings of the 57th Electronic Components and Technology Conference (ECTC '07)*, pp. 89–94, May 2007.
- [18] "Alien Higgs-3 RFID IC, Product Overview," <http://www.alientechnology.com/docs/products/Alien-Technology-Higgs-3-ALC-360.pdf>.
- [19] DuPont and H. N. Kapton, Datasheet, [http://www2.dupont.com/Kapton/en\\_US/assets/downloads/pdf/HN\\_datasheet.pdf](http://www2.dupont.com/Kapton/en_US/assets/downloads/pdf/HN_datasheet.pdf).
- [20] G. Marrocco, "The art of UHF RFID antenna design: impedance-matching and size-reduction techniques," *IEEE Antennas and Propagation Magazine*, vol. 50, no. 1, pp. 66–79, 2008.
- [21] K. Kurokawa, "Power waves and the scattering matrix," *IEEE Transactions on Microwave Theory and Techniques*, vol. 13, no. 3, pp. 194–202, 1965.
- [22] K. V. S. Rao, P. V. Nikitin, and S. F. Lam, "Impedance matching concepts in RFID transponder design," in *Proceedings of the 4th IEEE Workshop on Automatic Identification Advanced Technologies*, pp. 39–42, October 2005.
- [23] T. Björninen, M. Lauri, L. Ukkonen, R. Ritala, A. Z. Elsherbeni, and L. Sydänheimo, "Wireless measurement of RFID IC impedance," *IEEE Transactions on Instrumentation and Measurement*, vol. 60, no. 9, pp. 3194–3206, 2011.
- [24] "Ansys High Frequency Structure Simulator (HFSS) 13," <http://www.ansys.com/>.
- [25] "Fujifilm, Dimatix DMP-2800 Materials Printer, Overview," [http://www.fujifilmusa.com/products/industrial\\_inkjet\\_print-heads/deposition-products/dmp-2800/index.html](http://www.fujifilmusa.com/products/industrial_inkjet_print-heads/deposition-products/dmp-2800/index.html).
- [26] A. K. Sowpati, V. K. Palukuru, V. Pynttari, R. Mäkinen, M. V. Kartikeyan, and H. Jantunen, "Performance of printable antennas with different conductor thickness," *Progress in Electromagnetics Research Letters*, vol. 13, pp. 59–65, 2010.
- [27] M. Mantysalo and P. Mansikkamäki, "An inkjet-deposited antenna for 2.4 GHz applications," *AEU International Journal of Electronics and Communications*, vol. 63, pp. 31–35, 2007.
- [28] Voyantic Ltd., Tagformance Lite, Measurement Unit Overview, <http://www.voyantic.com/index.php?trg=browse&id=130>.
- [29] GS1, "Regulatory Status for Using RFID in the UHF Spectrum," [http://www.gs1.org/docs/epcglobal/UHF\\_Regulations.pdf](http://www.gs1.org/docs/epcglobal/UHF_Regulations.pdf).